Applying Biomimetic Modeling and Clinical Transcriptomics Data to Investigate Fibrotic Disease

by

Daniel L. Matera

A dissertation submitted in partial fulfillment
of the requirements for the degree of
Doctor of Philosophy
(Chemical Engineering)
in the University of Michigan
2022

Doctoral Committee:

Assistant Professor Brendon M. Baker, Chair
Assistant Professor Kelly B. Arnold
Professor Bethany B. Moore
Professor Lonnie D. Shea

Daniel L. Matera

dlmatera@umich.edu

ORCID iD: 0000-0003-4172-7903

Dedication

To all the friends and family who have supported me during my graduate studies.

Acknowledgements

Brendon, Willy & Chris, Sam & Harrison, other Baker lab members, undergrads, and collaborators.

Table of Contents

List of Figures

Abstract

Fibrosis is a hallmark of numerous diseases, including various cancers, post-infarction cardiac scarring, pulmonary fibrosis, and arteriosclerosis. With minimal available treatment options, fibrosis is implicated in 45% of all deaths in the developed world. Fibrotic diseases are characterized by myofibroblast (MF) differentiation, cellular proliferation and excessive extracellular matrix (ECM) synthesis, subsequently leading to a reorganization of tissue architecture and organ stiffening. Furthermore, while it has been well established that pro-fibrotic cytokines and ECM transformation correlate with MF differentiation and fibrotic progression, how 3D fibrotic ECM specifically affects stromal cell phenotype has been less explored. Despite their lack of canonical MF markers, alternative fibroblastic and endothelial cell subtypes may also be affected by fibrotic ECM and contribute to fibrosis. Thus, the overall focus of this dissertation is to 1) study how a 3D fibrous ECM affects fibroblast phenotype and 2) characterize the diversity of stromal phenotypes present in lung fibrosis.

Toward the above, this thesis firstly focuses on the design of a novel 3D fibrous biomaterial model of interstitial ECM and explores how physical attributes of 3D ECM (stiffness, fiber density) regulate the phenotype of primary lung fibroblasts. Using standard hydrogel chemistries and electrospinning methods, a model was established to approximate the fibrillar structure and mechanics of lung interstitial tissue. Our results revealed that crosslinking and stiffness did not directly promote MF differentiation in 3D environments, whereas matrix

fiber density was a strong driver of 3D MF differentiation. Furthermore, this differentiation mechanism was dependent upon matrix degradation via MMP activity, Rac1-mediated contact guidance along matrix fibers, and RhoA-mediated cell expansion and contractility. Alternative applications of this model, such as use for a drug screening platform were explored as well.

Subsequently, this thesis describes the phenotypic landscape of the human lung in a healthy and fibrotic state. Using clinical transcriptomics data, SC-RNA-SEQ analysis revealed various subtypes within the stromal compartment of the lung, including various fibroblasts, endothelial cells, pericytes, smooth muscle cells, and mesothelial cells. As the primary matrix producing cells, endothelial and fibroblast subtypes were explored in detail, with characterization of key biological pathways and regulators of these distinct cell types. To explore the relevance of the aforementioned fibrous hydrogel model to the native pulmonary microenvironment, transcriptomic analysis was conducted to cross reference with the clinical dataset. Alternative applications of these analyses included the identification of potentially novel regulators and pharmacologic targets which are actively being explored in murine models of fibrosis.

Overall, the work presented in this dissertation utilizes tissue engineering and bioinformatics approaches to investigate the fibrotic microenvironment. The data presented here suggests a tight regulation of stromal cell phenotype by 3D matrix fiber density and resultant cell mechanosensing. Furthermore, approaches used in this thesis present a path for the design and application of biomimetic disease models, and, via the combination of transcriptomics data, provide a guidepost for rational model benchmarking and biological discovery.

Chapter 1: Introduction

Toward the overall goal of better understanding the cell-scale microenvironment during fibrosis, this thesis utilizes a combination of tissue-engineering and bioinformatics approaches to investigate fibrotic pathology. More specifically, the following chapters employ synthetic and tunable biomaterial models to dissect the role of 3D physical cues during fibrogenesis, apply confocal microscopy to extract spatiotemporal information at the cell-scale, and utilize RNA-sequencing techniques to characterize cell phenotype at the whole-transcriptome level.

Chapter 2 serves as a broad introduction to the tissue-scale pathology of fibrosis and its connection to extracellular matrix (ECM). This chapter also serves to introduce fibrosis at the cellular scale, detailing the various types of cells and biological mechanisms that cells use to interact with their microenvironment. Lastly, Chapter 2 explores standard methods used for fibrosis research and their relative limitations, namely murine and *in vitro* models and the recent application of RNA-sequencing.

Chapter 3 focuses on the development of a new synthetic tissue model of fibrosis and resultant implications for the field of *in vitro* tissue modeling. This work established one of the first 3D synthetic and fibrous models of the ECM and documents the critical role of 3D architecture in regulating cell phenotype. Via orthogonal modulation of 3D matrix parameters, it was revealed that 3D cellular spread area was highly dependent upon matrix fiber density whereas stiffness controlled the temporal dynamics of cell outgrowth. Furthermore, it was shown

that fibroblast activation, as measured by proliferation and YAP activity, was also dependent upon 3D fiber density. Broadly, this chapter establishes and characterizes the first generation of the fibrous hydrogel composite platform used extensively in subsequent chapters.

The focal point of Chapter 4 involves the adaptation of the fibrous hydrogel composite model for use in pulmonary fibrosis research. Confocal and atomic force microscopy (AFM) of murine fibrotic tissue was used to establish design parameters for this model. After tuning model parameters, this chapter explores the role of fiber density and stiffness during the 3D MF differentiation process. In contrast to previous findings, this work proposes a new mechanism for 3D MF differentiation which is less dependent on the bulk stiffness of the cellular microenvironment. More specifically, matrix degradation and fiber density were found to have profound effects on MF differentiation in 3D. This chapter also provides enhanced biological characterization of cells within the fibrous hydrogel platform, namely via gene expression, cytokine, and immunofluorescence data. Finally, this model explores the utility of 3D synthetic models for pharmacologic screening applications.

Building on the previous work, Chapter 5 provides a deeper investigation into the cell-scale mechanism at play during 3D fibrogenesis *in vitro*. This work also examined the temporal stages of MF differentiation in 3D: firstly, cell spreading along matrix fibers initiates outgrowth, followed by cell proliferation, migration, network formation, and finally MF differentiation and ECM contraction. Using pharmacologic inhibitors of key mechanosensitive proteins, the contribution of various Rho GTPases was explored during the differentiation process. Notably, interplay between RhoA and Rac1 were found to be critical during 3D mechanosensing whereas RhoA was the primary driver in 2D. Overall, this work serves to expand on the results from Chapter 4, providing additional detail from a mechanobiological perspective.

Chapter 6 serves as a departure from prior work and focuses on the transcriptional landscape of cells derived from patients diagnosed with pulmonary fibrosis. In an attempt to address some of the limitations of *in vitro* models, Chapter 6 is primarily investigational and serves to characterize the tissue spaces that are of interest to the fibrosis-modeling community. Using standard bioinformatics analyses on single-cell RNA sequencing (scRNA-seq), this work identifies numerous stromal cell populations present in the lung during fibrosis, namely 5 subtypes of fibroblast and 6 subtypes of endothelial cells. Notably, two cell types marked by the POSTN gene (one fibroblastic and one endothelial) were found to expand only in patients diagnosed with fibrosis. Subsequently, to serve as a link to previous Chapters 2-5, the transcriptional landscape of the 3D fibrous hydrogel model is explored and its relevance to patient lung is discussed. A scRNA-seq analysis on ~50,000 fibroblasts from various hydrogel and media conditions revealed that different populations exist within *in vitro* models, but with only minor similarity between 2D and 3D contexts. Furthermore, it was revealed that certain *in vitro* populations bear more resemblance to their clinical counterparts than others, most notably one 3D population marked by CTHRC1. Finally, this work explores the potential use of bioinformatics data to identify regulators of disease and their potential drug targets. Overall, this work further characterizes the fibrous hydrogel model and raises critical implications for the future of the disease-modeling field. In addition, this chapter highlights the utility of using publicly available transcriptomics data and serves as a guide for future experiments within the bioengineering field.

Chapter 7 serves as a brief reflection on the field of fibrosis modeling. This chapter outlines critical research goals for the field over the next decade, discusses the advantages of emerging bioengineering technologies, and highlights the various limitations of current *in vitro*

research. When paired with Chapter 6, this work serves as an overview of the cutting edges of fibrosis research.

Finally, Chapter 8 summarizes the primary findings from this thesis work and emphasizes the outstanding questions and challenges that must be addressed going forward. While bioengineering techniques hold great promise for the study of human health and disease, the future of fibrosis research will have to be interdisciplinary; the integration of tissue-engineering technologies, bioinformatics approaches, and clinical samples will be critical as the field progresses.

Chapter 2: Background

2.1 An Introduction to Fibrotic Disease

Accounting for nearly half of all deaths in the developed world (Wynn, 2008), fibrosis is a central component of numerous diseases, including in many cancers, atherosclerosis, arthritis, and in pulmonary fibrosis (PF), the primary focus of this dissertation. In the clinic, fibrosis manifests as a severe scarring process; organ function declines as (functional) parenchymal organ structures are remodeled and converted into non-functional scar tissue. Furthermore, most fibrotic diseases are not sufficiently treatable; PF is particularly severe with a post-diagnosis survival of only 3–5 years (Bagnato & Harari, 2015). Poor prognosis is likely due to numerous factors: 1) a lack of sufficient early detection technologies restrict clinical intervention to patients with late-stage disease, 2) late-stage fibrosis often presents in older (>65 years of age) patients with a limited tissue-regeneration potential, 3) patient populations are often heterogeneous and contain various comorbidities, and 4) pharmacologic intervention is hindered by a limited understanding of fibrosis pathobiology, and, for known drug targets, by limited mechanisms for organ- and cell- specific drug delivery (Shastri et al., 2020). As a result, enhanced understanding of fibrosis pathology is critical for the identification of new diagnostic and therapeutic avenues.

Unfortunately, the biological mechanisms that drive (clinically relevant) late-stage fibrotic disease are still relatively obscure and difficult to study. This is, in part, due to the difficulty in recreating and studying an illness that often takes years to develop in humans (Wells

& Maher, 2017). Thus, basic research has largely focused on understanding the early stages of fibrosis as it develops; a granular understanding of fibrotic development should, at least partially, provide a foundation for understanding late-stage illness. Indeed, decades of research have established a general disease paradigm **(Figure 2.1)** whereby chronic tissue damage leads to immune cell accumulation (e.g. macrophages), the release of specific inflammatory factors (e.g. TGF-β1), and the activation of scar-forming myofibroblasts (MFs) which directly remodel the organ, spurring further tissue damage and promoting further immune cell recruitment; this feed-forward loop is proposed to drive a progressive scarring process until the stage of organ failure (D. Jiang, Dey, & Liu, 2020).

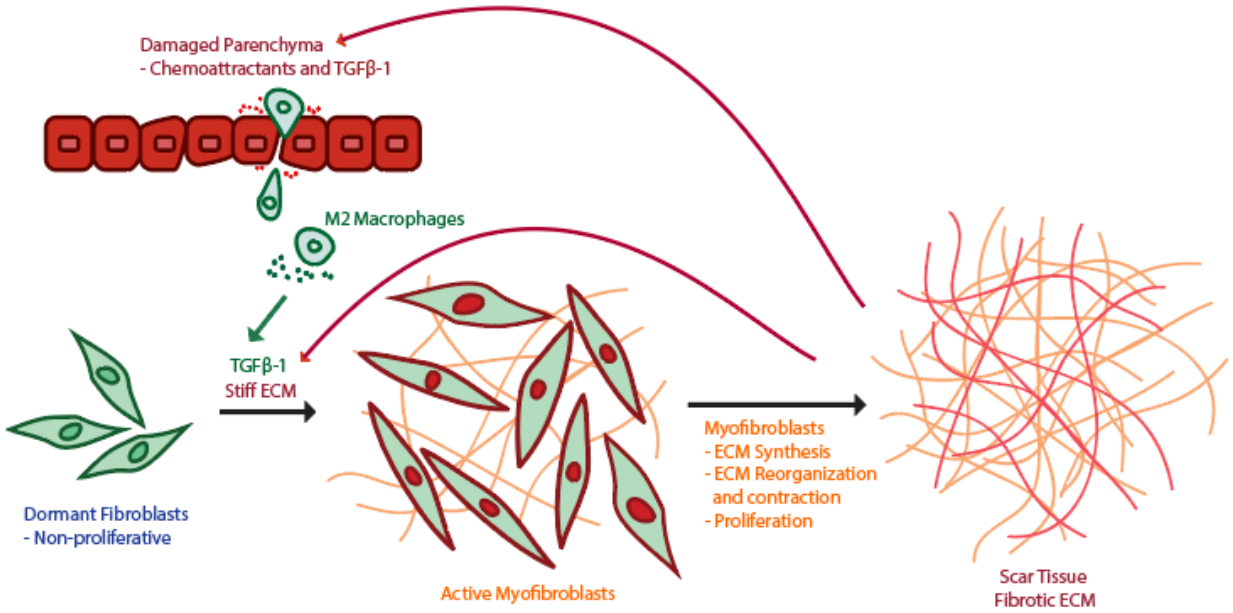

Figure 1: A common paradigm for fibrosis progression. Schematic depicting one of the major proposed feedback loops present in the development of fibrosis.

Importantly, the above paradigm has grown increasingly complex over time as numerous other cell types and feedback loops have been identified (Boris Hinz et al., 2012). For example, scar tissue itself may drive the accumulation of MFs through the mechanical activation of mesenchymal stem cells and healthy dormant fibroblasts (a mechanism discussed in detail in the

following section). MFs within fibrotic foci (regions of active scar formation) may also secrete their own TGF-β1, potentially allowing them to drive disease progression in the absence of macrophages (Tschumperlin & Lagares, 2020). Beyond just MFs, fibrotic regions of the lung are often heterogeneous **(Figure 2.2)** and have been shown to contain deformed vasculature, raising the question as to whether aberrant endothelial cells may also play a role in disease progression. In fact, patients with PF commonly present with pulmonary hypertension, a comorbidity that primarily affects the vasculature (Colombat et al., 2007). Indeed, the adoption of scRNA-seq technologies has further identified >30 different types of cells in fibrotic lung, many of which are unique subtypes of fibroblasts and endothelial cells; each may have their own function in a health- and disease-specific context (Sit, Chang, Conley, Mori, & Seita, 2019).

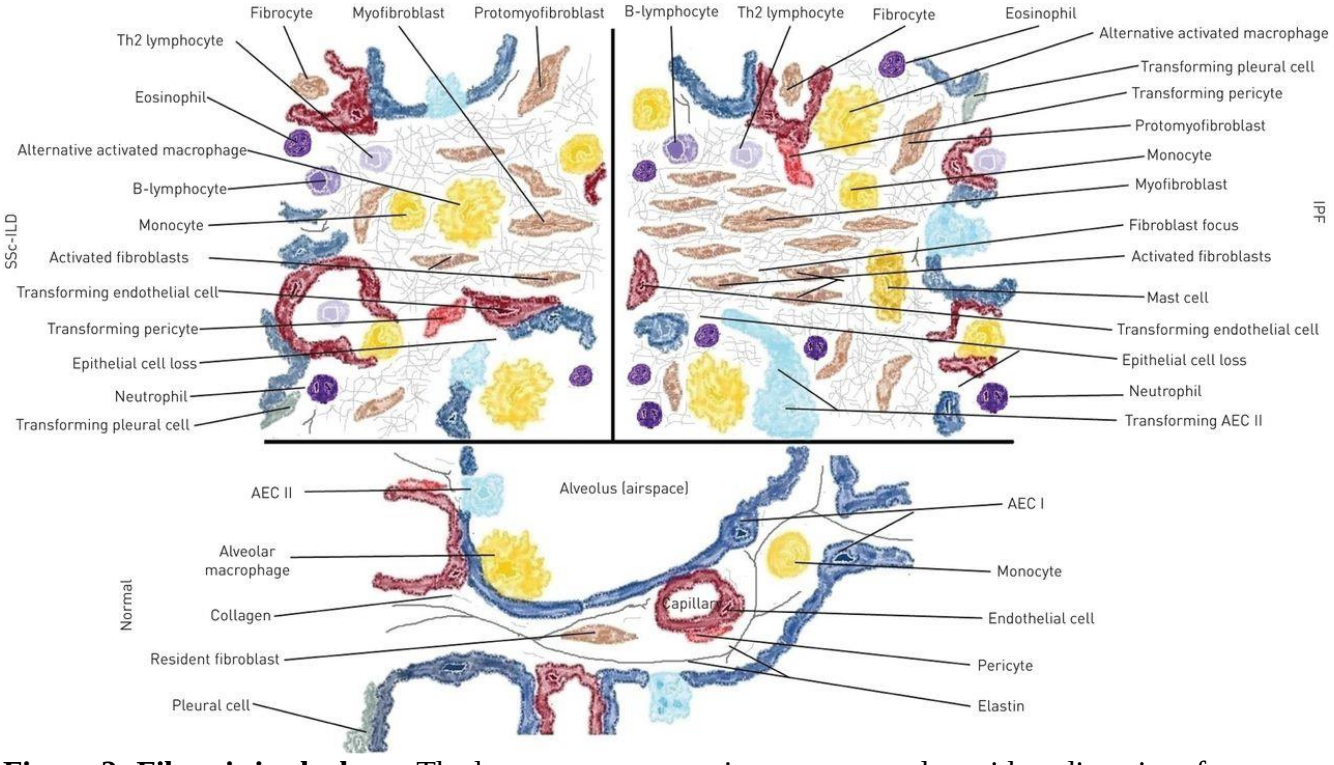

Figure 2: Fibrosis in the lung. The lung possesses a unique structure alongside a diversity of celltypes (bottom), both of which are altered in fibrotic disease (top). Image reproduced from (Bagnato & Harari 2015)https://err.ersjournals.com/content/24/135/102

While ongoing research aims to understand the relative contribution of various cell types to fibrosis progression, the role of the physical microenvironment is also under active investigation. In contrast to the cellular microenvironment, changes in the physical microenvironment (i.e. ECM) are relatively homogenous in terms of composition. In fact, the primary extracellular components (i.e. type 1 collagen) of fibrotic tissue are conserved within the lung and across all organ fibroses (Ushiki, n.d.). In fact, increased collagen deposition is a strong prognostic indicator of pulmonary fibrosis, heart disease, breast and pancreatic cancers (Humphrey, Dufresne, & Schwartz, 2014; Pearce et al., 2017; Provenzano et al., 2008; Rockey, Bell, & Hill, 2015; Sato, Fujiwara, & Takatsu, 2012). Furthermore, collagen and other ECM components serve as fundamental regulators of healthy tissue homeostasis; dysregulated matrix deposition may hinder tissue repair mechanisms. Beyond simply a marker of scar tissue, such observations have raised the possibility that ECM accumulation could directly underlie aberrant signaling in fibrosis. Moreover, a precise understanding of the role of ECM in fibrosis may inform the behavior of various cell types and guide the design of next-generation therapeutics. The following sections will discuss the ECM in detail, as well as explore the MF, the primary producer of ECM *in vivo*.

2.2 The Extracellular Matrix and the Myofibroblast

As tissue structure and biological function are tightly intertwined, the ECM serves as a critical regulator of numerous biological events including developmental morphogenesis, vascularization, and wound repair (S. H. Kim, Turnbull, & Guimond, 2011; Shoulders & Raines, 2009; Wozniak & Chen, 2009). ECM can be subdivided into regions of basement membrane and interstitial matrix. Basement membrane proteins such as type IV collagen and laminin serve as

key structural elements for epithelial tissue regions such as the pulmonary alveoli (Mouw, Ou, & Weaver, 2014). Interstitial ECM, a complex 3D composite of gel-like hydrophilic proteoglycans **(Figure 2.3)** and interpenetrating micron-scale fibrils, serves to provide biomechanical support to the basement membrane and acts as a reservoir for various cell types and growth factors. In the context of pulmonary fibrosis, the expansion of interstitial ECM into the alveolar basement

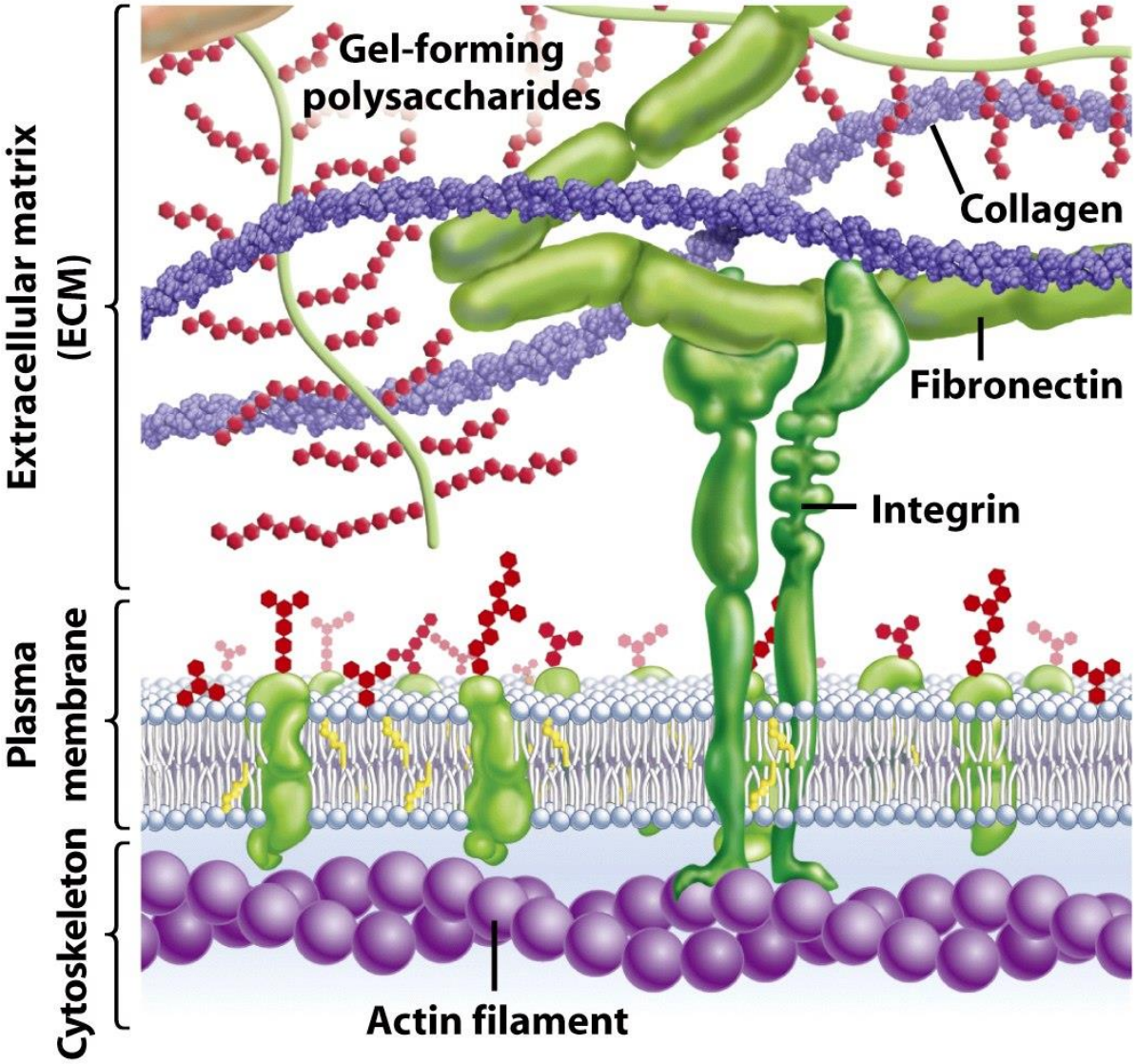

Figure 3: Structure of the interstitial extracellular matrix. Diagram of the interstitial extracellular matrix, including the major cellular components which serve as a link between the cytoskeleton and ECM. Image reproduced from (Freeman 2005).

membrane is thought to drive diseases progression and scar formation. Although numerous proteins and proteoglycans exist within interstitial ECM, this thesis will manly focus on fibrous type-1 collagen as it is the most abundant protein in mammals and is the primary protein deposited during fibrosis.

In addition to providing biomechanical support at the tissue-level, interstitial ECM serves as a biomechanical signal at the cellular scale. A diverse array of transmembrane integrin proteins directly recognize and bind to the ECM and create a mechanical linkage between tissue-resident cells and the extracellular tissue space (Huveneers & Danen, 2009). Furthermore, integrin clustering can lead to the creation of focal adhesion complexes which serve to provide key intracellular signals for cell survival, migration, proliferation, and differentiation in a process called mechanotransduction. In additional to serving as a source of critical intracellular signals, focal adhesions are dynamic mechanosensitive complexes that allow cells to sense and respond to changes in their physical microenvironment; ECM stiffening, degradation, deposition, and remodeling processes are all highly dependent on integrin and focal adhesion signaling (van Helvert, Storm, & Friedl, 2018). In the context of fibrosis, recently deposited type-1 collagen serves as a major target of cellular integrins and thus impacts the behavior of nearly every cell type within fibrotic tissue.

Differentiated from dormant interstitial fibroblasts via a combination of biochemical and mechanical signals, MFs are thought to be the primary cell type responsible for type-1 collagen synthesis, stiffening, and remodeling during fibrosis (Chong, Sato, Kolb, & Gauldie, 2019). Seminal findings *in vivo* have noted increased MF proliferation and differentiation in splinted wounds under increased force, and have been supported by *in vitro* work showing similar responses in collagen gels either unconstrained or under tension (Arora, Narani, & McCulloch,

1999; Giulio Gabbiani, 2003). Importantly, it has also been demonstrated that MF induction is focal adhesion dependent and does not occur on culture surfaces below a threshold stiffness, even in presence of potent pro-fibrotic soluble cues such as transforming growth factor β1 (TGF-β1) (Balestrini, Chaudhry, Sarrazy, Koehler, & Hinz, 2012). Taken together, these studies implicate tissue structure and mechanics as central drivers of MF differentiation and thus disease progression, yet also contribute to ambiguity - MF induction seemingly requires mechanical tension, yet MFs themselves are thought to be responsible for ECM secretion and contraction. In the context of PF, fibrotic regions exhibit increasingly dense and stiff collagen microstructure and contain a large MF population that is absent in the healthy lung; understanding the factors that contribute to MF differentiation and their maintenance is a major aim of this thesis.

2.3 Modeling the Fibrotic Microenvironment

2.3.1 Murine Models of Fibrosis

Numerous animal models have been developed for the study of pulmonary fibrosis, most of which focus on the emergence of disease in mice. The most common model involves the intratracheal injection of bleomycin, a chemotherapeutic agent known to cause lung fibrosis in humans (Peng et al., 2013). After administration, bleomycin leads to the production of free radicals and causes significant DNA damage in the pulmonary epithelium. Following epithelial cell death (day 1-4) and the release of inflammatory factors (day 1-7), a fibroproliferative phase (day 7-21) emerges that is reminiscent of PF in humans **(Figure 2.4)**.

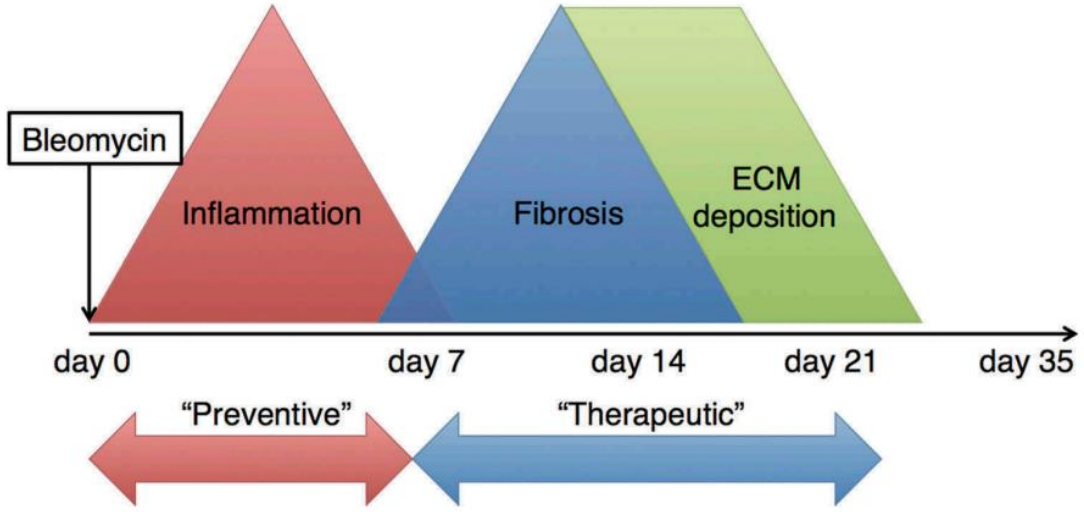

Figure 4: Timecourse for the bleomycin-induced pulmonary fibrosis model. Notably, much research has focused on studying fibrosis development and treatment prior to the later-stage ECM deposition phase. Image reproduced from (Yanagihara and Kolb, 2019).

While not a perfect recapitulation of human disease, the fibroproliferative phase of bleomycin injury shares many common features with PF, including the damaging of the alveolar basement membrane, the accumulation of MFs and type-1 collagen, and a resultant decline in lung function. Indeed, the bleomycin model has illuminated the importance of numerous signaling mediators (TGF-b1, IL-4, PDGF, etc.), celltypes (MFs, macrophages, AT2 cells, among others), and matrix proteins (collagen, elastin, heparan sulfate, fibronectin) that emerge during fibrosis onset (Kolb et al., 2020). However, the bleomycin model has critical disadvantages including 1) an inflammatory phase more reminiscent of acute lung injury than PF, 2) a reversion phase not present in humans, and 3) the inherent dissimilarity between murine and human lung. Indeed, the limitations of the bleomycin model are highlighted by the high proportion of drugs that fail in clinical trials, despite their curative function in mice (H. Bart van der Worp, D. W. Howells, E.S. Sena, M.J. Porritt, S. Rewell, V. O'Collins, 2016). Outside of translational research, a lack of sufficient intravital imaging technologies and the lethality of

ECM-specific genetic knockouts limit the use of the bleomycin model for studying basic MF-ECM biology at the cellular scale. Additionally, dynamic monitoring of multiple cell types and their interactions during disease progression remains challenging to do *in vivo.* Despite these challenges, it is likely that the bleomycin model will remain a vital tool for PF research. Further development of human-specific models and *in vitro* platforms will be needed as a supplement to the bleomycin model; together these technologies may be able to bridge the translational gap.

2.3.2 *In Vitro* Models of Fibrosis

While providing foundational knowledge, the aforementioned limitations of animal models have promoted the development of *in vitro* models of fibrosis **(Figure 2.5)**. The first generation of synthetic models were quite simplistic and typically involved 2D culture surfaces; traditional models primarily use flat, elastic surfaces of varying crosslinking to model either healthy (soft) or diseased (stiff) ECM in 2D (Engler, Sen, Sweeney, & Discher, 2006). These reductionist gel surfaces fail to recapitulate the 3D fibrous microstructure seen within lung interstitia, and lack any potential for structural reorganization/stiffening by cells, a key event during the transition from healthy to fibrotic tissue (Baker et al., 2015). Importantly, while these remodeling events lead to structural changes at the tissue scale, they also have signaling consequences at the cellular level; fibrous ECM reorganization prompts force transmission across large distances and facilitates intercellular communication and cytoskeletal rearrangement between cells (Guo, Ouyang, & Yu, 2013; Hall et al., 2016; Stracuzzi et al., n.d.). As these events are postulated to occur during pathology *in vivo* (Cox & Erler, 2011a), it would be advantageous to capture these processes when studying MF biology *in vitro*. Models developed in this thesis aim to recapitulate these dynamic matrix-dependent processes.

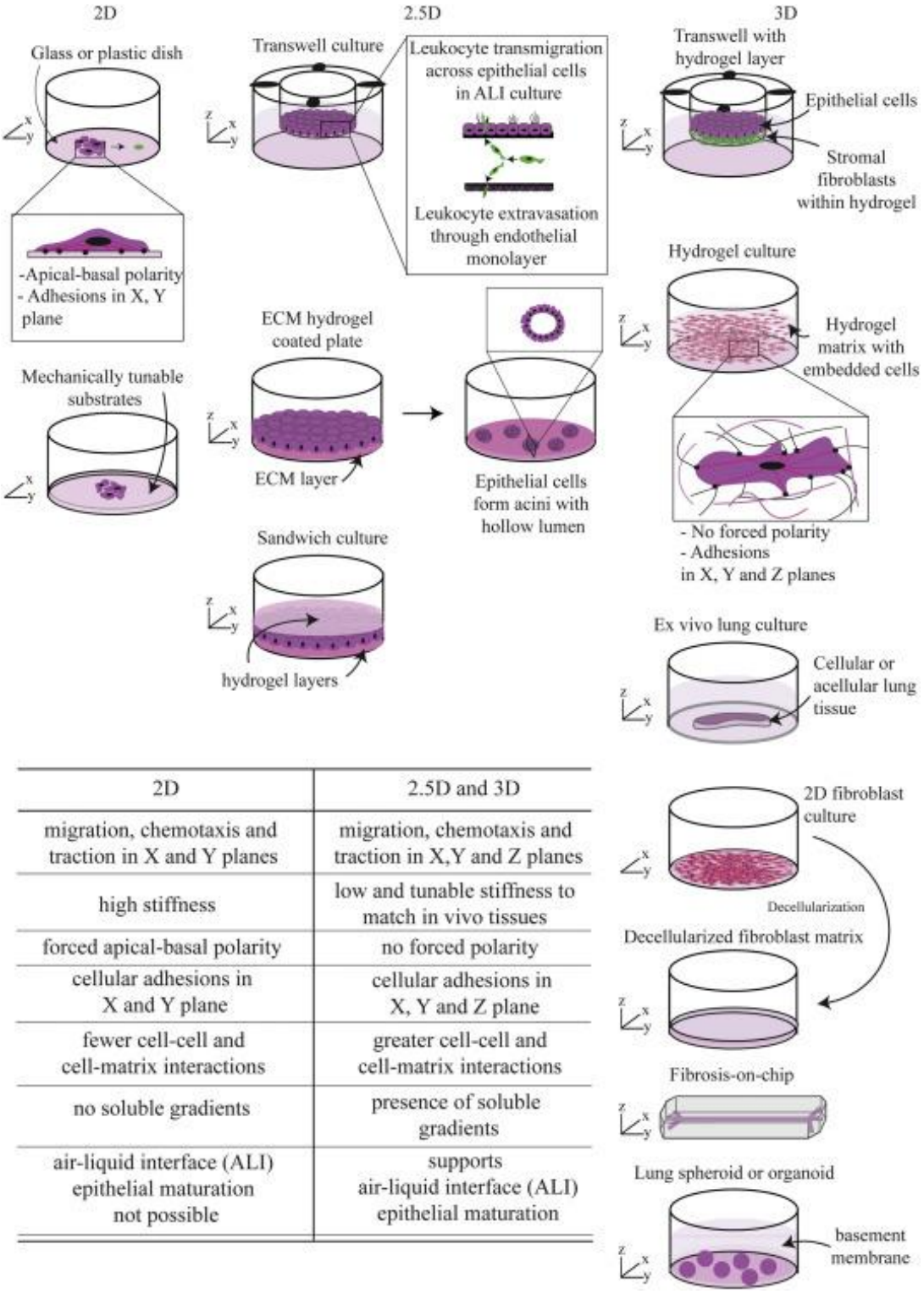

2D	2.5D and 3D
migration, chemotaxis and traction in X and Y planes	migration, chemotaxis and traction in X,Y and Z planes
high stiffness	low and tunable stiffness to match in vivo tissues
forced apical-basal polarity	no forced polarity
cellular adhesions in X and Y plane	cellular adhesions in X, Y and Z plane
fewer cell-cell and cell-matrix interactions	greater cell-cell and cell-matrix interactions
no soluble gradients	presence of soluble gradients
air-liquid interface (ALI) epithelial maturation not possible	supports air-liquid interface (ALI) epithelial maturation

Figure 5: Approaches for modeling fibrosis *in vitro*. Depiction of various 2D, 2.5D, and 3D models of fibrosis, including hydrogel surfaces and traditional glass culture (top left), transwell systems (top middle), and hydrogel-based approaches. 2.5D and 3D naturally derived culture materials are discussed, including the use of tissue explants and cell-derived matrix (middle right). Image reproduced from (Sundarakrishnan and Kaplan, 2017).

In contrast to established synthetic models, natural materials (decellularized tissue, reconstituted collagen and fibrin gels) typically possess architecture more reminiscent of *in vivo* tissue and allow for cell-mediated remodeling (Shinsato, Doyle, Li, & Yamada, 2020). Indeed, many established on-chip technologies primarily use natural materials and have yet to be adapted for use with synthetic hydrogel platforms. Nevertheless, natural materials have batch-specific variability, poor long-term stability, and lack orthogonal control over matrix properties; such disadvantages have limited the use of natural materials for the study of MF biology (Sundarakrishnan et al., 2019). As a result, next-generation fibrosis models will require the tunability and control of synthetic models as well as the biomimicry of natural materials; Chapter 3 will discuss prior models in detail as well as the development of a novel bioengineered model of fibrotic ECM.

2.3.3 In *Silico* Models of Fibrosis: Transcriptomics

In addition to animal and biomaterial models of fibrosis, recent advancements in next-generation sequencing technologies have enabled researchers to construct *in silica* models of the pulmonary microenvironment (Xu et al., 2016). More specifically, scRNA-seq allows for reconstruction of the cellular microenvironment at unprecedented resolution **(Figure 2.6)**. Established bioinformatics pipelines allow researchers to cluster cells based on similarity, identify emerging and canonical cell types, and conduct downstream analysis to elucidate potential cell phenotype. Importantly, scRNA-seq analyses assume that mRNA transcripts are an acceptable proxy for cellular phenotype; experimental validation is often required. Nevertheless, these technologies have aided in the identification of numerous cell types within the lung (Farber & Sims, 2019; Jin et al., 2021; Morse et al., 2019; Xiang et al., 2020) and have provided clinicians with the ability to characterize patient heterogeneity at an increasingly fidelity (Wu et

al., 2020). While yet to be fully realized, the pairing of *in silica* disease models with their *in vivo* and *in vitro* counterparts may allow researchers to compare clinical & benchtop samples at the whole-genome level, allowing for objective analysis of model accuracy. Single-cell transcriptomics are likely to play a large role in the study of fibrosis going forward and are discussed in further detail within Chapter 6.

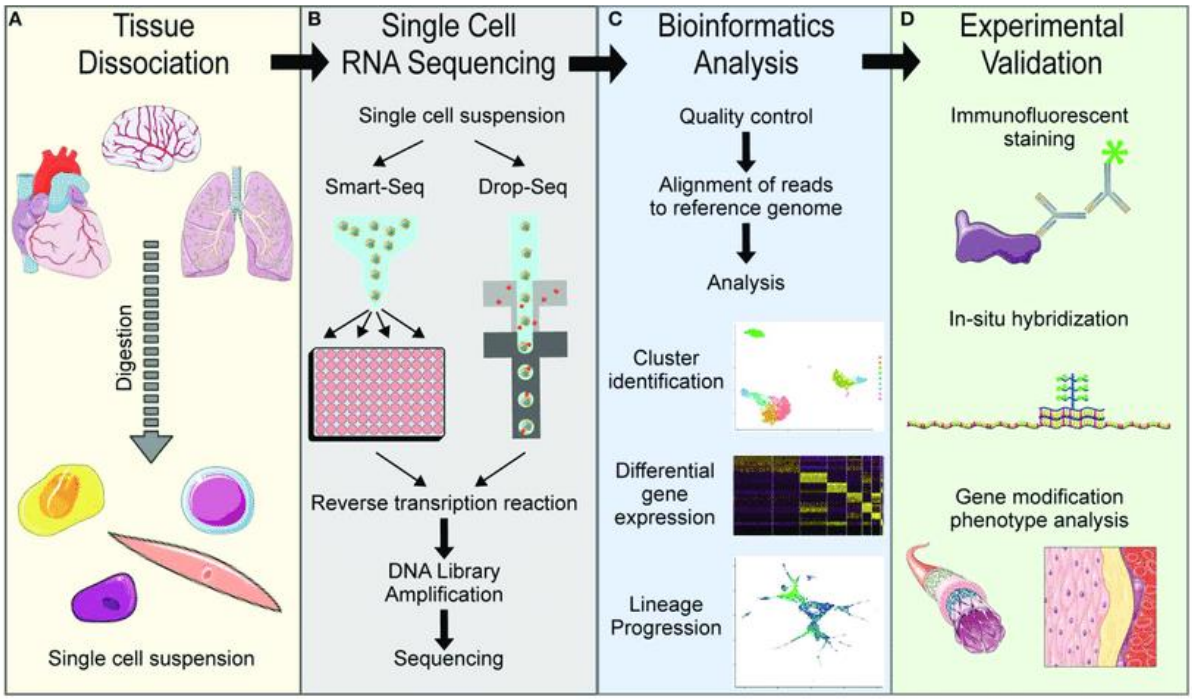

Figure 6: Overview of standard single-cell RNA sequencing pipelines. Established single-cell sequencing technologies typically involve tissue or material digestion (A) to extract single cells, followed by the barcoding, labeling, and sequencing of the RNA present within each individual cell (B). Downstream analysis typically involves standard PCA-based models which help evaluate different cell types and their gene expression (C). After bioinformatics analysis, experimental validation is often required. Figure adapted from (Chavkin and Hirschi, 2020)

Chapter 3: A Bioengineered Model of the Interstitial Extracellular Matrix

3.1 Authors

Daniel L. Matera, William Y. Wang, Makenzee R. Smit1, Ariella Shikanov, Brendon M. Baker

3.2 Abstract

Cellular phenotype is heavily influenced by the extracellular matrix (ECM), a complex and tissue-specific three-dimensional structure with distinct biophysical and biochemical properties. As naturally derived cell culture platforms are difficult to controllably modulate, engineered synthetic ECMs have facilitated our understanding of how specific matrix properties direct cell behavior. However, synthetic approaches typically lack fibrous topography, a hallmark of stromal and interstitial ECMs *in vivo*. To construct tunable biomimetic models with physiologic microstructure, we developed a versatile approach to generate modular fibrous architectures in 3D. Photocrosslinkable polymers were electrospun, photopatterned into desired lengths, and co-encapsulated alongside cells within natural biopolymer, semi-synthetic, and synthetic hydrogels. Cells encapsulated within fiber-reinforced hydrogel composites (FHCs) demonstrated accelerated spreading rates compared to in gels lacking such fibrous topography. Furthermore, increases in fiber density at constant bulk elastic modulus produced

morphologically distinct cell populations and modulated cellular mechanosensing in 3D, as evidenced by increased nuclear localization of the mechanosensitive transcription factor, Yes-associated protein (YAP). This work documents the impact of physical guidance cues in 3D and establishes a novel approach to generating more physiologic tissue- and disease-specific biomimetic models.

3.3 Introduction

A complex 3D composite of gel-like hydrophilic proteoglycans and interpenetrating micron-scale fibrils, the interstitial extracellular matrix (ECM) regulates numerous biological events in developmental morphogenesis, vascularization, and wound repair processes (S. H. Kim et al., 2011; Shoulders & Raines, 2009; Wozniak & Chen, 2009). Furthermore, while the ECM has emerged as a fundamental regulator of tissue homeostasis, dysregulated matrix signaling via excessive ECM synthesis and tissue stiffening is believed to drive multiple disease pathogeneses. For example, increased collagen deposition is a strong prognostic indicator of pulmonary fibrosis, heart disease, breast and pancreatic cancers (Humphrey et al., 2014; Pearce et al., 2017; Provenzano et al., 2008; Rockey et al., 2015; Sato et al., 2012). Unfortunately, lack of control over the ECM *in vivo* has hampered mechanistic understanding of how biophysical microenvironmental cues affect disease-related signaling. Thus, *in vitro* biomimetic hydrogel platforms have been crucial in parsing the effects of individual ECM properties (eg. elastic modulus, ligand density, degradability) on cellular phenotype (L. Li, Eyckmans, & Chen, 2017). Tremendous *in vitro* efforts have established a paradigm for cell-ECM mechanosensing, whereby substrate stiffness and ligand availability dictate the magnitude and arrangement of intracellular forces, in turn mediating cytoskeletal assembly, cell morphology, and downstream intracellular

signaling cascades (Discher, 2005; Engler et al., 2006; Plotnikov, Pasapera, Sabass, & Waterman, 2012; Yeung et al., 2005). Veritably, cellular morphology (spread area and shape) is implicated in a plethora of cell functions including proliferation, differentiation, and migration, all of which are relevant to disease (Humphrey et al., 2014; Pathak & Kumar, 2011).

Naturally derived ECM proteins such as type-I reconstituted collagen gels have emerged as the most common approach to modeling interstitial ECM. While the iterative enzyme-mediated assembly of such proteins leads to diverse and hierarchical structure *in vivo*, reconstituted gels of ECM proteins typically form via non-covalent interactions and protein precipitation (Hotary, Li, Allen, Stevens, & Weiss, 2006; Shoulders & Raines, 2009). As a result, naturally derived matrices typically have poor mechanical properties and short fibrils with nanometer-scale diameters, whereas stromal tissues *in vivo* contain assemblies of fibers with micrometer-scale diameters and lengths spanning multiple cell bodies (Wolf et al., 2009). Additionally, reconstituted collagen matrices lack a space-filling proteoglycan component and possess biophysical properties that are difficult to modulate independently (e.g. increasing the concentration of a collagen gel simultaneously increases stiffness, fiber and ligand density, and decreases pore size) (Ghajar et al., 2008; L. Li et al., 2017; Riching et al., 2015). Beyond increasing gel concentration, many techniques have been developed to further modulate collagen properties, but are plagued by similar challenges. For example, cold gelation techniques increase fiber diameter and length, but alter pore size and fiber stiffness, while chemical modifications such as hydrogel co-gelation or glycation can alter stiffness but may also impact pore size and gel architecture (Berger, Linsmeier, Kreeger, & Masters, 2017; Mason, Starchenko, Williams, Bonassar, & Reinhart-King, 2013). This intrinsic coupling of gel mechanical properties, matrix

topography, and ligand density has hindered the application of reconstituted ECM proteins for mechanistic study of the cellular microenvironment.

In contrast to naturally derived ECMs, synthetic hydrogels offer a controllable and modular design and have proven indispensable for studying the impact of bulk material properties (e.g. crosslinking density, stiffness, degradability) on cell function. Unfortunately, these nanoporous crosslinked polymer networks traditionally possess homogenous ligand distribution, mechanically behave as elastic continuums, and lack cell-scale topographical features (Russell & Carta, 2005; Sen, Engler, & Discher, 2009). As collagen is the most abundant protein in mammalian tissue, fibrous matrix architecture is ubiquitous *in vivo* and engenders unique biophysical properties: native ECMs possess intrinsic micron-scale topography, non-linear and anisotropic mechanics, and heterogeneity in ligand distribution at the length-scale of the cell (Handorf, Zhou, Halanski, & Li, 2015; S. H. Kim et al., 2011; Shoulders & Raines, 2009; H. Wang, Abhilash, Chen, Wells, & Shenoy, 2015). Discrete but interconnected fibers spatially define adhesion and degradation sites, consequently guiding cell spreading and migration (Cox & Erler, 2011a; Sapudom et al., 2015; van Helvert et al., 2018; Zhang et al., 2014). Recent studies have highlighted diverging cellular responses in fibrous compared to non-fibrous settings, exemplified by orders of magnitude discrepancies in effective therapeutic dosage when screening anti-proliferative and anti-migratory cancer drugs (Aref et al., 2013; Fallica, Maffei, Villa, Makin, & Zaman, 2012; Fong, Harrington, Farach-Carson, & Yu, 2016). Similarly, groups such as ours have documented opposing trends between fibrous and gel-like surfaces, whereby increased substrate stiffness promoted cell spreading on flat hydrogel surfaces but hindered cell spreading on fibrous substrates of the same material (Baker et al., 2015; Ramirez-San Juan, Oakes, & Gardel, 2017). Indeed, it remains to be shown how findings from

elastic hydrogels will translate to more mechanically complex *in vivo* settings (Knight & Przyborski, 2015; Tibbitt & Anseth, 2009).

Electrospinning has emerged as the most common technique used to create synthetic fibrous materials in the micron diameter range (Shapiro & Oyen, 2013). While this method allows for control of fiber composition and diameter, electrospun materials are typically relegated to thin (<1 mm) continuous mats with subcellular pore sizes, thus preventing significant 3D cell infiltration and isotropic cellular spreading (Baker et al., 2015; Shapiro & Oyen, 2013). Dual jet electrospraying/electrospinning or hydrogel infiltration approaches have previously been employed to create electrospun fiber-reinforced hydrogels (Coburn et al., 2011; Ekaputra, Prestwich, Cool, & Hutmacher, 2008). These techniques have proven useful for increasing hydrogel mechanical properties but have not yet been adapted to create biomimetic models of stromal ECM (Shapiro & Oyen, 2013). Additionally, the utilization of rigid and protein adsorbent polyester based electrospun fibers (eg. polycaprolactone, poly lactic acid, and polylactide-co-glycolide) yields matrices that adsorb cell-derived and serum proteins nonspecifically and therefore lack control over ligand presentation, and additionally possess structure defined by electrospinning conditions which typically results in sub-micron interfiber spacing. These attributes render such first generation composites non-ideal when modeling *in vivo* stromal architecture with orthogonal control over individual ECM features (such as fiber and ligand density).

Given the multi-component architecture of *in vivo* tissue and the widespread move toward more physiologic 3D culture platforms, incorporating both gel (proteoglycan-like) and fibrous (collagen-like) ECM components within a single synthetic and controllable 3D model would be a major advance. To this end, here we describe an innovative dual-component

fabrication approach for creating 3D fiber-reinforced hydrogel composites (designated FHCs), with independent control over the bulk material (naturally derived, semi-synthetic, or synthetic gel) and fiber constituents (adhesive ligand, diameter, length, density). Furthermore, as excessive ECM fiber deposition is associated with numerous pathologic conditions, we examined the effect of fiber density on cell morphology, proliferation, and ECM mechanosensing in these synthetic 3D fibrous microenvironments.

3.4 Results and Discussion

To create biocompatible and tunable fibers, we selected dextran, a protein-resistant hydrophilic polysaccharide with a diverse array of properties, including biocompatibility, non-immunogenicity, and ease of functionalization (Sun & Mao, 2012). Furthermore, linear, high molecular weight dextrans are amenable to electrospinning, and functionalization with pendant vinyl sulfone groups supports rapid photocrosslinking via UV-initiated radical polymerization. While electrospinning typically results in a single interconnected fibrous meshwork, this chemistry enables the fabrication of individual fiber segments with defined lengths via a photopatterning approach. Mats of water-soluble dextran vinyl sulfone (DexVS) fibers photomasked during UV-exposure resulted in crosslinked segments of individual fibers under transparent mask regions, while material beneath opaque regions are water-soluble and could be removed via hydration. This process allowed for the rapid fabrication of thick fibrous mats allowing for the fabrication of DexVS fibers at a throughout higher than that of the alternative fabrication processes, namely microfabrication, electrowriting, bioprinting, and fiber-pulling. Additionally, tuning of UV photocrosslinking and photomask spacing provide defined control over fiber geometries and mechanics.

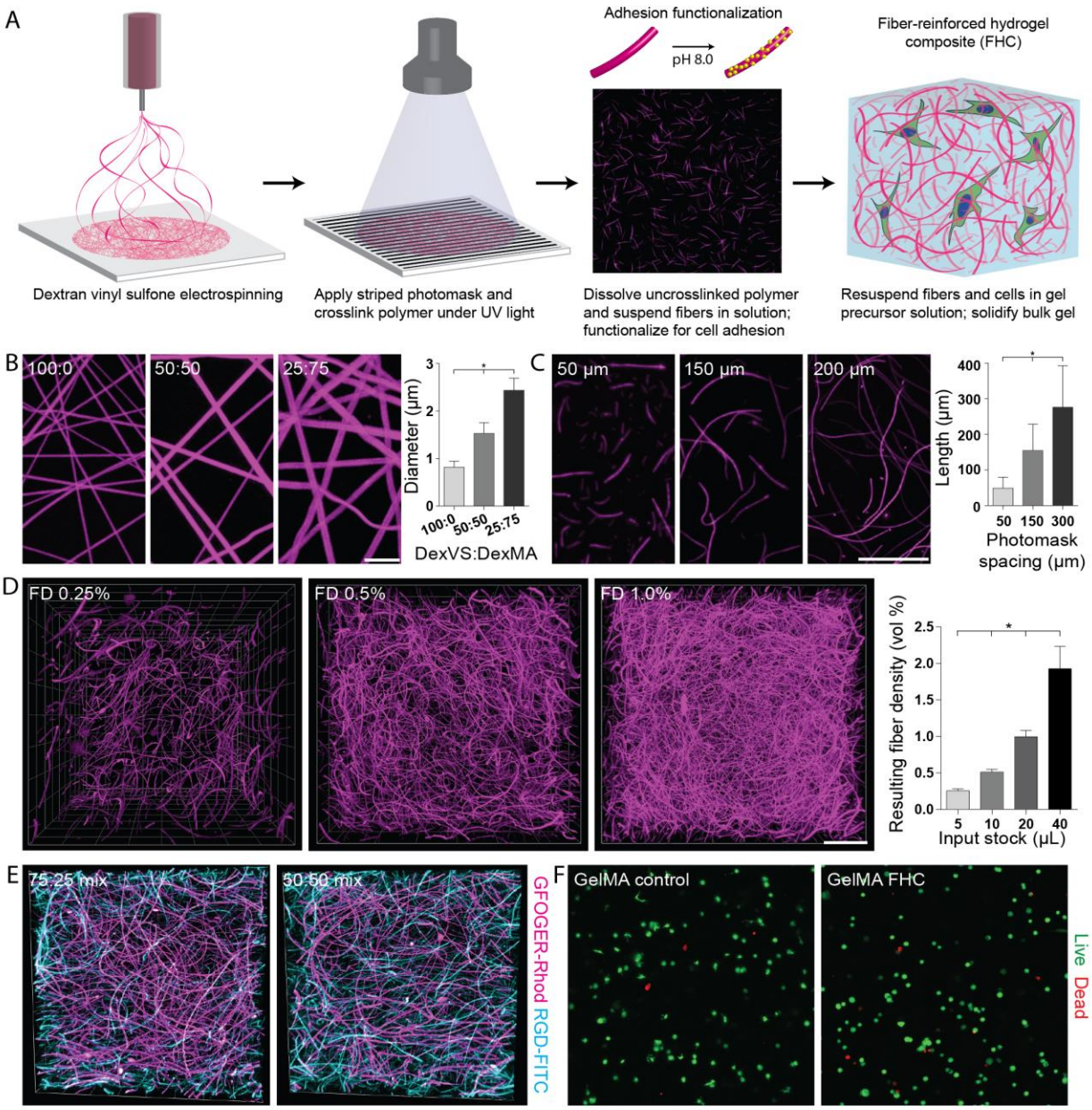

Figure 3.1 A novel approach to generating 3D fibrous microenvironments with tunable architectural features. (a) Schematic overview of the fiber hydrogel composite (FHC) fabrication process. (b) Images and quantification of electrospun fibers of three distinct diameters, created by electrospinning solutions of varying viscosity (scale bar: 10 μm). (c) Confocal projections and quantification of suspensions of fiber segments at varying lengths (scale bar: 100 μm). (d) Quantification and 500 μm confocal Z-stack 3D renderings of FHCs at three distinct fiber densities (0.25, 0.5, and 1 % fibers by volume) (scale bar: 100 μm). (e) 500 μm confocal Z-stack 3D renderings of 1 % vol FHCs containing two distinct fiber populations tagged with two different thiolated peptides, GFOGER (magenta) and RGD (cyan). (f) Live/dead stain of fibroblasts encapsulated in control and fiber-reinforced hydrogels. All data presented as mean ± std; * indicates a statistically significant comparison with $p<0.05$

Resulting suspensions of crosslinked fibers can then be functionalized with cell adhesive ligand CGRGDS (RGD) via a thiol-ene click reaction, and co-encapsulated alongside cells within a choice hydrogel material, which forms the bulk component of the fibrous composite **(Figure 3.1A)**. In order to capture the diverse fiber architectures that exist across tissue types and throughout disease progression, we optimized the FHC fabrication process to generate a considerable parameter space with orthogonal control over fiber diameter (0.8-3 μm), length (50-300 μm), and encapsulation density (0.25-2.0 % volume) across the physiologic range **(Figure 3.1B-E)** (Comley & Fleck, 2010; Furtado et al., 2012; Mayorca-Guiliani et al., 2017; Mercer et al., 1990; Provenzano et al., 2008; Wolf et al., 2009) . Additionally, as native ECM contains a mixture of fibrous proteins each with distinct adhesive ligands, we also demonstrated the ability to integrate, at desired ratios, multiple fiber populations each displaying unique thiolated adhesive peptides within a single FHC **(Figure 3.1E)**. This approach allows for the encapsulation of fibers presenting virtually any thiolated peptide or growth factor, and thus can be easily tailored for a variety of cell culture applications.

To examine how the incorporation of fiber segments influences cell spreading in 3D, we generated FHCs utilizing semi-synthetic gelatin methacrylate (GelMA) as the bulk component given its versatility and widespread use in bioprinting and tissue-engineering applications (Yue et al., 2015). GelMA‘s homology to collagen also provides endogenous adhesive and degradation sites, making it a suitable polymer for use in an ECM model. The viability of human dermal fibroblasts encapsulated within GelMA FHCs was not impacted by incorporation of DexVS fibers **(Figure 3.1F)**. As the primary resident cell type of stromal and interstitial tissues, we employed human fibroblasts in all subsequent studies. Time-lapse microscopy immediately following encapsulation revealed increased cell outgrowth and spreading within fiber-reinforced

as compared to in non-fibrous control hydrogels **(Figure 3.2A)**. To examine whether this response was consistent across other commonly employed hydrogels, we also generated FHCs with reconstituted basement membrane (rBM, a complex mixture of naturally derived matrix proteins which forms via macromolecular protein assembly) or fully synthetic polyethylene glycol (PEG8VS-RGD, formed via Michael-type addition chemistry with protease-sensitive thiolated crosslinkers and RGD) as the bulk component. Despite considerable distinctions in polymer structure, adhesive ligands, gelation mechanisms, and degradation kinetics between these three bulk materials, the inclusion of DexVS fibers consistently resulted in a doubling of 3D spreading compared to control hydrogels lacking fibers **(Figure 3.2B)**. Similar results were achieved with human umbilical vein endothelial cells (hUVEC) and human mesenchymal stem cells (hMSC), indicating that fiber-reinforcement could prove beneficial in tissue engineering applications **(Supplementary Figure 3.1)**. However, despite a consistent increase in spreading, the effect of fiber-reinforcement on cell morphology was dependent on the bulk hydrogel component. For example, control rBM gels appeared too compliant (~300 pa) to support cell spreading, but upon fiber reinforcement, rapid cell spreading and the formation of cell-cell contacts was observed within 1 day of culture, coinciding with marked fiber reorganization **(Supplementary Figure 3.2)**. Dramatic remodeling of the ECM is consistent with descriptions of early morphogenetic events during development when tissue mechanical properties are comparatively low (Czirók, Rongish, & Little, 2004). In contrast, such fiber reorganization events were not observed in more rigid PEG-8VS-RGD and GelMA FHCs.

As fibrous proteins are widely considered to be the major ECM constituent supporting cell adhesion *in vivo*, we further inquired whether cell adhesivity within the bulk hydrogel was a prerequisite to cell spreading in these 3D settings. We generated adhesive (PEG8VS-RGD) and

non-adhesive (PEG8VS) gels with or without DexVS-RGD fiber-reinforcement. While cells proved unable to spread in non-fibrous gels lacking RGD in the bulk, reinforcement with RGD-presenting fibers rescued cell spreading as evidenced by increased cell lengths, although not to equivalent levels of FHCs containing RGD in both fiber and bulk components (Supplementary **Figure** 3). These results indicate that bulk adhesive ligand enhances but is not essential for cell spreading in fiber-reinforced gels. Conversely, to investigate whether integrin engagement to RGD-presenting fibers mediated the observed increases in cell spreading, we generated GelMA and PEG8VS-RGD FHCs with DexVS fibers lacking RGD. Despite the presence of RGD within the bulk, reinforcement with fibers lacking RGD did not significantly increase spread area relative to non-fibrous controls **(Supplementary Figure 3.3)**. This indicates that fiber-reinforcement primarily increases cell spreading rates through integrin engagement directly to RGD presented on fibers.

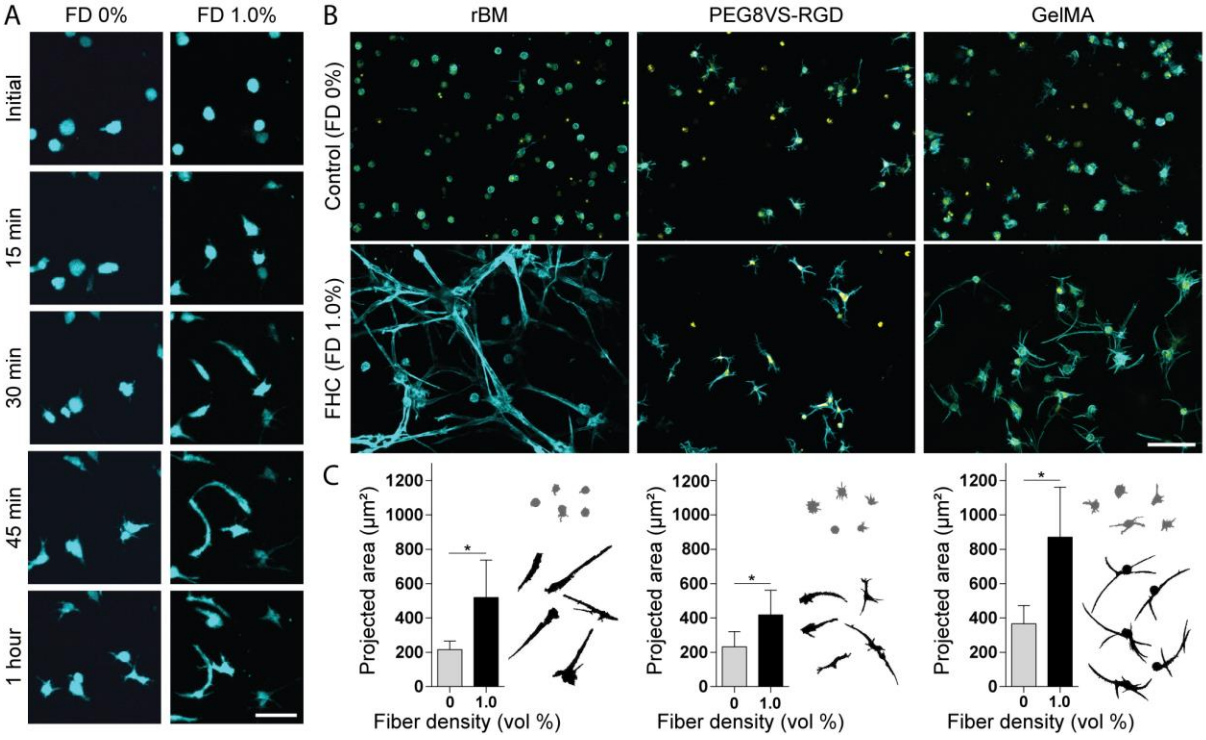

Figure 3.2: Fiber-reinforcement promotes single cell outgrowth and spreading in a variety of 3D hydrogel matrices. (a) Representative time-lapse images of fibroblasts spreading in

control and fiber-reinforced hydrogels (F-actin (cyan), scale bar: 50 μm). (b) Representative Z-stack projections of cells spreading in control and fiber-reinforced rBM (day 2), PEG8VS-RGD (day 7), and GelMA (day 4) hydrogels (F-actin (cyan) and nuclei (yellow), scale bar: 100 μm). (c) Quantification of cell spread area in control and fiber-reinforced hydrogels along with outlines of five representative cells from each condition. All data presented as mean ± std; * indicates a statistically significant comparison with $p<0.05$.

To investigate whether fiber-mediated cell spreading was simply due to a higher concentration of RGD presented on fibers relative to the bulk hydrogel (2mM on DexVS fibers vs. 0.5mM on the PEG-8VS background), we utilized a protease sensitive DexVS hydrogel and generated blank control and fiber-reinforced hydrogels over a range of bulk RGD concentrations (0, 1, 2, 4 mM). The abundance of functional groups within the DexVS polymer backbone (~250 VS moieties/chain) allowed for increasing RGD functionalization at a constant gel crosslinking and weight percentage, something not easily achieved with PEG-8VS hydrogels which are more stochiometrically constrained (due to maximally eight VS moieties per polymer chain). Fiber-reinforcement increased cell spreading across all bulk ligand concentrations **(Supplementary Figure 3.3)**, including in gels where the RGD coupling concentration was higher in the bulk hydrogel than on fibrous elements (4mM vs. 2mM). While cell spreading in 3D materials requires proteolytic activity and is often limited compared to in unconstrained 2D contexts, these results establish fiber-reinforcement as a straightforward route to accelerating and enhancing 3D cell spreading; fiber-reinforcement increased spreading in RGD-rich environments (GelMA, PEG8VS-RGD, DexVS-RGD) and rendered otherwise physically inert (rBM) or biochemically inert (PEG8VS, DexVS) materials supportive of cell spreading.

Considerable previous work has documented profound effects of hydrogel crosslinking on cell behavior, with high crosslinking (and resulting substrate stiffness) increasing cell spreading and associated signaling on 2D substrates, but hindering spreading in 3D contexts due

to the requirement for proteolytic degradation of crosslinks (Engler et al., 2006; Paszek et al., 2005). Therefore, we investigated whether fiber-reinforcement could enhance 3D spreading rates despite increases in bulk crosslinking and stiffness. We generated FHCs at three crosslinking densities via altering the degree of GelMA polymerization; differences in crosslinking were confirmed by increases in elastic modulus as a function of LAP photoinitiator concentration (**Figure 3.3A,B**). As fiber-reinforcement is a common strategy to increase biomaterial mechanical properties, we performed bulk mechanical testing and found that DexVS fiber-reinforcement did not alter bulk mechanical properties **(Figure 3.3B),** likely due to encapsulation of fibers at low density (1 % volume). In agreement with previous studies,

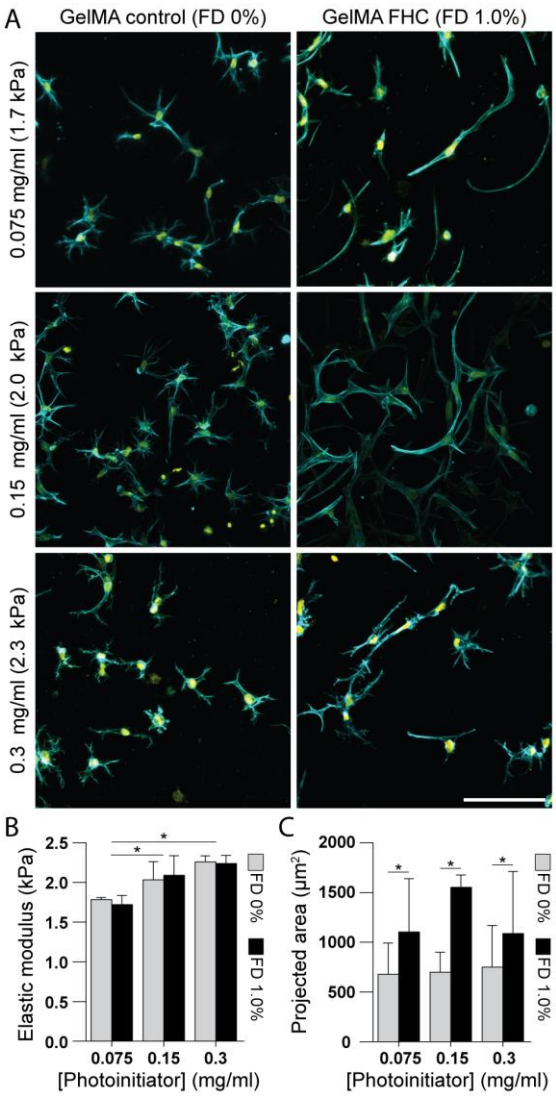

Figure 3.3: Fiber-mediated cell spreading occurs across a range of hydrogel crosslinking densities. (a) Representative Z-stack projections of steady state cell spreading in control and fiber-reinforced GelMA hydrogels polymerized with increasing photoinitiator concentrations (F-actin (cyan) and nuclei (yellow), scale bar: 100 μm). 1.7, 2.0, and 2.3 kPa hydrogels were fixed and imaged at day 1, day 4, and day 10, respectively. (b) Quantification of elastic modulus as a function of photoinitiator concentration and fiber density via bulk compression testing. (c) Quantification of cell spread area in control and fiber-reinforced gels. All data presented as mean ± std; * indicates a statistically significant comparison with $p<0.05$.

increased crosslinking density within the bulk hydrogel markedly hindered cellular spreading rates (Caliari, Vega, Kwon, Soulas, & Burdick, 2016); cells encapsulated in 0.3 mg ml-1 LAP

(2.4 kPa) gels spread nearly 10x slower (10 days vs. 1 day) compared to in 0.075 mg ml-1 LAP (1.7 kPa) gels. However, even at the highest crosslinking density examined, fiber-reinforcement led to an approximately two-fold increase in spread area compared to non-fibrous controls (**Figure** 3.3a,c), further demonstrating fiber-reinforcement to be a robust approach to accelerating 3D cell spreading independent of material composition **(Figure 3.2)**, crosslinking, and bulk mechanical properties.

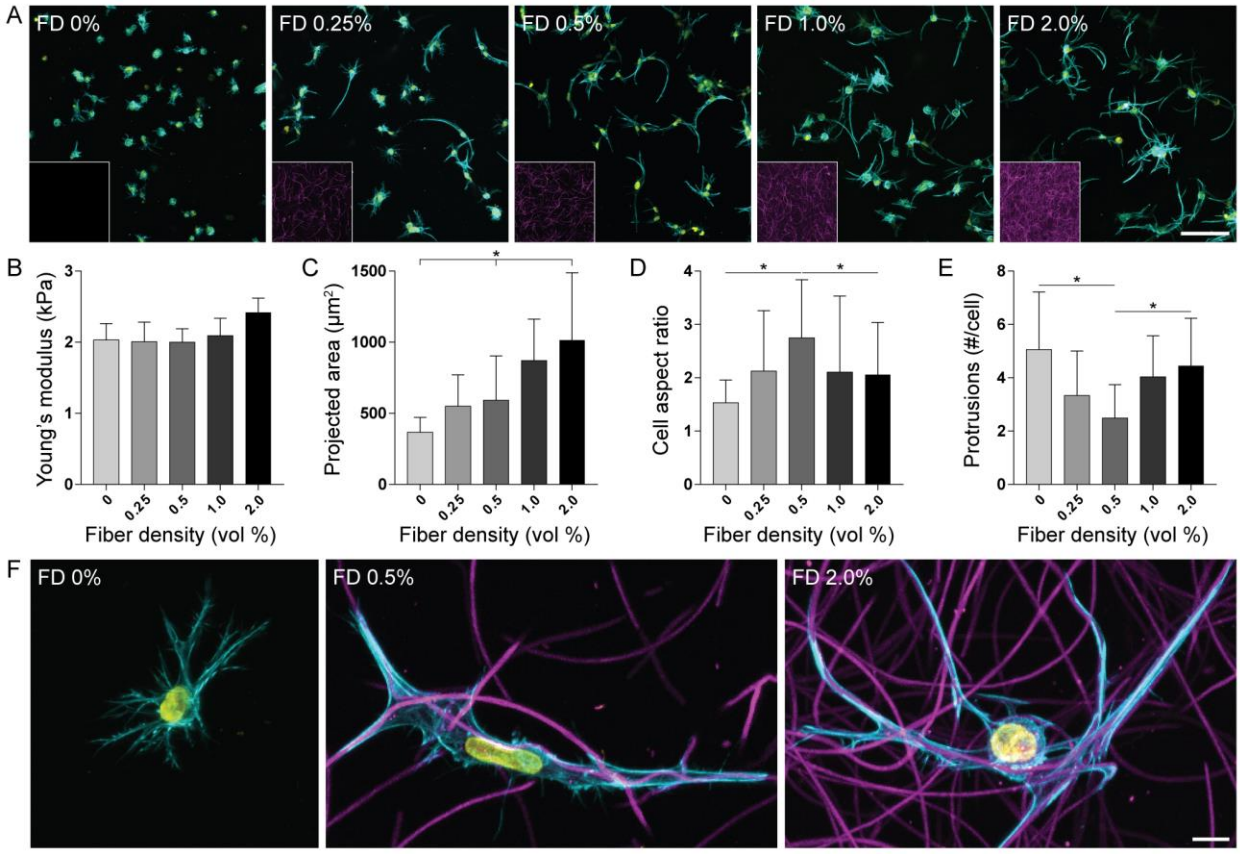

Figure 3.4: Distinct cell morphologies arise as a function of fiber density in 3D. (a) Representative Z-stack projections of day 4 cellular spreading in GelMA hydrogels with increasing fiber densities (F-actin (cyan) and nuclei (yellow), scale bar: 100 μm). Inset: representative image of rhodamine-labeled fibers (magenta) at each density. (b) Young's modulus as a function of fiber density determined by bulk compression testing. Quantifications of cellular spread area (c), cellular aspect ratio (d), and number of protrusions per cell (e) as a function of fiber density. (F) High-resolution confocal Z-stack projections of representative cells in samples with no, intermediate, and high fiber density (F-actin (cyan), nuclei (yellow), dexVS fibers (magenta), scale bar: 10 μm). All data presented as mean ± std; * indicates a statistically significant comparison with $p<0.05$.

While incorporation of fibers promoted cell spreading across an array of bulk hydrogel materials in the above studies, cells may be exquisitely sensitive to fiber density, a microenvironmental cue known to vary across tissues and with disease status. To evaluate the effect of fiber density on cell morphology, we encapsulated fibroblasts in GelMA FHCs with fiber volume fractions ranging from 0.25 % to 2 % volume (**Figure 3.4A**). Across this range of fiber densities the elastic modulus remained constant, suggesting orthogonal control over fiber density and bulk mechanical properties **(Figure 3.4B)**. Interestingly, while increasing levels of fiber-reinforcement led to concomitant increases in spread area, we noted a biphasic response with respect to cellular aspect ratio and protrusion number (**Figure** 3.4c,d,e). Distinct cellular morphologies emerged as a function of fiber reinforcement; cells in both high density fiber-reinforced gels (1-2 % volume) and non-fibrous control gels possessed lower aspect ratios as compared to gels with an intermediate density of fibers (0.5 % volume). The number of protrusions per cell inversely mirrored cell aspect ratio, with conditions leading to high aspect ratios corresponding to low total numbers of protrusions. Corroborating these measures, high resolution confocal imaging revealed equiaxially spread cells in control gels, uniaxially extended cells in gels at intermediate fiber conditions, and equiaxial morphologies at high fiber densities **(Figure 3.4A,F)**. Cell extensions in fiber-reinforced conditions appeared to track along fibers in similar fashion to observations of contact guidance along collagen fibers from intravital imaging studies (Nakatsuji & Johnson, 1984; W. Wang et al., 2002; Weigelin, Bakker, & Friedl, 2012).

Likely, variations in the number of fibers directly adjacent to cells account for these distinct morphologies. In control gels, the complete absence of topographical cues resulted in the formation of small protrusions in all directions. FHCs with high fiber density provided cells with an abundance of guidance cues and led to the formation of larger protrusions in all directions,

yielding greater spreading but a similar equiaxial morphology. In contrast, low to intermediate fiber densities provided cells with limited fibrous cues, thereby restricting contact guidance effects to one or two nearby fibers, ultimately resulting in more uniaxial cell morphologies. Interestingly, these morphological changes mirrored observations in 3D reconstituted type-I collagen gels, where low concentration gels led to less spread but more uniaxial cell morphologies, while high concentration gels possessing higher fiber densities led to greater cell area, protrusion counts, and branching structures **(Supplementary Figure 3.3)** (Miron-Mendoza, Seemann, & Grinnell, 2010). These results contrast 3D synthetic hydrogels where increased polymer concentration or crosslinking density typically results in hindered spreading rates, and highlights the importance of fibrous physical guidance cues in 3D, an important physiologic variable frequently overlooked when modeling the ECM *in vitro*.

Increased interstitial fiber density is a hallmark of tumor desmoplasia and fibrotic plaque development in the lung, liver, and heart, and as such, collagen density and tissue stiffness are prognostic markers used to stage disease progression in the clinic (Humphrey et al., 2014; Provenzano et al., 2008; Rockey et al., 2015). The major cellular player thought to mediate this ECM transformation are mechanosensitive fibroblasts, normally quiescent cells that differentiate toward activated myofibroblasts in response to physical and inflammatory microenvironmental stimuli. Indeed, several studies have shown pro-fibrotic soluble factors alone are insufficient to drive transformation; synergy between both biochemical and physical cues is required (Fang, Yuan, Peng, & Li, 2014; J. Jiang, Parker, Fuller, Kawula, & H, 2008; Parker et al., 2014; Seager, Hajal, Spill, Kamm, & Zaman, n.d.). While the role of hydrogel stiffness on myofibroblast activation has been extensively studied on 2D elastic surfaces (with increasing substrate stiffness leading to robust fibroblast activation in part through YAP transcriptional activity (F. Liu et al.,

2015a; van Grunsven, 2017)), the effect of 3D stromal architecture has not been previously described. As the accumulation of myofibroblasts *in vivo* is both dependent upon and a driver of increased fibrous ECM deposition, we asked whether increased fiber density (independent of bulk stiffness) could drive activation and disease signaling in otherwise normal fibroblasts.

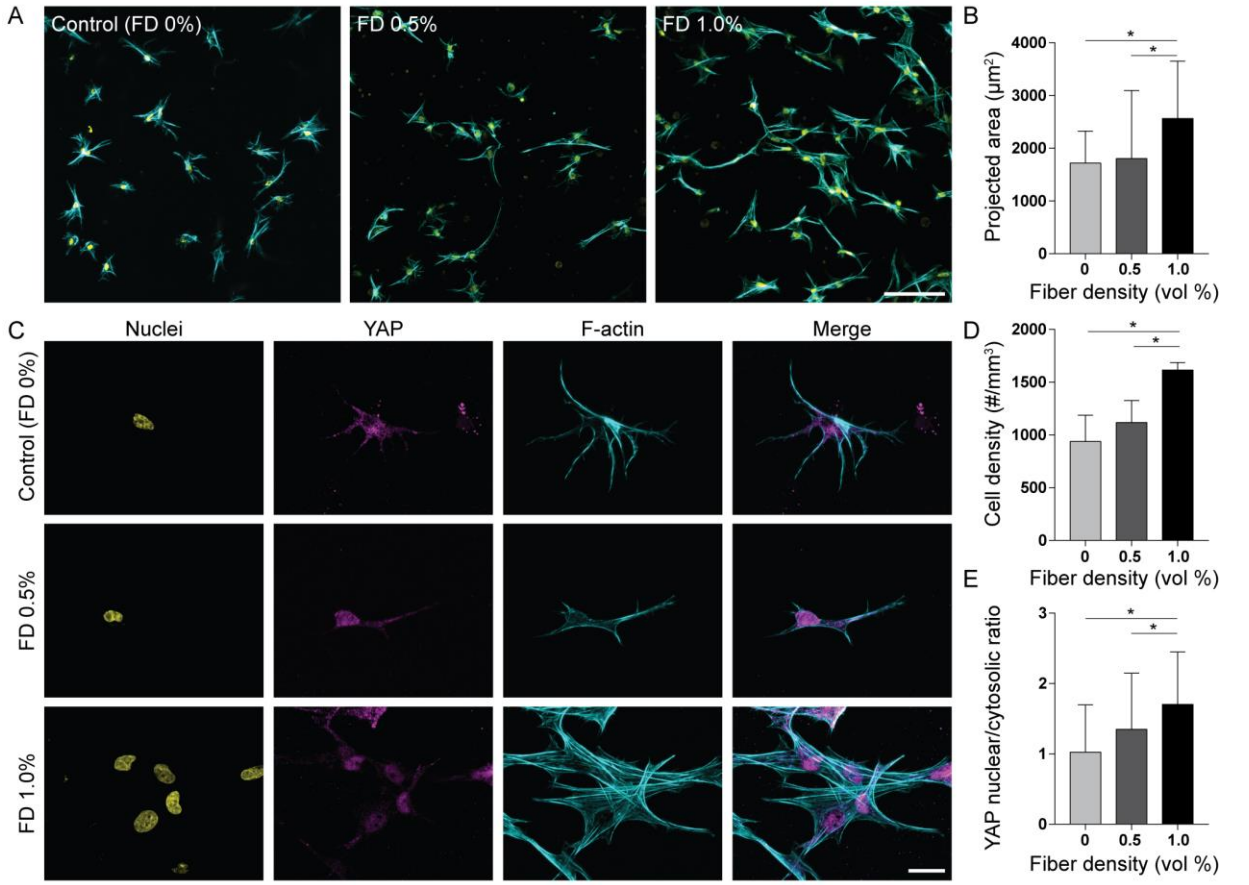

Figure 3.5: Fiber-reinforcement stimulates fibroblast activation in 3D, independent of bulk stiffness. (a) Representative Z-stack projections of cells spreading in 2 kPa GelMA hydrogels at increasing fiber densities in the presence of TGFβ-1 at day 7 (F-actin (cyan) and nuclei (yellow), scale bar: 100 μm). (b) Corresponding quantification of cellular spread area as a function of fiber density. (c) High-resolution confocal Z-stack projections of nuclei (yellow), YAP (magenta), F-actin (cyan), and merged F-actin and YAP channels within control and fiber-reinforced hydrogels (scale bar: 10 μm). Quantification of cell density (d) and YAP nuclear/cytosolic ratio (e) in non-fibrous controls and fiber-reinforced gels. All data presented as mean ± std; * indicates a statistically significant comparison with $p<0.05$.

To model the transition from healthy to fibrotic stromal ECM, normal fibroblasts were encapsulated in non-fibrous control, low (0.25 % volume) and high (1 % volume) density fiber-reinforced GelMA hydrogels and then subjected to soluble TGFβ-1, a potent mediator of myofibroblast activation *in vivo* (Meng, Nikolic-Paterson, & Lan, 2016). We then immunostained for YAP to assay fibroblast activation, a hippo pathway transcriptional regulator known to promote myofibroblast differentiation, proliferation, and ECM synthesis (Calvo et al., 2013; F. Liu et al., 2015a; Piersma, Bank, & Boersema, 2015; Plouffe, Hong, & Guan, 2015). Supporting the studies above, fibroblasts in control gels exhibited lower spread area compared to in FHCs, even at late time points and in the presence of TGFβ-1 (a known inducer of cell spreading (Rys, Monteiro, & Alliston, 2016)) **(Figure 3.5A, B)**.

Consequently, YAP nuclear localization was nearly two-fold higher in composites with high fiber density (1 % volume) compared to in non-fibrous controls **(Figure 3.5C, E)**. Potentially due to proliferative signaling stemming from YAP transcriptional activity, we also noted increased cell density and aggregates of activated cells within the high fiber density condition **(Figure 3.5D)**, reminiscent of dense cell plaques observed histologically in fibrotic tissues. In composites with lower fiber density (0.25 % volume), significant differences in spread area, YAP nuclear translocation, and cell density relative to non-fibrous controls were not observed. As healthy stromal ECM is naturally fibrous, composites with low fiber volume fraction may reflect a homeostatic architecture. Taken together, these findings are in line with numerous *in vivo* studies noting that myofibroblast activation only occurs beyond a threshold fiber density, and contrasts prior work *in vitro* establishing bulk stiffness as the primary regulator of nuclear YAP translocation (Rys et al., 2016).

Furthermore, this work highlights a distinction between bulk mechanical properties conferred by hydrogel crosslinking and cell-scale mechanical properties influenced by local fibrous architecture. While many *in vitro* studies have identified bulk crosslinking/stiffness as a fundamental physical regulator of cell spreading, morphology, and phenotype, we noted similar cell morphologies across different bulk materials **(Figure 3.2)** and with variations in crosslinking/stiffness **(Figure 3.3)**. Conversely, when maintaining bulk stiffness constant across a range of fiber densities, we documented vastly different morphologies **(Figure 3.4)** and phenotypes **(Figure 3.5)**. These observations support previous work showing that cells primarily sense and respond to local rather than bulk mechanical properties as they form cell-ECM adhesions, generate traction forces, and undergo contact guidance (Baker et al., 2015; Doyle, Carvajal, Jin, Matsumoto, & Yamada, 2015; Miller, Jeftinija, & Mallapragada, 2002). While bulk mechanical properties can be influential in shaping cell response, local topographical cues are invariably present *in vivo*, and appear to play a similar fundamental role in regulating morphology and cell-ECM mechanosensing.

3.5 Conclusion

In this work, we introduced a versatile method for fabricating 3D fibrous hydrogel composites (FHCs) with orthogonal control over numerous parameters including bulk material, ligand, elastic modulus, and fiber architecture (diameter, length, density). Across hydrogel crosslinking densities and material platforms, robust increases in cell spreading were observed in FHCs, demonstrating fiber-reinforcement as a novel approach to control 3D cell shape independent of bulk material. Consequently, this method has likely implications in tissue engineering where control over spreading dependent cell processes (e.g. stem cell differentiation,

vasculogenesis, wound closure) is critical for therapeutic efficacy. In accordance with *in vivo* observations, higher fiber-reinforcement densities also led to notable increases in fibroblast activation at constant elastic modulus, thus highlighting the importance of fiber density as a critical material design parameter. Indeed, while the ECM has proven challenging to model controllably with naturally derived materials and accurately with synthetic hydrogels, fiber-reinforced composites appear to be a vital next step in physiologic biomimetic modeling.

3.6 Materials and Methods

3.6.1 Reagents

All reagents were purchased from Sigma Aldrich and used as received, unless otherwise stated.

3.6.2 Synthesis of modified dextran and gelatin

DexVS**:** A previously described protocol for vinyl sulfonating polysaccharides was adapted for use with linear high MW dextran (MW 86,000 Da, MP Biomedicals, Santa Ana, CA) (Yu & Chau, 2012). Briefly, pure divinyl sulfone (12.5 ml, Fisher Scientific, Hampton, NH) was added to a sodium hydroxide solution (0.1 M, 250 mL) containing dextran (5 g). This reaction was carried out at 1500 RPM for 3.5 minutes, after which the reaction was terminated by adjusting the pH 5.0 via the addition of HCL. DexMA: Dextran was methacrylated using previously described protocols (Baker et al., 2015). Briefly, dextran (30 g) and 4-dimethylaminopyridine (3 g) were dissolved in anhydrous dimethyl sulfoxide (150 mL) overnight. Next, glycidyl methacrylate (36.9 mL) was added under vigorous stirring, heated to 45 ˚C and allowed to react for 24 hours. The solution was then cooled to 4 ˚C and precipitated into chilled (4 ˚C) 2-propanol (1 L). The crude product was recovered by centrifugation, re-dissolved in milli-Q water. GelMA: Methacrylated

gelatin was synthesized according to previously described methods (Nichol et al., 2010). Briefly, type A porcine skin gelatin (5 g) was dissolved in PBS (50 mL) at 60 ^{o}C under stirring for one hour. Methacrylic anhydride (1 mL) was added dropwise and allowed to react for 1 hour. The reaction was terminated by 5x dilution with warm PBS. All reaction products were dialyzed for 5 days against milli-Q water, with two water exchanges daily, and then lyophilized for 3 days to obtain the pure product.

NMR: Functionalization of DexVS, DexMA, and GelMA was characterized by ^{1}H –NMR spectroscopy in D_2O. The degree of methacrylate functionalization was calculated as the ratio of the proton integral (6.174 and 5.713 ppm) and the anomeric proton of the glucopyranosyl ring (5.166 and 4.923 ppm). As the signal of the anomeric proton of α-1,3 linkages (5.166 ppm) partially overlaps with other protons, a predetermined ratio of 4% α-1,3 linkages was assumed as previously described (van Dijk-Wotthuis et al., 1995) and the total anomeric proton integral was calculated solely based on the integral at 4.923 ppm. A methacrylate/dextran repeat unit ratio of 0.7 was determined. The degree of vinyl sulfone functionalization was calculated as the ratio of the proton integral (6.91 ppm) and the anomeric proton of the glucopyranosyl ring (5.166 and 4.923 ppm), here a vinylsulfone/dextran repeat unit ratio of 0.376 was determined. For GelMA, a 57.8% degree of methacrylate functionalization was calculated as previously described where the degree of functionalization is equal to 1 – (lysine methylene proton of GelMA)/(lysine methylene proton of Gelatin) x 100% (Hoch, Hirth, Tovar, & Borchers, 2013).

3.6.3 Fiber segment fabrication

DexVS was dissolved at 0.6 g ml^{-1} in a 1:1 mixture of milli-Q water and dimethylformamide with 0.015% Irgacure 2959 photoinitiator. Methacrylated rhodamine (0.5 mM; Polysciences, Inc., Warrington, PA) was incorporated into the electrospinning solution to

fluorescently visualize fibers. This polymer solution was utilized for electrospinning within an environment-controlled glovebox held at 21 ˚C and 30-40% relative humidity. Electrospinning was performed at a flow rate of 0.3 ml h^{-1}, gap distance of 7 cm, and voltage of -8.0 kV onto a grounded collecting surface. Fiber layers were collected on glass slabs and primary crosslinked under ultraviolet light (100mW cm^{-2}) through a photomask and then secondary crosslinked (100mW cm^{-2}) in a 1mg mL^{-1} Irgacure 2959 solution. After polymerization, fiber segments can be handled similarly to cells, microspheres, or microgels and were resuspended in a known volume of PBS (typically 3 ml). The total volume of fibers was then be calculated via a conservation of volume equation: total resulting solution volume = volume of fibers + volume of PBS (3 ml). After calculating total fiber volume, solutions were re-centrifuged, supernatant was removed, and fiber pellets were resuspended to create a 10 vol% fiber solution, which were then aliquoted and stored at 4^{o} C. To modulate fiber segment length, photomasks of different gap sizes (50, 150, 300 μm) were added on top of fiber layers before crosslinking. To control fiber diameter, the viscosity of the electrospinning solution was increased at constant dextran weight percentage via tuning the DexMA:DexVS ratio (3:1, 1:1, 0:1), with larger ratios leading to higher solution viscosities and increases in fiber diameter. For all cell studies, a 0:1 ratio (100% DexVS) was used. To support cell adhesion, 2.0 mM RGD (CGRGDS, CPC Scientific, Sunnyvale, CA) was coupled to vinyl sulfone groups along the DexVS backbone via Michael-type addition chemistry.

3.6.4 Hydrogel formation

GelMA hydrogels were formed at 5% w/v in the presence of ultraviolet light (5 mW cm-2) and lithium phenyl-2,4,6-trimethylbenzoylphosphinate (LAP) photoinitiator at a concentration of 0.15 mg ml-1. PEG-8VS (40,000 Da, JenKem USA, Plano, TX) hydrogels were formed via a thiol-ene click reaction at 3.25% w/v with 0.75mM RGD, 0.005M sodium hydroxide, and

stoichiometric amounts of VPMS crosslinker peptide (GCRDVPMSMRGGDRCG, Genscript, George Town, KY). DexVS gels were formed via an analogous click reaction at 3.5% w/v with 10mM VPMS crosslinker and varying amounts of RGD (0.0-4.0mM). Gelation of rBM (Matrigel, Corning, Corning NY) and Collagen (Type-I rat tail collagen, Corning, Corning NY) was carried out by incubation at 37°C for at least 30 minutes. All hydrogel precursor solutions were made in PBS. To create fibrous hydrogels, a defined stock solution (10 vol %) of suspended fibers in PBS was mixed into hydrogel precursor solutions prior to gelation. Via controlling the dilution of the fiber suspension, fiber density was readily tuned within the hydrogel at a constant hydrogel weight percentage.

3.6.5 Cell culture and biological reagents

Human dermal fibroblasts were cultured in DMEM containing 1% penicillin/streptomycin, L-glutamine and 10% fetal bovine serum (Atlanta biologics Flowery Branch, GA). HDFs were passaged upon achieving confluency at a 1:4 ratio and used for studies until passage 6. For all studies, cells were trypsinized, counted and encapsulated into gels at a density of 500,000 cells ml-1, and subsequently cultured at 37°C and 5% CO2.

3.6.6 Fluorescent staining, microscopy, and analysis

Cells within control and fiber-reinforced gels were fixed with 4% paraformaldehyde for 30 min at room temperature. To ensure we were not quantifying a transient cellular morphology, experimental time points were selected based upon the time required to reach a steady-state cellular spread area, i.e. when cells were no longer significantly increasing in size as a function of time. To stain the actin cytoskeleton and nuclei, samples were permeabilized in PBS solution containing Triton X-100 (5% v/v), sucrose (10% w/v), and magnesium chloride (0.6% w/v), blocked in 1% BSA, and stained simultaneously with phalloidin and DAPI. To immunostain for

YAP, samples were fixed and permeabilized as described above, blocked for 12 h in 10% fetal bovine serum, and incubated with 1:1000 rabbit anti-YAP antibody (ab52771, Abcam, Cambridge, UK). A Zeiss LSM 800 laser scanning confocal microscope with an environmental chamber was used for all imaging. For cell spreading analyses, 300µm Z-stacks were taken with a 10x objective. High-resolution images of YAP and actin morphology were acquired with a 40x objective. Time-lapse microscopy was performed at 15-minute frame intervals over 14 hours, immediately prior to imaging, cell were labeled CellTracker Green CMFDA (5-chloromethylfluorescein diacetate) dye. Unless otherwise specified, images are presented as maximum intensity projections with actin labeled in cyan, cell nuclei in yellow, and fibers in magenta. All cell and fiber morphometric analyses (fiber size, cell area) were performed using custom Matlab scripts with sample sizes > 50 cells/group. Average fiber density and cell density values were calculated via confocal microscopy and custom Matlab analysis scripts. For example, DAPI-stained cell nuclei were thresholded and counted in six separate 600 x 600 x 200 µm image volumes, allowing us to calculate a total number of cells per mm3 of gel volume.

3.6.7 Mechanical Testing

Hydrogel composites were mechanically tested using a custom device consisting of a linear actuator with sub-nanometer resolution (Smaract, Oldenberg, Germany) and a 5.0 N loadcell (Novatech Measurements Limited, East Sussex, UK). Hydrogels molded into cylinders (6 mm diameter, 3 mm height) were tested in unconfined compression between two impermeable platens. Samples were subjected to 10% strain applied at 0.05%/s. Stress was approximated as applied load normalized to initial cross-sectional area. Strain was approximated as change in sample height normalized to initial height. The elastic modulus was determined from linear fits over the 0-5% strain range of the stress-strain curve.

3.6.8 Statistics

Statistical significance was determined by one-way analysis of variance (ANOVA) or Student's t-test where appropriate, with significance indicated by $p<0.05$. All data are presented as mean ± standard deviation.

3.7 Supplementary Figures

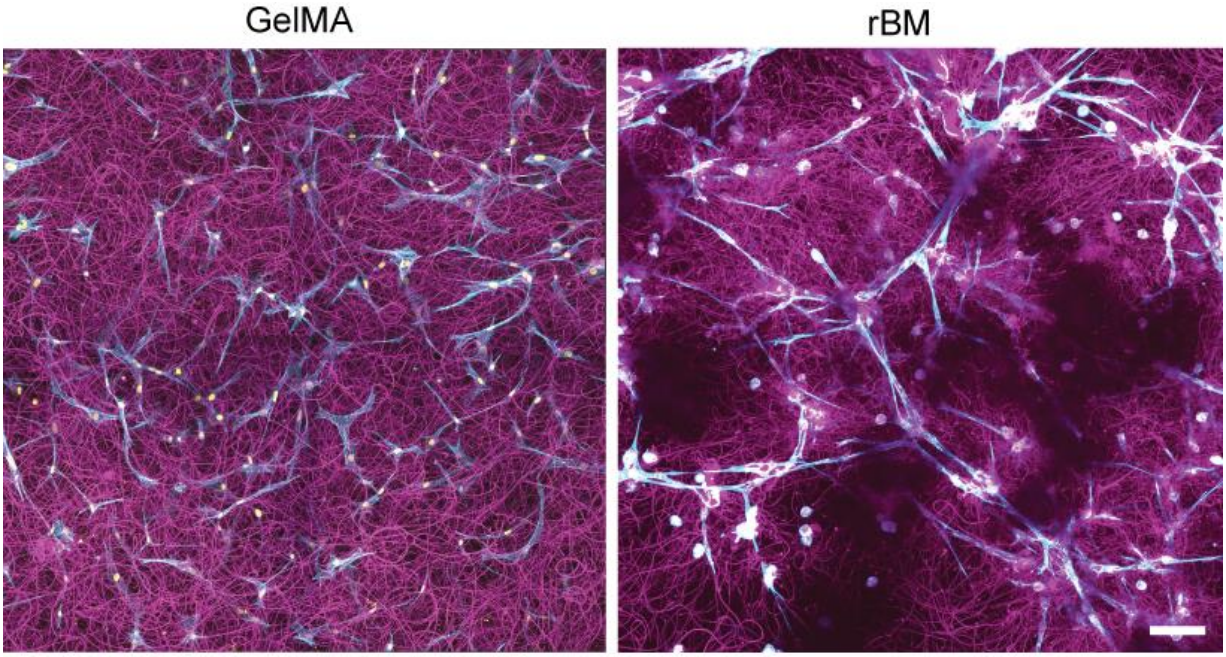

Supplemental Figure 3.1: Cells within fiber-reinforced hydrogels of varying bulk material. Fibroblasts in compliant rBM FHCs heavily remodeled fibrous architecture during the spreading process, in contrast to in GelMA FHCs where cells spread with limited fiber recruitment.

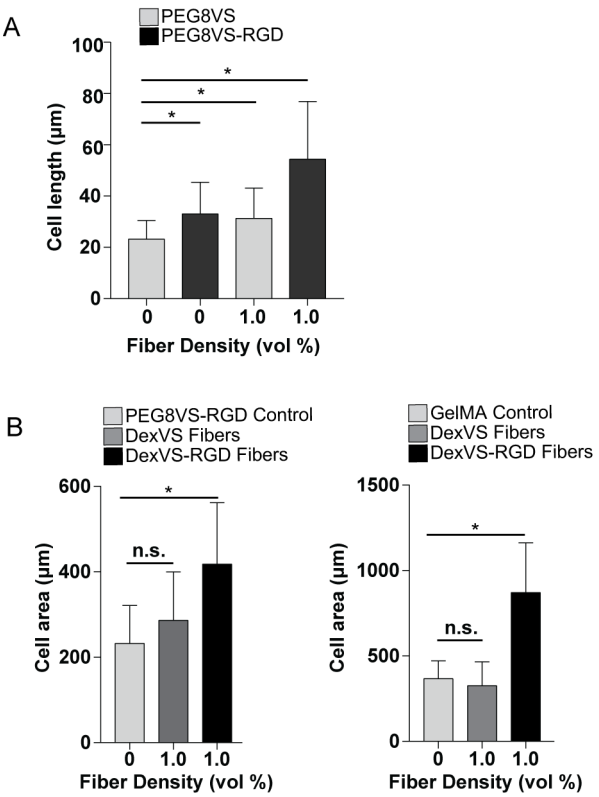

Supplemental Figure 3.2: RGD location controls cellular spreading responses in FHCs. (a) Fibroblasts in non-adhesive PEG8VS hydrogels (lacking bulk RGD) demonstrated limited spreading compared to in non-adhesive PEG8VS gels reinforced with adhesive fibers. Cell spreading was highest in adhesive PEG8VS-RGD reinforced with adhesive fibers. (b) PEG8VS-RGD and GelMA FHCs formed with non-adhesive fibers did not lead to increased cell spreading relative to non-fibrous control gels.

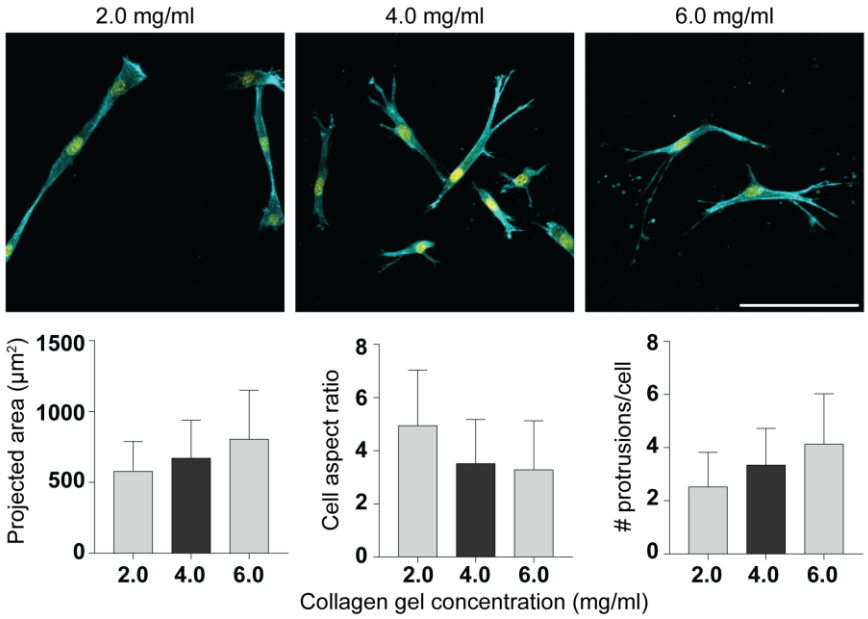

Supplemental Figure 3.3: Collagen concentration modulates cellular morphology. Increasing the concentration of type-I collagen gels lead to increases in cell area and the number of protrusions per cell, and lead to decreases in cellular aspect ratio (scale bar: 100 μm).

Chapter 4: The Role of Fiber Density and Matrix Proteolysis in a Bioengineered Model of Pulmonary Fibrosis

4.1 Authors

Daniel L. Matera, Katarina M. DiLillo, Makenzee R. Smith, Christopher D. Davidson, Ritika Parikh, Mohammed Said, Carole A. Wilke, Isabelle M. Lombaert, Kelly B. Arnold, Bethany B. Moore, Brendon M. Baker

4.2 Abstract

Fibrosis is often untreatable and is characterized by aberrant tissue scarring from activated myofibroblasts. Although the extracellular matrix becomes increasingly stiff and fibrous during disease progression, how these physical cues impact myofibroblast differentiation in 3D is poorly understood. Here we describe a multicomponent hydrogel that recapitulates the 3D fibrous structure hallmark to the interstitial tissue regions where idiopathic pulmonary fibrosis (IPF) initiates. In contrast to findings on 2D hydrogels, myofibroblast differentiation in 3D was inversely correlated with hydrogel stiffness, but positively correlated with matrix fiber density. Employing a multi-step bioinformatics analysis of IPF patient transcriptomes and *in vitro* pharmacologic screening, we identify matrix-metalloprotease activity to be essential for 3D but not 2D myofibroblast differentiation. Given our observation that compliant degradable 3D

matrices amply support fibrogenesis, these studies demonstrate a departure from the established relationship between stiffness and myofibroblast differentiation in 2D, and provide a new 3D model for studying fibrosis and identifying antifibrotic therapeutics.

4.3 Introduction

Fibrosis is implicated in nearly 45% of all deaths in the developed world and plays a role in numerous pathologies including pulmonary fibrosis, cardiac disease, atherosclerosis, and cancer (Wynn, 2008). In particular, interstitial lung diseases, such as idiopathic pulmonary fibrosis (IPF), are fatal and incurable with a median survival of only 2-5 years (Bagnato & Harari, 2015). Often described as dysregulated or incessant wound healing, fibrosis involves persistent cycles of tissue injury and deposition of extracellular matrix (ECM) by myofibroblasts (MFs). These critical cellular mediators of fibrogenesis are primarily derived from tissue resident fibroblasts (Wynn, 2008). MFs drive eventual organ failure through excessive fibrous extracellular matrix deposition, force generation and tissue contraction, and eventual disruption of parenchymal tissue function (Wynn, 2008). As organ transplantation remains the only curative option for late-stage disease, effective anti-fibrotic therapeutics that slow MF expansion or even reverse fibrosed tissue remain a major unmet clinical need. Undoubtedly, the limited efficacy of anti-fibrotic drugs at present underscores limitations of existing models for identifying therapeutics, the complexity of the disease, and an incomplete understanding of MF biology.

A strong correlation between lung tissue stiffening and worse patient outcomes suggests an important role for matrix mechanosensing in fibrotic disease progression (Fiore et al., 2018). Pre-clinical models of fibrosis in mice have supported the link between tissue stiffening and disease progression. However, a precise understanding of how physical cues from the microenvironment influence MF differentiation *in vivo* is confounded by concurrent structural (eg.

collagen density, laminin/elastin degradation) and biochemical (eg. matrix composition, inflammatory) changes to the microenvironment (Sundarakrishnan, Chen, Black, Aldridge, & Kaplan, 2018). Consequently, natural and synthetic *in vitro* tissue models have provided great utility for the study of MF mechanobiology. Seminal studies utilizing natural type I collagen gels have elucidated the role of pro-fibrotic soluble cues (e.g. TGF- β1) in promoting cell contractility, ECM compaction, and MF differentiation, and more recently, precision cut lung slices have emerged as a powerful tool to study the complexity of the pulmonary microenvironment in IPF (Liberati, Randle, & Toth, 2010; Sundarakrishnan et al., 2018). However, their utility in identifying physical microenvironmental determinants of MF differentiation suffers from an intrinsic coupling of multiple biochemical and mechanical material properties (Pathak & Kumar, 2011). Rapid degradation kinetics (1-3 days) and resulting issues with material stability (1-2 weeks) further impede the use of natural materials for studying fibrogenic events and drug responses, which occur over weeks to months in *in vivo models* or years in patients (Arora et al., 1999; Nakagawa, Pawelek, & Grinnell, 1989).

Synthetic hydrogels that are more resistant to cell-mediated degradation have provided a better controlled setting for long-term studies of disease-related processes (Ebrahimkhani, Young, Lauffenburger, Griffith, & Borenstein, 2014). For example, synthetic hydrogel-based cell culture substrates with tunable stiffness have helped establish a paradigm for mechanosensing during MF differentiation in 2D, where compliant matrices maintain fibroblast quiescence in contrast to stiffer matrices which promote MF differentiation (Balestrini et al., 2012; Castella, Buscemi, Godbout, Meister, & Hinz, 2010). Extensive findings in 2D suggest a causal role for matrix mechanics (eg. stiffness) during MF differentiation *in vitro* and potentially in human disease, but these models lack the 3D nature of interstitial spaces where fibrosis originates (Bochaton Piallat, Gabbiani, &

Hinz, 2016). The interstitium surrounding alveoli is structurally composed of two key components: networks of fibrous ECM proteins (namely type I collagen fibers) and interpenetrating ground substance, an amorphous hydrogel network rich in glycosaminoglycans such as heparan sulfate proteoglycan. Mechanical cues from fibrotic ECM that promote MF differentiation may arise from changes to the collagen fiber architecture or the gel-like ground substance; indeed, whether matrix stiffness is a prerequisite for MF differentiation in 3D fibrous interstitial spaces remains unclear (Giménez et al., 2017). Furthermore, the limited efficacy of anti-fibrotic therapies identified in pre-clinical and *in vitro* models of IPF motivates the development of 3D tissue-engineered systems with improved structural and mechanical biomimicry, relevant pharmacokinetics, and the potential to incorporate patient cells (Ebrahimkhani et al., 2014). Furthermore, recapitulating key features of the fibrotic progression in an *in vitro* setting that better approximates interstitial tissues could 1) improve our current understanding of MF mechanobiology and 2) serve as a more suitable test bed for potential anti-fibrotic therapeutics.

Accordingly, herein we describe a microengineered pulmonary interstitial matrix which recapitulates mechanical and structural features of fibrotic tissue as well as key biological events observed during IPF progression. Design parameters of these engineered microenvironments were informed by mechanical and structural characterization of fibrotic lung tissue from a bleomycin mouse model. We then investigated the influence of dimensionality, matrix crosslinking/stiffness, and fiber density on TGF- β□-induced MF differentiation in our pulmonary interstitial matrices. Surprisingly, increased hydrogel crosslinking/stiffness substantially hindered MF differentiation in 3D in contrast to findings in 2D, while fibrotic matrix architecture (i.e. high fiber density) potently promoted fibroblast proliferation and differentiation into MFs. Long-term (21 day) culture

of hydrogels possessing a fibrotic architecture engendered tissue stiffening, collagen deposition, and secretion of pro-fibrotic cytokines, implicating fiber density as a potent fibrogenic cue in 3D microenvironments. Pharmacologic screening in fibrotic pulmonary interstitial matrices revealed matrix metalloprotease (MMP) activity and hydrogel remodeling as a key step during 3D fibrogenesis, but not in traditional 2D settings. To explore the clinical relevance of our findings, we leveraged a multi-step bioinformatics analysis of transcriptional profiles from 231 patients, highlighting increased MMP gene expression and enriched signaling domains associated with matrix degradation in patients with IPF. Together, these results highlight the utility of studying fibrogenesis in a physiologically relevant 3D hydrogel model, underscore the requirement of matrix remodeling in IPF, and establish a new platform for screening anti-fibrotic therapies.

4.4 Results

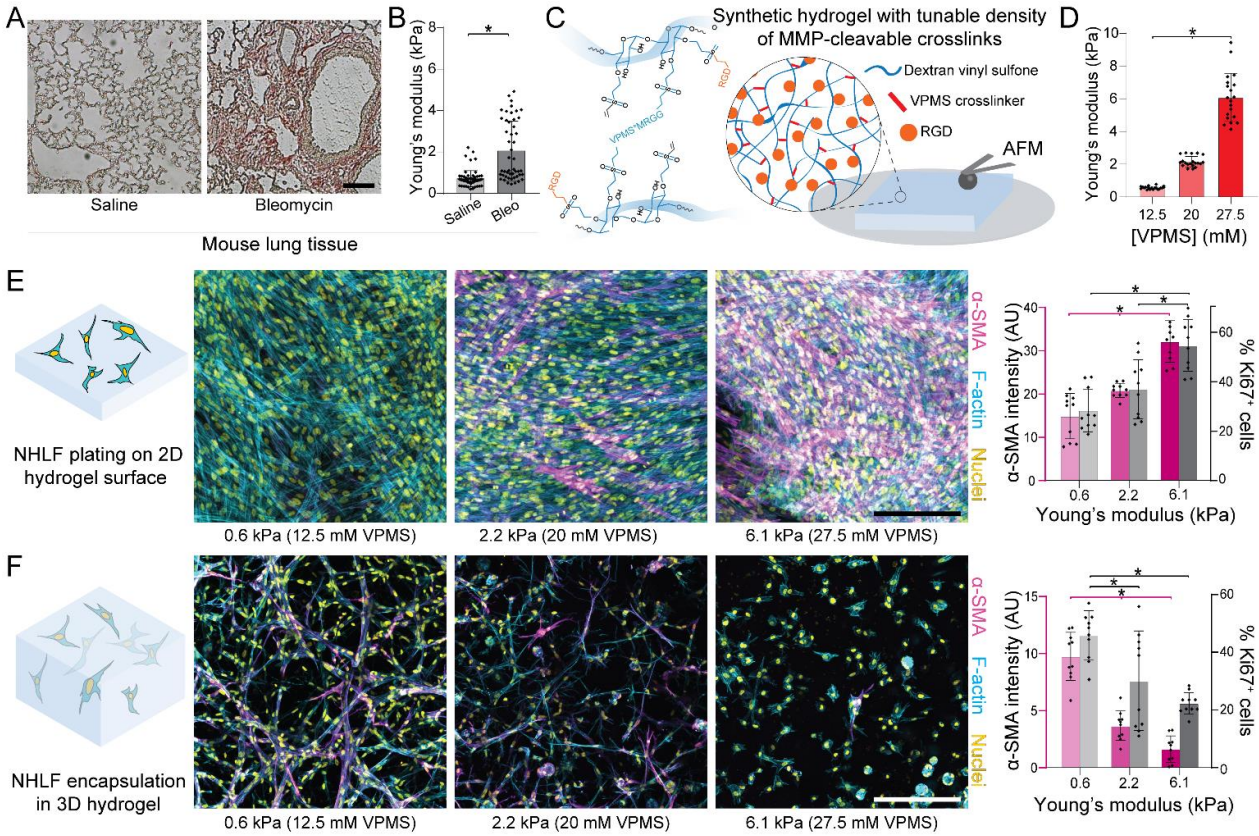

Figure 4.1: Matrix crosslinking and stiffness have opposing effects on myofibroblastic differentiation of fibroblasts plated on 2D vs. in 3D hydrogels. A) Histological preparations of healthy control and bleomycin-treated murine lung tissue (n=3 mice/group) stained for collagen by picrosirius red (scale bar: 100 μm). B) Young's modulus of mouse lung tissue as measured by AFM nanoindentation, with data fit to the Hertz contact model to determine Young's modulus (n=3 mice/group, n=50 indentations/group on n=9 tissue sections). C) Schematic of proteolytically sensitive, cell adhesive DexVS-VPMS bulk hydrogels. D) Young' s modulus determined by AFM nanoindentation of DexVS-VPMS hydrogels formed with different concentrations of VPMS crosslinker (n=4 samples/group, n=20 total indentations/group). E and F) Representative images of F-actin (cyan), nuclei (yellow) and α-SMA (magenta); image-based quantification of α-SMA expression (left axis, magenta bars, day 9) and nuclear Ki67 (right axis, grey bars, day 5) in 2D and 3D (n=4 samples/group, n=10 fields of view/group, n>50 cells/field of view; scale bars: 200 μm). All data presented are means ± standard deviations with superimposed data points; asterisk denotes significance with $p < 0.05$ determined by one-way analysis of variance.

To inform key design criteria for our pulmonary interstitial matrices, we began by characterizing mechanical properties of fibrotic interstitial tissue in a bleomycin-induced lung injury model in mouse. Naïve C57BL/6 mice were intratracheally challenged with bleomycin to

induce lung injury and subsequent fibro-proliferative repair, with saline treated animals maintained as a control group. After two weeks, animals were sacrificed and lung tissue was dissected out, sectioned and stained, and then mechanically tested by atomic force microscopy (AFM) nanoindentation to map the stiffness of interstitial tissue surrounding alveoli. Importantly, while single-dose bleomycin administration does not recapitulate human IPF, the fibro-proliferative response is well-characterized and leads to myofibroblast differentiation, collagen deposition, and lung stiffening events that are reminiscent of what occurs in human disease over longer time scales. As previously documented (F. Liu & Tschumperlin, 2011), bleomycin treatment corresponded to an increase in the thickness of interstitial tissue regions surrounding alveoli, a structural change which occurred alongside matrix stiffening **(Figure 4.1A-B)**; bleomycin treated lungs possessed elastic moduli nearly 5-fold greater than healthy control tissues. To generate synthetic hydrogels with elastic moduli tunable over this range, we functionalized a biocompatible and protein resistant polysaccharide, dextran, with pendant vinyl-sulfone groups amenable to peptide conjugation (termed DexVS, **Figure 4.1C**). To permit cell-mediated proteolytic hydrogel degradation and thus spreading of encapsulated cells, we crosslinked DexVS with a bifunctional peptide (GCVPMS↓MRGGCG, abbreviated VPMS) primarily sensitive to MMP9 and MMP14, two MMPs implicated in fibrosis-associated matrix remodeling (Corbel et al., 2001; Zigrino et al., 2016). Tuning input VPMS crosslinker concentration yielded stable hydrogels spanning the full range of elastic moduli we measured by AFM nanoindentation of lung tissue **(Figure 4.1D)**. Additional functionalization with cell adhesive moieties (CGRGDS, abbreviated RGD) facilitated adhesion of primary normal human lung fibroblasts (NHLFs) **(Figure 4.1E)**.

To confirm the role of matrix mechanics on cell proliferation and MF differentiation, we seeded patient-derived NHLFs on 2D DexVS protease-sensitive hydrogel surfaces varying in VPMS crosslinker density and resulting stiffness, and stimulated cultures with TGF- β1 to promote TGF- β1 MF differentiation. In accordance with prior literature, we observed a stiffness-dependent stepwise increase in cell proliferation (day 5) and MF differentiation (day 9) as measured by Ki67 and alpha-smooth muscle actin (α-SMA) immunofluorescence, respectively **(Figure 4.1E)** (Balestrini et al., 2012). As the influence of matrix elasticity on MF differentiation in 3D synthetic matrices has not previously been documented, we also encapsulated NHLFs in 3D within identical DexVS hydrogels. Surprisingly, the opposing trend with respect to stiffness was noted for cells encapsulated in 3D; compliant (E=560 Pa) hydrogels which limited α-SMA expression in 2D plated cells instead exhibited the highest levels of MF differentiation in 3D **(Figure 4.1F)**. Decreasing proliferation and cell-cell contact formation as a function of increasing hydrogel stiffness were also noted in 3D matrices, and may be one reason why rigid hydrogels limit differentiation in 3D. Similar findings have been reported for mesenchymal stem cells encapsulated in hyaluronic acid matrices, where compliant gels promoted stem cell proliferation and yes-associated protein (YAP) activity in 3D, yet inhibited YAP activity and proliferation in 2D (Caliari et al., 2016). These results suggest that while stiff, crosslinked 2D surfaces promote cell spreading, proliferation, and MF differentiation, an equivalent relationship does not directly translate to 3D settings. High crosslinking and stiffness (E=6.1 kPa) in 3D matrices sterically hinder cell spreading, proliferation, and the formation of cell-cell contacts, all well-established promoters of MF differentiation (Follonier, Schaub, Meister, & Hinz, 2008a).

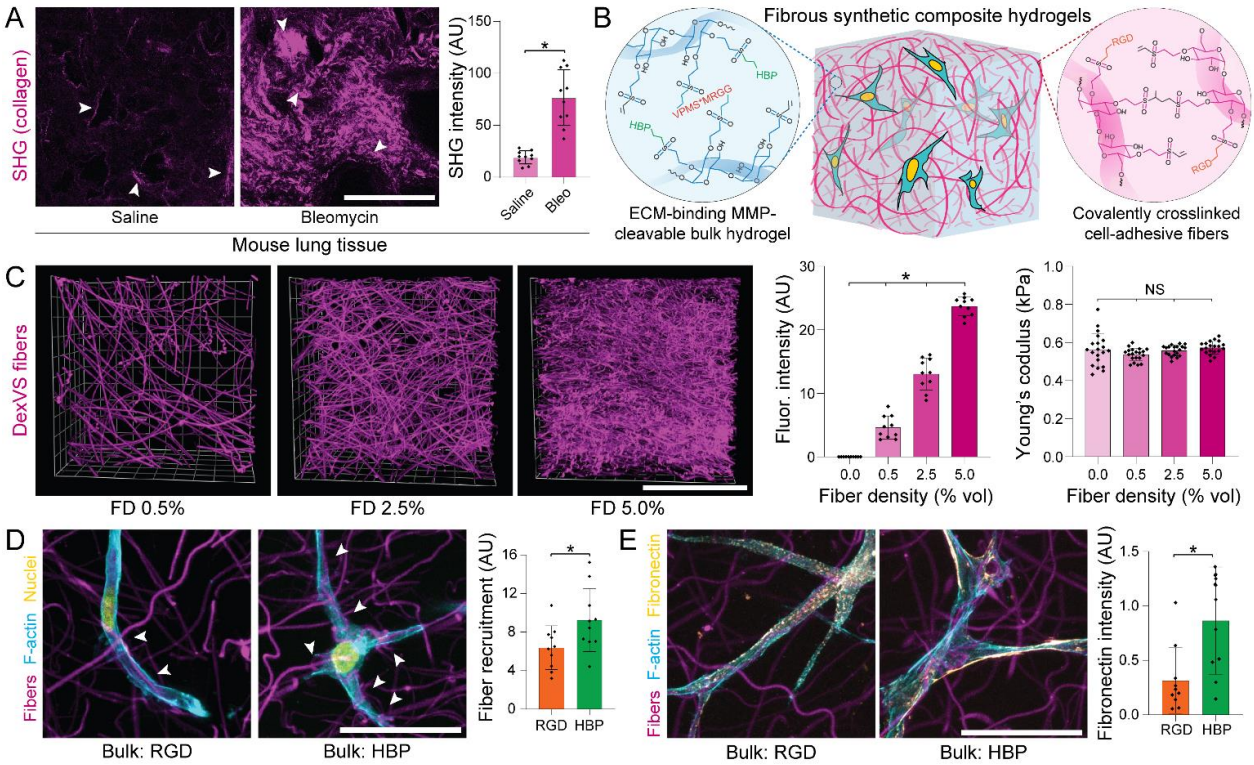

Figure 4.2: Microengineered fibrous hydrogel composites to model the lung interstitium. A) SHG imaging of collagen microstructure within healthy and bleomycin-treated lungs on day 14, with quantification of average signal intensity (arrows indicate interstitial tissue regions adjacent to alveoli; n=3 mice/group, n=10 fields of view/group; scale bar: 100 μm). B) Schematic depicting polymer crosslinking and functionalization for generating fibrous DexVS hydrogel composites to model changes in fiber density within lung interstitial tissue ECM. C) Images and intensity quantification of fluorophore-labeled fibers within composites varying in fiber density (n=4 samples/group, n=10 fields of view/group; scale bar: 100 μm). Young's modulus determined by AFM nanoindentation of fibrous composites formed with different concentrations of VPMS crosslinker (n=4 samples/group, n=20 measurements/group). D) Representative high resolution images of NHLFs on day 1 in fibrous composites formed with bulk hydrogels (12.5 mM VPMS) functionalized with integrin ligand arginylglycylaspartic acid (RGD) or heparin-binding peptide (HBP) (F-actin (cyan), nuclei (yellow) and DexVS fibers (magenta); scale bar: 50 μm). Quantification of fiber recruitment as measured by contact between cells and DexVS fibers (n=10 fields of view/group, n>25 cells analyzed). E) Representative high resolution images of NHLF on day 1 fibrous composites formed with bulk hydrogels functionalized with integrin ligand RGD or heparin-binding peptide HBP (F-actin (cyan), fibronectin (yellow) and DexVS fibers (magenta); scale bar: 5 μm). Quantification of fibronectin deposition into the hydrogel matrix as measured by immunostain intensity (n=10 fields of view/group, n>25 cells analyzed). All data presented are means ± standard deviations with superimposed data points; asterisk denotes significance with $p < 0.05$ determined by *o*ne-way analysis of variance or Student's t-test where appropriate*;* NS denotes non-significant comparison.

Cell-degradable synthetic hydrogels with elastic moduli approximating that of fibrotic tissue proved non-permissive to MF differentiation in 3D. Although matrix crosslinking and densification of ground substance has previously been implicated in fibrotic tissue stiffening, remodeled collagenous architecture can also engender changes in tissue mechanics and may modulate MF development in IPF independently. To characterize the fibrous matrix architecture within healthy and fibrotic lung interstitium, we utilized second-harmonic generation (SHG) microscopy to visualize collagen microstructure in saline and bleomycin-treated lungs, respectively. Per prior literature, saline-treated lungs contained limited numbers of micron-scale (~1 μm diameter) collagen fibers, primarily localized to the interstitial spaces supporting the alveoli **(Figure 4.2A)** (Kottmann et al., 2015). In contrast, bleomycin-treated lungs had on average 4-fold higher overall SHG intensity, with collagen fibers localized to both an expanded interstitial region and in disrupted alveolar networks. While no difference in fiber diameter was noted with bleomycin treatment, we did observe thick (~2-5 μm) collagen bundles containing numerous individual fibers in fibrotic lungs, potentially arising from physical remodeling by resident fibroblasts **(Figure 4.2A, Supplementary Figure 4.1)**. Given that typical synthetic hydrogels amenable to cell encapsulation (as in **Figure 4.1**) lack fibrous architecture, we leveraged a previously established methodology for generating fiber-reinforced hydrogel composites (Matera, Wang, Smith, Shikanov, & Baker, 2019). Electrospun DexVS fibers approximating the diameter of collagen fibers characterized by SHG imaging **(Supplementary Figure 4.1**) were co-encapsulated alongside NHLFs in DexVS-VPMS hydrogel matrices, yielding a 3D interpenetrating network of DexVS fibers ensconced within proteolytically cleavable DexVS hydrogel **(Figure 4.2B)**. To recapitulate the adhesive nature of collagen and fibronectin fibers within interstitial tissues, we functionalized DexVS fibers with RGD to support integrin

engagement and 3D cell spreading. Importantly, while increasing the weight % of type I collagen matrices increases collagen fiber density and simultaneously increases hydrogel stiffness **(Supplementary Figure 4.2)**, our synthetic matrix platform enables changes to fiber density (0.0-5.0%) without altering mechanical properties assessed by AFM nanoindentation **(Figure 4.2C)**, likely due to the constant weight percentage of DexVS and VPMS crosslinker within the bulk hydrogel.

Beyond recapitulating the multiphase structural composition of interstitial ECM, we also sought to mimic the adhesive ligand presentation and protein sequestration functions of native interstitial tissue. More specifically, the gel-like ground substance within fibrotic tissue intrinsically lacks integrin-binding moieties and is increasingly rich in heparan sulfate proteoglycans, primarily serving as a local reservoir for nascent ECM proteins, growth factors, and profibrotic cytokines. In contrast, synthetic hydrogels are often intentionally designed to have minimal interactions with secreted proteins and require uniform functionalization with a cell-adhesive ligand to support cell attachment and mechanosensing. We hypothesized that RGD-presenting fibers alone would support cell spreading (Matera et al., 2019) enabling the use of a non-adhesive bulk DexVS hydrogel functionalized with heparin binding peptide (HBP, CGFAKLAARLYRKAG) (Sakiyama-elbert & Hubbell, 2000). Indeed, while both RGD- and HBP-functionalized bulk DexVS gels supported cell spreading upon incorporation of RGD-presenting fibers, HBP-functionalized hydrogels encouraged matrix remodeling in the form of cell-mediated fiber recruitment **(Figure 4.2D)** and enhanced the deposition of fibronectin fibrils into the adjacent matrix **(Figure 4.2E)**. Given the multiphase structure of lung interstitium, changes in collagen fiber density noted with fibrotic progression, and the importance of physical

and biochemical matrix remodeling to fibrogenesis, we employed HBP-tethered 560 Pa DexVS-VPMS bulk hydrogels with tunable density of RGD-presenting fibers in all subsequent studies.

We next investigated whether changes in fiber density reflecting fibrosis-associated alterations to matrix architecture could influence MF differentiation in our 3D model. NHLFs were encapsulated in compliant DexVS-VPMS hydrogels ranging in fiber density (E= 560 Pa, 0.0-

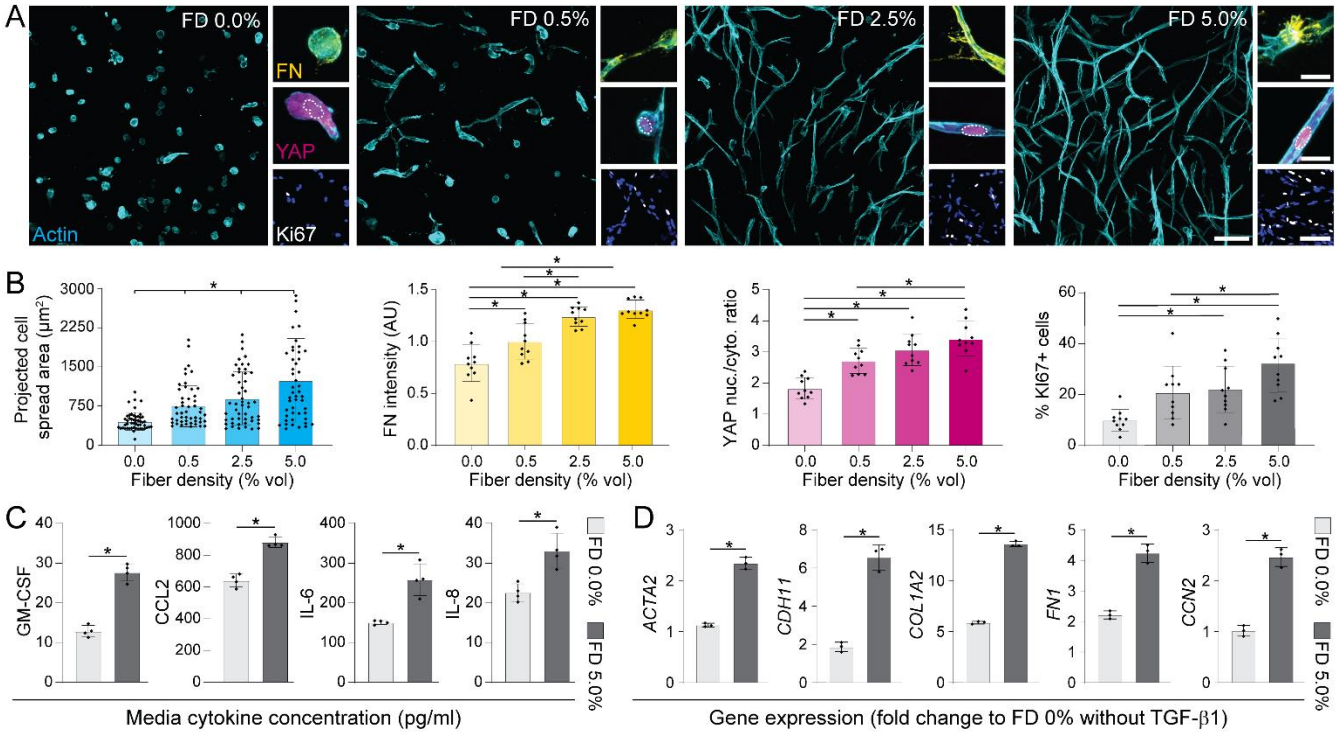

Figure 4.3: Increasing matrix fiber density in HBP-presenting 3D fibrous hydrogels primes fibroblasts for activation into myofibroblasts. A) Immunofluorescence images of NHLFs in hydrogel composites over a range of fiber densities after 3 days of culture (F-actin (cyan), fibronectin (FN, yellow), YAP (magenta), Ki67 (white) and nuclei (blue); scale bars: F-actin 100 μm, FN 20 μm, YAP 20 μm, Ki67/nuclei 100 μm). B) Corresponding image-based quantification of cell area, deposited FN, YAP nuclear to cytosolic ratio, and % of proliferating cells (n=4 samples/group; for cell spread area analysis, n>50 cells/group; for FN, YAP, and Ki67 analyses, n=10 fields of view/group and n>25 cells/field of view). C) Cytokine secretion into culture media on day 3 (all data was normalized to background levels in control media, n=4 samples/condition). D) Expression of myofibroblast-related genes in NHLFs stimulated with TGF-β1 on day 3, either in highly fibrous (FD 5.0%) or nonfibrous (FD 0.0%) hydrogels (data presented are GAPDH-normalized fold changes relative to NHLFs within a FD 0% hydrogel lacking TGF-β1 supplementation). All data presented are means ± standard deviations with superimposed data points; asterisk denotes significance with $p < 0.05$ determined by one-way analysis of variance or Student's t-test where appropriate.

5.0% vol fibers). Examining cell morphology after 3 days of culture, we noted increased cell

spreading **(Figure 4.3A-B)** and evident F-actin stress fibers **(Supplementary Figure 4.3)** in fibrous conditions compared to nonfibrous controls. Increased frequency of direct cell-cell interactions was also observed as a function of fiber density, as evidenced by higher area:perimeter ratios and the number of fibroblasts per contiguous multicellular cluster **(Figure 4.3A)**. As evidenced by changes in the ratio of nuclear to cytosolic YAP localization, we detected changes in mechanosensing as a function of fiber density, with the highest nuclear ratio measured in samples containing the highest fiber density examined. Given that nuclear YAP activity (a transcriptional co-activator required for downstream mechanotransduction) has been implicated as a promoter of MF differentiation (F. Liu et al., 2015b), we also assayed other markers associated with fibroblast activation. With increases in fiber density, we found significant increases in cell proliferation and local fibronectin deposition **(Figure 4.3A-B)**. Luminex quantification of cytokine secretion at this time point revealed elevated secretion of inflammatory and pro-fibrotic cytokines **(Figure 4.3C)**, suggesting that matrix fibers may modulate the soluble milieu known to regulate the response to tissue damage and repair *in vivo* (Gharaee-kermani, Mccullumsmith, Charo, Kunkel, & Phan, 2003; Luzina, Todd, Sundararajan, & Atamas, 2015; Sahin & Wasmuth, 2013). While no α-SMA expression or collagen deposition was observed at this early time point, F-actin stress fibers, YAP activity, and fibronectin expression have been previously established as proto-MF markers *in vivo* (Boris Hinz, 2007), suggesting that physical interactions with matrix fibers primes fibroblasts for activation into MFs. Indeed, supplying the pro-fibrotic soluble factor TGF-β1 prompted increases in the expression of various pro-fibrotic YAP-target genes *(ACTA2, COL1A1, FN1, CD11, CTGF)* relative to non-fibrous (FD 0.0%) controls at day 5 **(Figure 4.3D)**. Taken together, these data suggest heightened fiber density promotes a fibrotic phenotype **(Figure**

4.3, A to C) and gene expression **(Figure 4.3D)**, despite the absence of a stiff surrounding hydrogel.

To explore whether fibrotic matrix cues in the form of heightened fiber density could promote 3D MF differentiation over longer-term culture, NHLFs were encapsulated within hydrogels varying in fiber density and maintained in media supplemented with TGF-β beginning on day 1. Immunofluorescent imaging and cytokine quantification were performed on days 3, 5, 7 and 9 to capture dynamic changes in cellular phenotype and secretion, respectively. No α-SMA positive stress fibers or changes in total cytokine secretion were observed on day 3 or 5. On day 7, we noted the appearance of sparse (but insignificant) α-SMA positive cells alongside increased total cytokine secretion **(Figure 4.4D)** in FD 5.0% conditions containing TGF-β1, indicating the beginning of a potential phenotypic shift. Extensive MF differentiation (designated by α-SMA positive cells) and a 6-fold increase in total cytokine secretion occurred rapidly between day 7 and 9 **(Figure 4.4B, D-E)** in the highest fiber density (FD 5.0%) condition. Importantly, despite the high proliferation within high fiber density hydrogels **(Figure 4.4C)**, α-SMA positive cells were not evident in samples lacking exogenous TGF-β1 supplementation. Moreover, α-SMA positive cells were also absent in TGF-β1 supplemented conditions that lacked fibrous architecture, indicating a requirement for both soluble and physical fibrogenic cues in 3D. Furthermore, inhibiting integrin engagement by incorporating fibers lacking RGD also abrogated MF differentiation and proliferation despite the presence of TGF-β1 **(Figure 4.4A-B)**, suggesting that a fibrotic matrix architecture drives α-SMA expression primarily through integrin engagement and downstream mechanosensing pathways. These results were replicated with primary human dermal fibroblasts and mammary fibroblasts, where similar trends with α-SMA expression as a function of fiber density were observed **(Supplementary Figure 4.4)**. Interestingly, while high

fiber density promoted proliferation in dermal fibroblasts, mammary fibroblasts underwent MF differentiation in the absence of higher proliferation rates, demonstrating intrinsic differences between cell populations originating from different tissues. Nevertheless, these results suggest that fibrotic matrix architecture may be promoting MF differentiation in other pathologies, namely dermal scarring in systemic sclerosis and desmoplasia in breast cancer.

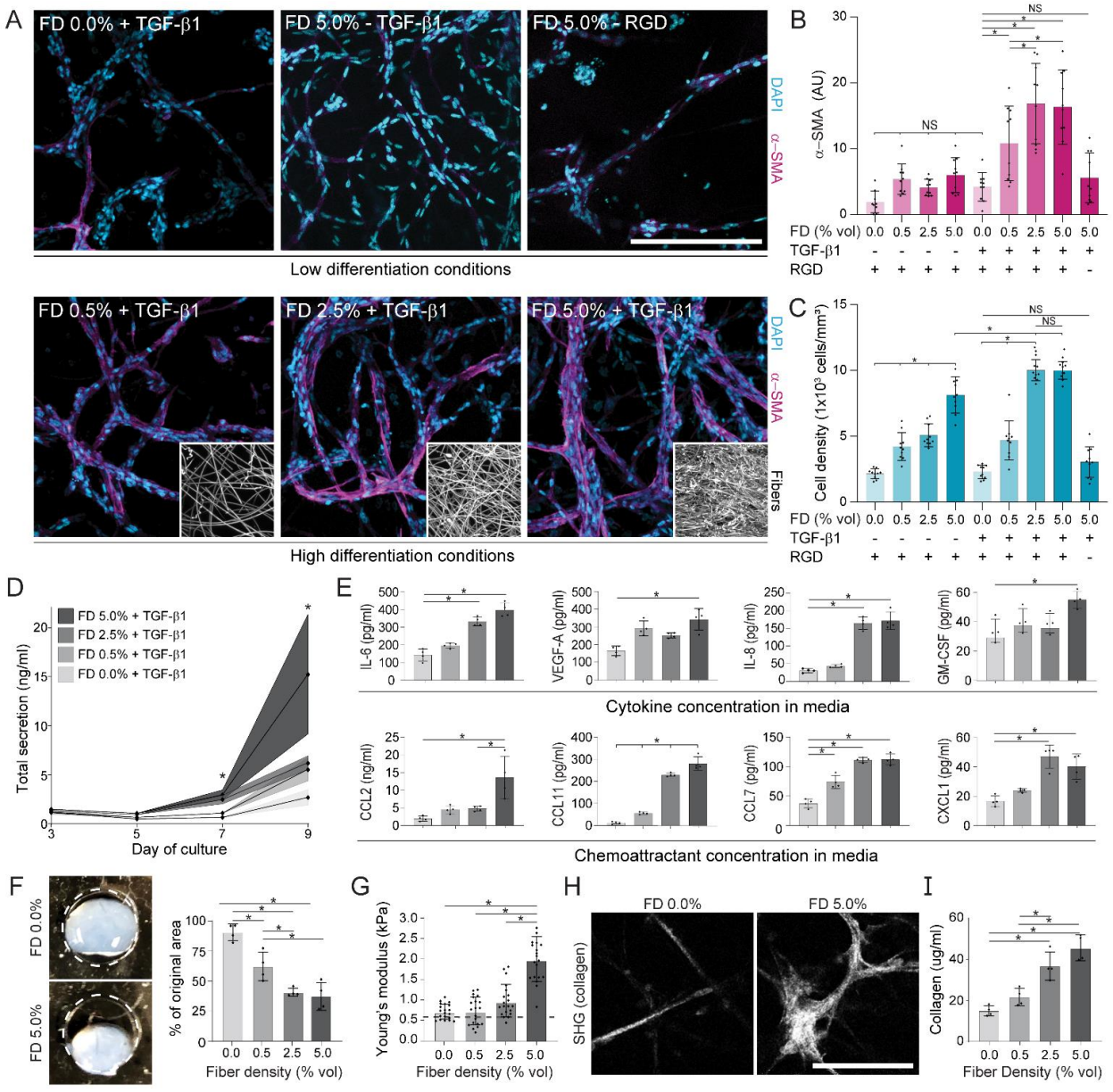

Figure 4.4: Profibrotic soluble and physical cues promote MF differentiation in 3D and initiate a progression of fibrosis-associated changes over long-term culture. A) Representative immunofluorescence images of NHLFs in microenvironmental conditions leading to low (top row)

or high (bottom row) MF differentiation after 9 days in culture (α-SMA (magenta) and nuclei (cyan); n=4 samples/group, n=10 fields of view/group and n>50 cells/field of view; scale bar: 200 μm), with corresponding image-based quantification in (B) and (C). Insets depict representative fiber densities. D) Measurement of total cytokine secretion over time as a function of fiber density (n=4 samples/condition, * indicates significant differences between FD 5.0% and all other groups at a given time point; NS denotes non-significant comparison). E) Secretion of specific cytokines and chemoattractants as a function of fiber density on day 9 (n=4 samples/condition). F) Representative images and quantification of tissue contraction within day 14 fibroblast-laden hydrogels of varying fiber density (n=4 samples/group, dashed line indicates initial diameter of 5 mm). G) AFM measurements of day 14 fibroblast-laden hydrogels of varying fiber density (n=20 measurements from n=4 samples/group). Dashed line indicates original hydrogel stiffness. H) SHG images of fibrous collagen within fibroblast laden hydrogels after 21 days of culture in media supplemented with ascorbic acid (scale bar: 100 μm). I) Measurement of total collagen content within digested DexVS hydrogels at day 21 as measured by biochemical assay (n=4 samples/group). All data presented are means ± standard deviations with superimposed data points; asterisk denotes significance with $p < 0.05$ determined by one-way analysis of variance; NS denotes non-significant comparison.

While proliferation and α-SMA expression are accepted markers of activated fibroblasts, fibrotic lesions contribute to patient mortality through airway inflammation, collagen secretion, tissue contraction, and lung stiffening – pathogenic events which hinder the physical process of respiration (Carone, Salerno, & Esquinas, 2016). Luminex screening of 41 cytokines and chemokines within hydrogel supernatant revealed elevated total cytokine secretion as a function of fiber density over time **(Figure 4.4D)**, many of which were soluble mediators known to regulate airway inflammation **(Figure 4.4E)** (Luzina et al., 2015). Numerous other cytokines were additionally secreted at day 9 but did not change as a function of fiber density despite differences in cell number at this timepoint **(Supplementary Figure 4.5)**, suggesting that cell number alone cannot account for the increased cytokine secretion in high fiber density conditions. By generating free-floating hydrogels which allow for contraction over time, we also examined macroscale changes in tissue geometry. Consistent with the influence of fiber density on α-SMA expression, hydrogels containing high fiber densities underwent greater hydrogel contraction compared to non-fibrous or low fiber density conditions **(Figure 4.4F)**. Day 14 fibrotic hydrogels (FD 5.0%) were also 4-fold stiffer (2.0 vs. 0.5 kPa) as measured by AFM nanoindentation **(Figure 4.4G)** compared

to conditions which yielded low rates of MF differentiation in shorter term studies (ie. FD 0.0 or FD 0.5% in **Figure 4.4A-B**). When media was supplemented with ascorbic acid to permit procollagen hydroxylation, collagen deposition into surrounding matrix was evident by SHG microscopy by day 21 in high fiber density hydrogels **(Figure 4.4H)** as compared to nonfibrous controls. Further biochemical analysis of hydrogel collagen content confirmed a stepwise increase in collagen production as a function of fiber density **(Figure 4.4I)**. Taken together, these findings demonstrate a clear influence of fiber density on MF differentiation and phenotype in 3D, and furthermore suggest that this *in vitro* model recapitulates key pathogenic events associated with the progression of fibrosis *in vivo.*

Having established microenvironmental cues that promote robust 3D MF differentiation, we next evaluated the potential of our fibrous hydrogel model for use as an anti-fibrotic drug screening platform. Nintedanib, a broad-spectrum receptor tyrosine kinase inhibitor, and Pirfenidone, an inhibitor of the MAPK/NF-κB pathway, were selected due to their recent Food and Drug Admininstration approval for use in patients with IPF (Ogura et al., n.d.). We also included dimethyl fumarate, an inhibitor of the YAP/TAZ pathway clinically approved for treatment of systemic sclerosis, and Marimastat, a broad-spectrum MMP inhibitor which has shown efficacy in murine pre-clinical models of fibrosis (de Meijer et al., 2010; Grzegorzewska et al., 2017). We generated fibrotic matrices (560 Pa DexVS-VPMS-HBP bulk hydrogels containing 5.0% vol DexVS-RGD fibers) which elicited the highest levels of MF differentiation, matrix contraction, and collagen secretion in our previous studies **(Figure 4.4)**. As a comparison to the current standard for high throughput compound screening, we also seeded identical numbers of NHLFs on 2D tissue culture plastic in parallel. Cultures were stimulated with TGF- β1 on day 1,

and pharmacologic treatments were added on day 3, following extensive fibroblast spreading, cell-cell junction formation, and proliferation **(Figure 4.3A)**.

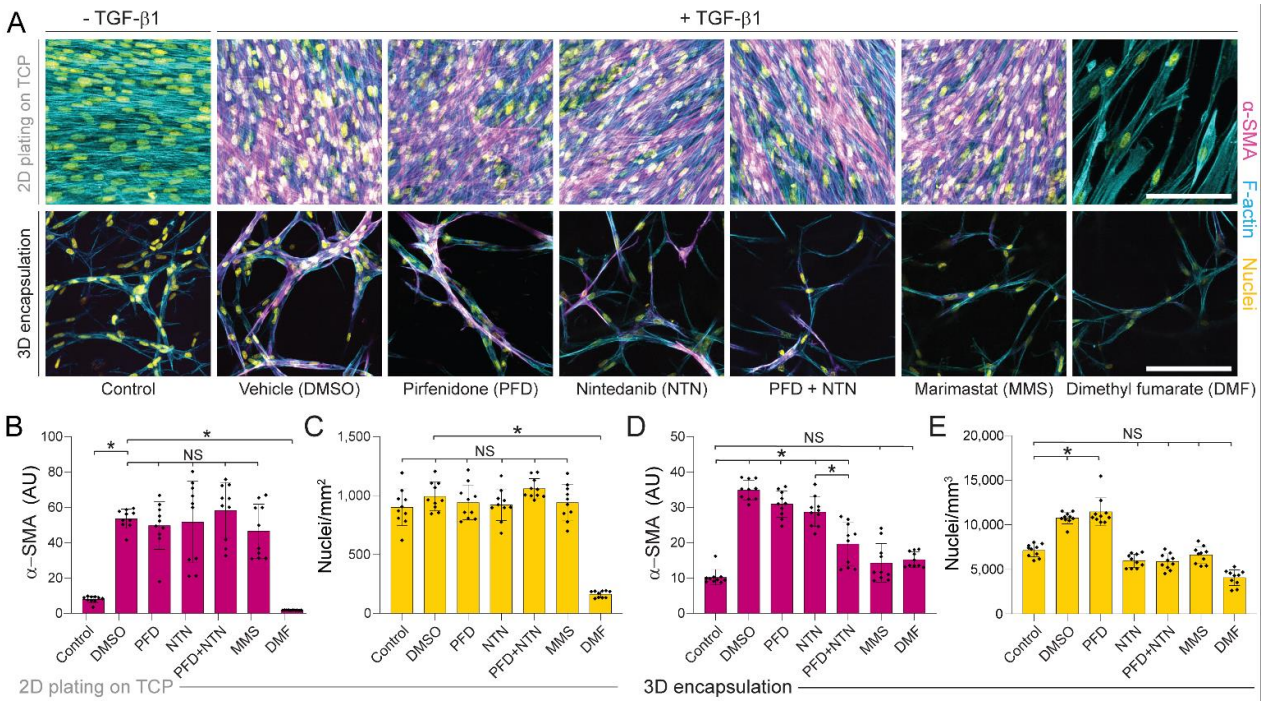

Figure 4.7: Pharmacologic treatment of NHLFs plated on tissue culture plastic (TCP) in 2D compared to encapsulated within 3D fibrous hydrogels reveals differential drug responses. A) Representative confocal images stained for α-SMA (magenta), F-actin (cyan), and nuclei (yellow) of NHLFs after 9 days of culture on TCP (top row) or 3D fibrotic matrices (bottom row) with pharmacologic treatment indicated from days 3 to 9 (scale bar: 100 μm). Imaged regions were selected to maximize the # of α-SMA+ cells/field of view within each sample. B) Quantification of α-SMA and C) total cell count within 2D NHLF cultures. D) Quantification of α-SMA and E) total cell count within 3D fibrotic matrices (n=4 samples/group, n=10 fields of view/group and n>50 cells/field of view). All data presented are means ± standard deviations with superimposed data points; asterisk denotes significance with $p < 0.05$ determined by one-way analysis of variance; NS denotes non-significant comparison.

As in our earlier studies, TGF- β1 supplementation promoted proliferation and α-SMA expression within 3D constructs as well as on on rigid tissue culture plastic **(Figure 4.5A)**. Interestingly, Nintedanib and Pirfenidone had differential effects on NHLFs depending on culture format; NHLFs on 2D tissue culture plastic were resistant to Pirfenidone/Nintedanib treatment with no difference in proliferation or α-SMA expression relative to vehicle controls, whereas modest but significant decreases in α-SMA expression (Pirfenidone, Nintedanib) and proliferation

(Nintedanib) were detected in 3D (**Figure 4.5, A to E)**. Combined treatment with Pirfenidone and Nintedanib provided an anti-fibrotic effect only in fibrotic matrices, supporting ongoing clinical studies exploring their use as a combinatorial therapy (ClinicalTrials.gov identifier NCT03939520). Dimethyl fumarate abrogated cell proliferation and α-SMA expression across all conditions, suggesting that inhibition of downstream mechanosensing inhibits MF differentiation in both 2D and 3D contexts in support of the general requirement for mechanosensing during MF differentiation independent of culture substrate (Balestrini et al., 2012). Indeed, inhibition of YAP activity *in vivo* has been shown to mitigate fibrosis and may be an advantageous therapeutic target (F. Liu et al., 2015b). Blockade of MMP activity via Marimastat treatment proved ineffectual in reducing α-SMA expression or proliferation on 2D tissue culture plastic, but surprisingly fully abrogated the proliferation and differentiation response in 3D fibrotic matrices **(Figure 4.5, A to E)**. Given the role of protease activity in tissue remodeling *in vivo* (de Meijer et al., 2010) and in cellular outgrowth within 3D hydrogels (Caliari et al., 2016; Madl et al., 2017), our data suggest that degradative matrix remodeling is a requirement for MF differentiation in 3D, but not in more simplified 2D settings. To summarize, multiple anti-fibrotic agents (Pirfenidone, Nintedanib, dimethyl fumarate, Marimastat demonstrating efficacy in clinical literature elicited an anti-fibrotic effect in our engineered fibrotic pulmonary interstitial matrices, but not in the 2D tissue culture plastic contexts traditionally used for compound screening.

As the protease inhibitor Marimastat fully ablated TGF- β1 induced α-SMA expression and proliferation in our 3D fibrotic matrices, we leveraged bioinformatics methodologies to investigate the role of matrix proteases in IPF patients on a network (Reactome) and protein (STRING) basis. Differential expression analysis of microarray data within the NCBI GEO (dataset # GSE47460) was used to generate an uncurated/unbiased dataset composed of the top

1000 differentially regulated genes in IPF, revealing *MMP1* as the most upregulated gene in IPF patients, with other matrix proteases (*MMP1, MMP3, MMP7, MMP9, MMP10, MMP11, MMP12*) and matrix remodeling proteins (*COL1A2, LOX, ACAN, DCN, HS6ST2*) similarly upregulated (**Figure 4.6B**). To focus on genes associated with MF differentiation for subsequent analyses, we performed GO term enrichment (via GEO2R) to compile a curated dataset containing 188 key genes associated with MF differentiation (Data File S1) and utilized Reactome and STRING analyses to investigate network signaling within both the uncurated and curated datasets. Analyses revealed 103 (uncurated) and 89 (curated) enriched signaling pathways in IPF (Data File S1). Interestingly, the top 3/5 (uncurated) and 5/5 (curated) significantly enriched pathways in IPF involved matrix degradation and remodeling (**Figure 4.6C**). Subsequent STRING protein-protein interaction analysis of datasets revealed that top signaling nodes were MMPs (uncurated: *MMP1, MMP3*; **Figure 4.6D**), fibrous collagens (uncurated: *COL1A2, COL3A1*), or cytokines (curated: *IL6, VEGFA, IL1B , IGF1*; **Figure 4.6D**) known to increase MMP expression in fibroblasts (Howard et al., 2012; Mia, Boersema, & Bank, 2014; Ohshima et al., 2016; Sundararaj et al., 2009). These results emphasize the interdependence between MMP activity and systems-level pathogenic signaling in IPF, and in combination with our 3D drug screening results, highlight fibroblast-specific protease activity as a potential therapeutic target. Furthermore, given that protease inhibition had no effect on MF differentiation in 2D culture, these data also support the growing sentiment that simplified 2D screening models may be masking the identification of potentially viable anti-fibrotics.

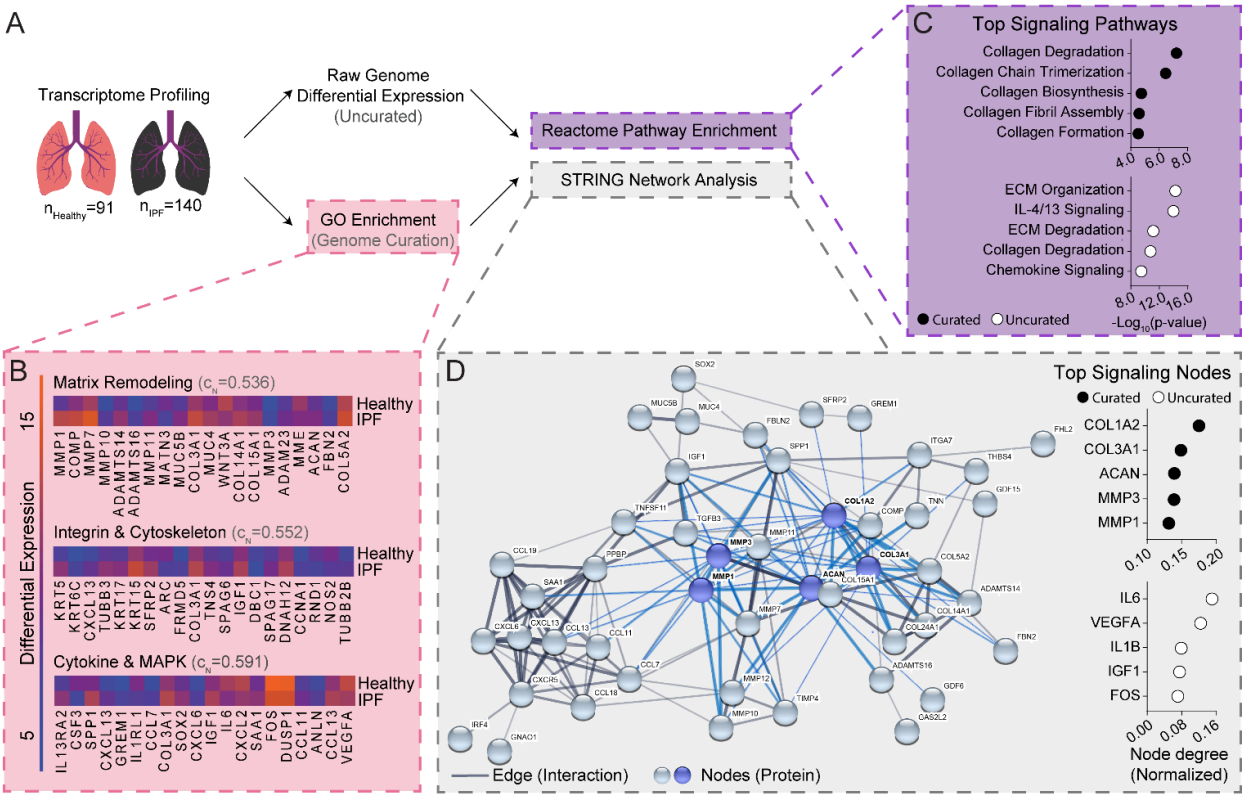

Figure 4.6: Bioinformatics analysis of IPF patient transcriptomes reveals matrix remodeling as a key signaling node in human disease. A) Schematic representation of bioinformatics workflow: whole-genome transcriptomes from 91 healthy and 140 patients with lung fibrosis were fetched from the NCBI GEO. Differential expression analysis was utilized to assemble an uncurated list of the top 1000 differentially expressed genes. GO enrichment of choice biological pathways was utilized to assemble a curated list of genes associated with MF differentiation. Datasets were fed through a prior-knowledge based analysis pipeline to identify enriched signaling pathways (Reactome) and key protein signaling nodes (STRING) within IPF patients. B) Heatmaps of the top 20 differentially expressed genes within specified GO categories which were manually selected for curated analysis. C_N values indicate a high degree of interaction between proteins selected for curated analysis. Colors are based on differential expression values which were not log-normalized. C) Summary of the top 5 significantly enriched pathways in the curated and uncurated gene set. D) Representative STRING diagram depicting protein interactions within the curated dataset, with summary of the top 5 signaling nodes in the uncurated and curated gene set. Blue nodes and edges represent interactions within the top 5 signaling nodes for the curated dataset.

4.5 Discussion

Despite fibrosis widely contributing to mortality worldwide, inadequate understanding of fibrotic disease pathogenesis has limited the development of efficacious therapies (Bochaton Piallat et al., 2016). Pre-clinical studies *in vivo,* while indispensable, often fail to translate to clinical settings as evidenced by the failure of ~90% of drugs identified in animal studies (H. Bart van der Worp, D. W. Howells, E.S. Sena, M.J. Porritt, S. Rewell, V. O'Collins, 2016). Additionally, limitations in current technologies (e.g. the embryonic lethality of many genetic ECM knockouts and the limited resolution/imaging depth of intravital microscopy) have hindered the application of pre-clinical *in vivo* models for the study of cell-ECM interactions which underlie fibrogenesis (Cox & Erler, 2011b). In contrast, existing *in vitro* models utilize patient-derived cells are affordable, scalable, and amenable to microscopy, but often fail to recapitulate the complex 3D matrix structure hallmark to the interstitial tissue regions where fibrotic diseases such as IPF originate. We leveraged electrospinning and bio-orthogonal chemistries to engineer novel pulmonary interstitial matrices that are 3D and possess fibrous architecture with biomimetic ligand presentation. In the presence of a pro-fibrotic soluble factors, these settings reproduce hallmarks of fibrosis at cellular and tissue levels **(Figure 4.2-4.4)**. Examining the influence of physical microenvironmental cues (crosslinking/stiffness and fiber density) on MF differentiation, we find that crosslinking/stiffness has opposing effects on MF differentiation in 2D vs. 3D **(Figure 4.1)**, and that incorporation of a fibrous architecture in 3D is a prerequisite to MF differentiation **(Figure 4.4)**. Furthermore, supported by the importance of protease signaling in IPF **(Figure 4.6)**, we performed proof-of-concept pharmacologic screening within our 3D fibrotic matrices **(Figure 4.5)** and highlighted enhanced biomimicry as compared to traditional 2D drug screening substrates where matrix remodeling appears to be dispensable for MF differentiation.

While tunable synthetic hydrogels have identified mechanosensing pathways critical to MF differentiation in 2D, these observations have yet to be translated to 3D fibrous settings relevant to the interstitial spaces where fibrosis originates. Given that late-stage IPF progresses in the absence of external tissue damage, current dogma implicates fibrotic matrix stiffness as the continual driver of MF differentiation *in vivo* (Balestrini et al., 2012; Castella et al., 2010; Santos & Lagares, 2018). While we cannot disregard this hypothesis, our work elucidates a contrasting MMP-dependent mechanism at play in 3D, whereby a compliant, degradable, and fibrous matrix architecture supports MF differentiation, with matrix contraction and stiffening occurring downstream of α-SMA expression, nearly a week later. Given numerous 2D studies indicating matrix stiffness as a driver of MF differentiation, the finding that a compliant matrix promotes MF differentiation may appear counterintuitive (Balestrini et al., 2012; Castella et al., 2010). However, MF accumulation has been documented prior to tissue stiffening in human disease (Fiore et al., 2018), and a recent phase 2 clinical trial (ClinicalTrials.gov Identifier: NCT01769196) targeting the LOX pathway (the family of enzymes responsible for matrix stiffening *in vivo*) failed to prevent disease progression in IPF patients and was terminated due to lack of efficacy (Raghu et al., 2017). Furthermore, compelling recent work by Fiore et. al. combined immunohistochemistry with high-resolution AFM to characterize human IPF tissue mechanics, and found that regions of active fibrogenesis were highly fibrous but possessed a similar Young's modulus as healthy tissue (Fiore et al., 2018). In concert with our *in vitro* data, these findings suggest that MF differentiation is possible within soft provisional ECM *in vivo*, and that the initiation of fibrogenesis may not be dependent on heightened tissue stiffness, so long as matrix fibers and appropriate soluble cues (e.g. TGF- β1) are present.

Consequently, understanding the source of pro-fibrotic soluble cues *in vivo* is of critical importance when identifying therapeutic targets for IPF. Luminex screening of supernatant from 3D fibrotic matrices revealed 6-fold increases in cytokine secretion during fibrogenesis, the majority of which were potent inflammatory factors (eg. GM-CSF, IL-6, IL-8, VEGF-A) and chemoattractants (eg. CCL2, CCL7, CCL11, CXCL1) **(Figure 4.4E)**. Furthermore, IL-6 and VEGF-A were found to be major signaling nodes in IPF patients **(Figure 4.6D)**. While not typically regarded as an immunomodulatory cell population, these findings suggest MFs may maintain localized inflammation to support continual fibrogenesis. Mitogens such as IL-6 and IL-8 promote endothelial- and epithelial-to-mesenchymal transition, a process that gives rise to matrix-producing MF-like cells in IPF (Piera-Velazquez, Li, & Jimenez, 2011). CCR2 (CCL2, CCL7) and CXCR1 (CXCL1, IL-8) ligation facilitates macrophage chemotaxis, potentially leading to a sustained influx of TGF- β1 producing cells in IPF, and glycoproteins such as GM-CSF inhibit caspase activity in mononuclear cells, potentially preventing apoptotic events required for the resolution of wound repair and return to homeostasis (Ehling et al., 2014; Luzina et al., 2015). Additionally, secretion of nearly all cytokines were increased as a function of fiber density, highlighting a potential feed-forward loop distinct from canonical TGF- β1 signaling. Further model development (e.g. co-culture platforms) will be required to examine these hypotheses and the role of MF-derived cytokines in persistent inflammation and fibrosis.

In addition to documenting the role of fibrotic matrix architecture in 3D fibrogenesis, we demonstrate proof-of-concept pharmacologic screening within our synthetic pulmonary interstitial matrices and highlight their improved relevance to human disease. Prior work *in vitro* has documented profound reductions in MF differentiation after treatment with clinically approved anti-fibrotics (Pirfenidone, Nintedanib), whereas in the clinic, Pirfenidone and Nintedanib impede

disease progression but are far from curative (Asmani et al., 2018; Kurita et al., 2017; Ogura et al., n.d.; Sundarakrishnan et al., 2018). Interestingly, Pirfenidone or Nintedanib had insignificant effects in 2D settings in our hands and only modest effects in 3D **(Figure 4.5)**. One reason for this discrepancy may be the use of supraphysiologic Pirfenidone and Nintedanib concentrations in previous *in vitro* studies, whereas we selected dosages based upon plasma concentrations in IPF patients (Schuett, Ostermann, & Wollin, 2015). Differences in pharmacokinetics, nutrient/growth factor diffusion, and cell metabolism between 2D and 3D tissue constructs likely also play a role. Furthermore, as evidenced by the preventative effect of the protease inhibitor Marimastat in 3D hydrogels but not 2D settings **(Figure 4.5)**, pharmacologics which influence matrix degradation and remodeling are likely to have a minimized effect in 2D settings due to the less dynamic nature of tissue culture plastic and flat hydrogels (Baker et al., 2015). Indeed, Nintedanib and Pirfenidone have been shown to influence protease activity and matrix remodeling *in vivo* (Corbel et al., 2001), and may be mediating their effects within fibrotic matrices through modulation of ECM remodeling. Given the identification of numerous potential anti-fibrotic agents (microRNA, TGF-β1 inhibitors, IL-4, IL-13 neutralizing antibodies, integrin blockers) in pre-clinical models, application of the system described here could elucidate how choice pharmacologics impact MF differentiation and matrix remodeling processes which are difficult to recapitulate in 2D culture. Further development of our interstitial matrices as an arrayed platform, as has been elegantly implemented with collagen matrices (Asmani et al., 2018), is a critical next step to moving this technology towards high-throughput screening applications.

It is important to note that this work has several potential limitations. Our material approach allows for facile control of initial microenvironmental conditions (eg. dimensionality, fiber density, ligand density, elastic modulus) and of note, composites of RGD-bearing nondegradable

fibers and degradable bulk hydrogel decouple degradation induced changes in matrix mechanics and ligand availability. However, we have no experimental control over subsequent dynamic cell-driven remodeling events (eg. MMP-mediated hydrogel softening, fibronectin and collagen deposition, hydrogel contraction/stiffening from resident cells) which likely impact local matrix mechanics, cellular mechanosensing, and MF differentiation. Exciting recent technologies such as 3D TFM and magnetic bead microrheology could enable future examination of how these dynamic changes in cell-scale mechanics potentiate MF differentiation in 3D. Along similar lines, although our study suggests a requirement for initial adhesion to the surrounding matrix, how the dynamics of ligand presentation due to matrix remodeling regulates mechanosensing was not explored here. We present this platform as a reductionist approach to modeling the activation of fibroblasts within the 3D fibrous interstitia associated with fibrosis, a pathology that develops over years *in vivo* and involves multiple cell types. Human pulmonary tissue and fibrotic foci in particular also possess viscoelastic and nonlinear mechanical behaviors (Fiore et al., 2018; Nam, Lee, Brownfield, & Chaudhuri, 2016) which were not explored in our AFM measurements of murine lung or hydrogel composites. Given the important role such mechanical features can play in ECM mechanosensing, incorporating new synthetic material strategies in combination with cell-scale mechanical measurements will be essential to modeling physiologic complexity. Indeed, given that the development of engineered microtissues and lung organoids are still in their infancy, decellularized precision-cut lung slices currently represent the best culture platform to capture the full complexity of the lung microenvironment (Liberati et al., 2010).

In summary, we designed a tunable 3D and fibrous hydrogel model which recapitulates dynamic physical (eg. stiffening, contraction) and biochemical (eg. secretion of fibronectin, collagen, and cytokines) alterations to the microenvironment observed during the progression of

IPF. Implementation of our model allowed us to establish a developing mechanism for MF differentiation in 3D compliant environments, whereby cell spreading upon matrix fibers drives YAP activity, cytokine release, and proteolysis-dependent MF differentiation. Furthermore, we leveraged bioinformatics techniques to explore protease signaling in clinical IPF, and in concert with our therapeutic screening data, establish a strong role for proteases during IPF pathogenesis and in 3D MF differentiation, respectively. Whether protease activity promoted MF differentiation directly through modulation of intracellular signaling, or indirectly through affects on the local matrix environment has yet to be explored in these settings but will be the focus of future efforts. Consequently, these results highlight critical design parameters (3D degradability, matrix architecture) frequently overlooked in established synthetic models of MF differentiation. Future work incorporating macrophages, endothelial cells and epithelial cells may expand current understanding of how developing MF populations influence otherwise homeostatic cells, and how matrix remodeling influences paracrine signaling networks and corresponding drug response. Given the low translation rate of drugs identified in high-throughput screening assays, we show that the application and development of engineered biomimetics, in combination with pre-clinical models, can improve drug discovery and pathophysiological understanding.

4.6 Materials and Methods

4.6.1 Reagents, Synthesis, and Materials

All reagents were purchased from Sigma Aldrich and used as received, unless otherwise stated.

Dextran vinyl sulfone (DexVS)**:** A previously described protocol for vinyl sulfonating polysaccharides was adapted for use with linear high MW dextran (MW 86,000 Da, MP Biomedicals, Santa Ana, CA) (Matera et al., 2019). Briefly, pure divinyl sulfone (12.5 ml, Fisher

Scientific, Hampton, NH) was added to a sodium hydroxide solution (0.1 M, 250 mL) containing dextran (5 g). This reaction was carried out at 1500 RPM for 3.5 minutes, after which the reaction was terminated by adjusting the pH to 5.0 via the addition of hydrochloric acid. A lower functionalization of DexVS was utilized for hydrogels, where the volume of divinyl sulfone reagent was reduced to 3.875 ml. All reaction products were dialyzed for 5 days against Milli-Q ultrapure water, with two water exchanges daily, and then lyophilized for 3 days to obtain the pure product. Functionalization of DexVS was characterized by ^{1}H –NMR spectroscopy in D_2O and was calculated as the ratio of the proton integral (6.91 ppm) and the anomeric proton of the glucopyranosyl ring (5.166 and 4.923 ppm), here a vinylsulfone/dextran repeat unit ratio of 0.376 and 0.156 was determined for electrospinning and hydrogel DexVS polymers, respectively.

For fiber segment fabrication, DexVS was dissolved at 0.6 g ml^{-1} in a 1:1 mixture of Milli-Q ultrapure water and dimethylformamide with 0.015% Irgacure 2959 photoinitiator. Methacrylated rhodamine (0.5 mM; Polysciences, Inc., Warrington, PA) was incorporated into the electrospinning solution to fluorescently visualize fibers under 555 laser. This polymer solution was utilized for electrospinning within an environment-controlled glovebox held at 21 ˚C and 30% relative humidity. Electrospinning was performed at a flow rate of 0.3 ml h^{-1}, gap distance of 5 cm, and voltage of -10.0 kV onto a grounded collecting surface attached to a linear actuator. Fiber layers were collected on glass slabs and primary crosslinked under ultraviolet light (100mW cm^{-2}) and then secondary crosslinked (100 mW cm^{-2}) in a 1mg mL^{-1} Irgacure 2959 solution. After polymerization, fiber segments were resuspended in a known volume of PBS (typically 3 ml). The total volume of fibers was then calculated via a conservation of volume equation: total resulting solution volume = volume of fibers + volume of PBS (3 ml). After calculating total fiber volume,

solutions were re-centrifuged, supernatant was removed, and fiber pellets were resuspended to create a 10 vol% fiber solution, which were then aliquoted and stored at 4^{o} C. To support cell adhesion, 2.0 mM RGD was coupled to vinyl sulfone groups along the DexVS backbone via Michael-type addition chemistry for 30 min, followed by quenching of excess VS groups in a 300 mM cysteine solution for 30 minutes.

For hydrogel formation, DexVS gels were formed via a thiol-ene click reaction at 3.3% w/v (pH 7.4, 37°C, 45 min) with VPMS crosslinker (12.5, 20, 27.5 mM) (GCRDVPMSMRGGDRCG, Genscript, George Town, KY) in the presence of varying amounts of argininylglycylaspartic acid (RGD, CGRGDS, 2.0 mM, Genscript, George Town, KY), heparin-binding peptide (HBP, GCGAFAKLAARLYRKA, 1.0 mM, Genscript, George Town, KY), and fiber segments (0.0-5.0% v/v). For experiments comparing hydrogels of varying ligand type (1 mM HBP vs. 2 mM RGD) cysteine was added to precursor solutions to maintain a final vinyl sulfone concentration of 60 mM. All hydrogel and peptide precursor solutions were made in PBS containing 50 mM HEPES. To create fibrous hydrogels, a defined stock solution (10% v/v) of suspended fibers in PBS/HEPES was mixed into hydrogel precursor solutions prior to gelation. Via controlling the dilution of the fiber suspension, fiber density was readily tuned within the hydrogel at a constant hydrogel weight percentage. For gel contraction experiments, DexVS was polymerized within a 5 mm diameter PDMS gasket to ensure consistent hydrogel area on day 0.

4.6.2 Cell Culture

Normal Human Lung Fibroblasts (NHLFs, University of Michigan Central Biorepository), Normal Human Dermal Fibroblasts (Lonza, Basel, Switzerland), and Normal Human Mammary Fibroblasts (Sciencal, Carlsbad, CA) were cultured in DMEM containing 1%

penicillin/streptomycin, L-glutamine and 10% fetal bovine serum (Atlanta biologics, Flowery Branch, GA). NHLFs derived from 3 separate donors were utilized for experiments. Cells were passaged upon achieving 90% confluency at a 1:4 ratio and used for studies until passage 7. For all hydrogel studies, cells were trypsinized, counted and either encapsulated into or seeded onto 25 µl hydrogels at a density of 1,000,000 cells ml^{-1} of hydrogel, and subsequently cultured at 37°C and 5% CO2 in serum containing medium. For studies comparing 3D hydrogels to tissue culture plastic, the number of cells seeded into 2D conditions was analogous to the total cell number within hydrogel matrices. Media was refreshed the day after encapsulation and every 2 days after. In selected experiments, recombinant human TGF- β1 (5 ng/ml, Peprotech, Rocky Hill, NJ) was supplemented into the media at 5 ng ml^{-1}. For pharmacological studies, Nintedanib (50 nM, Fisher Scientific, Hampton, NH), Pirfenidone (100 µM, Fisher Scientific, Hampton, NH), Marimastat (1.0 µM), dimethyl fumarate (100 nM), were supplemented in serum containing media and refreshed every 2 days.

4.6.3 Microscopy

Cultures were fixed with 4% paraformaldehyde for 30 min at room temperature. To stain the actin cytoskeleton and nuclei, samples were permeabilized in PBS solution containing Triton X-100 (5% v/v), sucrose (10% w/v), and magnesium chloride (0.6% w/v), blocked in 1% BSA, and stained simultaneously with phalloidin and DAPI. For immunostaining, samples were permeabilized, blocked for 8 h in 1% w/v bovine serum albumin, and incubated with mouse monoclonal anti-YAP antibody (1:1000, Santa Cruz SC-101199), mouse monoclonal anti-fibronectin antibody (FN, 1:2000, Sigma #F6140), rabbit monoclonal anti-Ki67 (1:500, Sigma #PIMA514520) or mouse monoclonal anti- α-SMA (1:2000, Sigma #A2547) followed by secondary antibody for 6 h each at room temperature with 3x PBS washes in between. High-

resolution images of YAP, FN and actin morphology were acquired with a 40x objective. Unless otherwise specified, images are presented as maximum intensity projections of 100μm Z-stacks. Hydrogel samples were imaged on a Zeiss LSM 800 laser scanning confocal microscope. SHG imaging of lung tissue was imaged was conducted on a Leica SPX8 laser scanning confocal microscope with an excitation wavelength of 820 nm and a collection window of 400-440 nm. Single cell morphometric analyses (cell spread area) were performed using custom Matlab scripts with sample sizes > 50 cells/group, while YAP, α-SMA, Ki67, FN immunostains were quantified on an image basis with a total of 10 frames of view. Myofibroblasts were denoted as nucleated, F-actin+, α-SMA+ cells. For cell density (# of nuclei) calculations, DAPI-stained cell nuclei were thresholded and counted in six separate 600 x 600 x 200 μm image volumes, allowing us to calculate a total number of cells per mm^3 of gel. Fiber recruitment analysis was conducted via a custom Matlab script; briefly, cell outlines were created via actin masking and total fiber fluorescence was quantified under each actin mask on a per cell basis. A similar analysis method using Matlab was used for cell-cell junction analysis as published previously, with higher area:perimeter ratios and clusters/cell indicative as more pronounced network formation (Davidson, Wang, Zaimi, Jayco, & Baker, 2019).

To determine the elastic modulus of lung tissue and DexVS hydrogels, indentation tests were employed using a Nanosurf FlexBio atomic force microscope (AFM; Nanosurf, Liestal, Switzerland). Samples were indented upon via a 5 μm bead at a depth of 10 μm and an indentation rate of 0.333 μm/s. Resulting force-displacement curves were fit to a spherical Hertz model utilizing AtomicJ. A Poisson's ratio of 0.5 and 0.4 were utilized for hydrogels and lung tissue, respectively.

4.6.4 PCR and ELISA

For all PCR experiments, additional hydrogel replicates were finely minced and degraded in dextranase solution (4 IU/ml, Sigma) for 20 minutes, homogenized in buffer RLT (Qiagen, Venlo, Netherlands), and RNA was isolated according to manufacturer protocols. cDNA was generated from DNAse-free RNA, amplified, and gene expression was normalized to the house-keeping gene, glyceraldehyde 3-phosphate dehydrogenase (GAPDH). Experiments were run with technical triplicates across three individual biological experiments.

To characterize the inflammatory secretome associated with various DexVS-VPMS environments, media was collected from NHLF cultures 3, 5, 7, and 9 days post encapsulation. A Luminex FlexMAP 3D (Luminex Corporation, Austin, TX) systems technology was used to measure 41 cytokines/ chemokines (HCTYMAG-60K-PX41, Milliplex, EMD Millipore Corporation) in the media samples according to manufacturer instructions. Total secretion was reported as the sum of all 41 analytes measured for each respective condition. Cell secreted collagen was measured using the established colorimetric Sircol assay in hydrogels cultured with serum free media in the presence of 25 $\mu g\ ml^{-1}$ ascorbic acid.

4.6.5 Animal Studies

All animal studies were approved by the Animal Care and Use Committee at the University of Michigan. Bleomycin (0.025 U; Sigma) was instilled intratracheally in C57BL6 mice (8 wk of age; The Jackson Laboratory, Bar Harbor, ME, USA) on day 0. Briefly, mice were anesthetized with sodium pentobarbital, the trachea was exposed and entered with a 30-gauge needle under direct visualization, and a single 30-µl injection containing 0.025 U bleomycin (Sigma) diluted in normal saline was injected. Lungs were collected on day 14 for mechanical and histological analysis. For histology samples, lungs were perfused with saline and inflated with 4% paraformaldehyde, sectioned, and stained with Picosirius Red. For mechanical

characterization via AFM, lungs were perfused with saline, infused with OCT compound (Fisher), and flash frozen in a slurry of dry ice and ethanol. Sections were mechanically tested via AFM nanoindentation immediately upon thawing.

4.6.6 Bioinformatics

The NCBI GEO database was consulted (dataset GSE47460 (GP14550)) to fetch gene expression data from 91 healthy patients and 140 patients with IPF; patients with COPD and non-idiopathic fibrotic lung diseases were excluded from the analysis (Barrett et al., 2013). GEO2R (http://www.ncbi.nlm.nih.gov/geo/geo2r/) software was utilized for GO term enrichment, with keywords extracellular matrix, MMP, integrin, cytoskeleton, cytokine, chemokine, and MAPK used as search terms for dataset curation (Barrett et al., 2013). Noncurated datasets were composed of the top 1000 differentially expressed genes between healthy and ILD conditions. Differential expression was calculated based on subtracting normalized expression values between diseased and healthy patients. All genes were normalized prior to analysis with GEO2R via a pairwise cyclic losses approach. For pathway and protein-protein enrichment analyses, a curated pathway database (Reactome (Jassal et al., 2019)) and Search Tool for Retrieval of Interacting Genes/Proteins (STRING (Szklarczyk et al., 2019)) methodology were consulted, respectively. For STRING analyses, upregulated genes within the druggable genome were focused upon.

4.6.7 Statistical Analysis

Statistical significance was determined by one-way analysis of variance (ANOVA) or Student's t-test where appropriate, with significance indicated by $p<0.05$. All data are presented as mean ± standard deviation.

4.7 Supplementary Figures

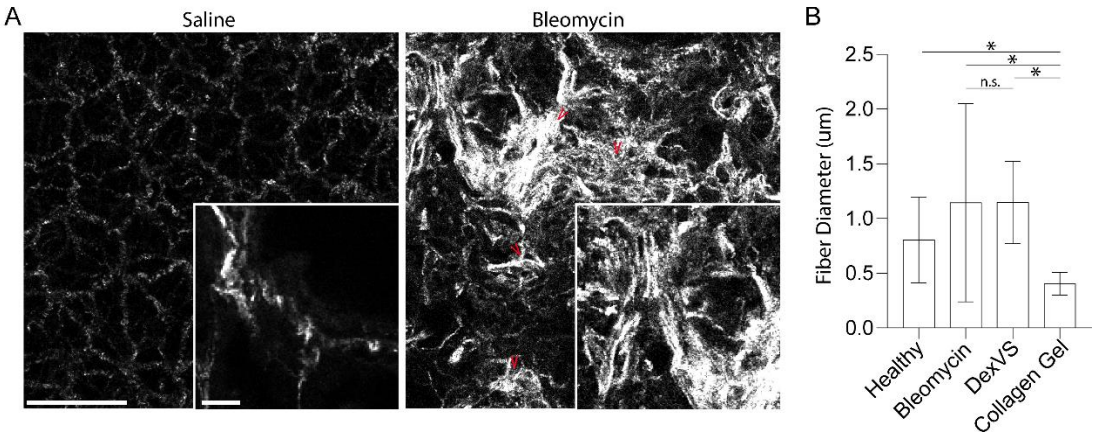

Supplementary Figure 4.1: Collagen fiber architecture within saline and bleomycin treated lungs. A) Second harmonic generation microscopy images of collagen fibers within saline and bleomycin treated mouse lung tissue at day 14 (scale bar: 75 µm); insets: higher magnification images depicting regions containing collagen fiber bundles in bleomycin treated lung tissue (scale bar: 5 µm). B) Quantification of fiber diameter (n>20 fibers) within mouse lung compared to synthetic DexVS fibers and collagen fibers within 3 mg/ml reconstituted type I collagen matrices. All data presented are means ± standard deviations; asterisk denotes significance with $p < 0.05$ determined by one-way analysis of variance; n.s. denotes non-significant comparison.

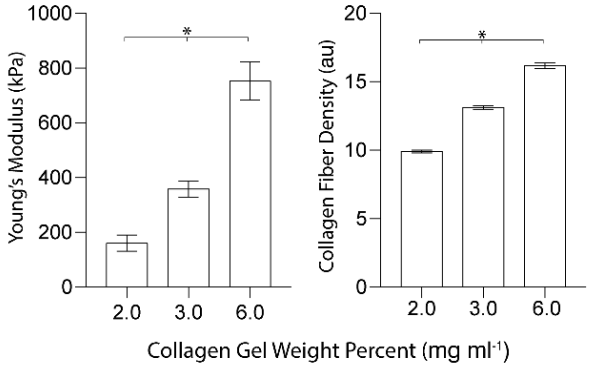

Supplementary Figure 4.2: Relationship between collagen gel mechanical and structural properties. Quantification of type I collagen gel Young's modulus and fiber density as a function of gel weight percentage (n=10 measurements/group). All data presented are means ± standard deviations; asterisk denotes significance with $p < 0.05$ determined by one-way analysis of variance.

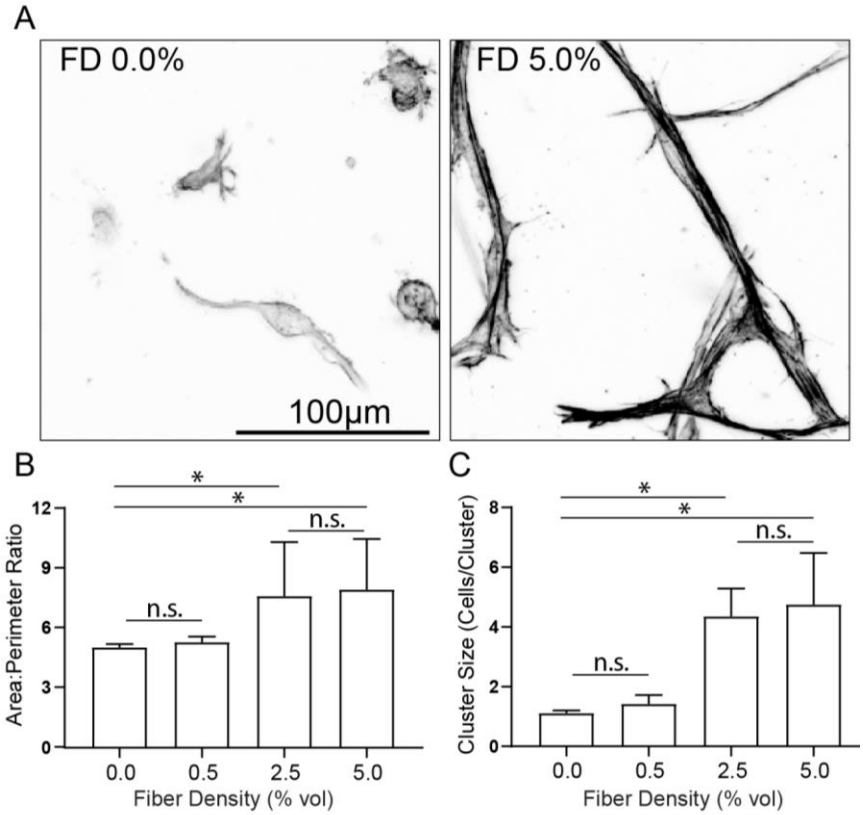

Supplementary Figure 4.3: Effect of fiber density on lung fibroblast actin cytoskeleton and multicellular network formation. A) Representative high-magnification images of NHLF F-actin within nonfibrous control (FD 0.0%) and fibrous (FD 5.0%) hydrogels after 3 days of culture (scale bar: 100 μm). B) Quantification of fibroblast network area:perimeter ratio and C) number of fibroblasts per cell cluster (n=4 samples/group with n=10 frames of view quantified and n>25 cells/frame of view) after 3 days of culture. Note: higher area:perimeter ratio and cluster size indicate increased cell-cell connectivity in 3D (Davidson et al., 2019). All data presented are means ± standard deviations; asterisk denotes significance with $p < 0.05$ determined by one-way analysis of variance; n.s denotes non-significant comparison.

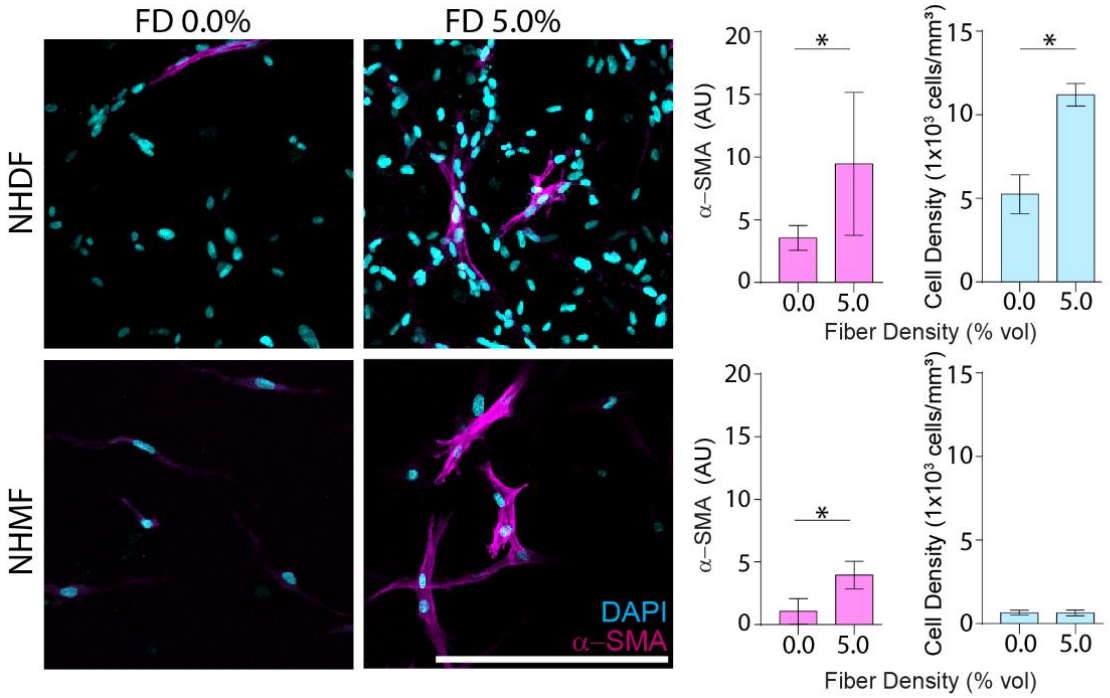

Supplementary Figure 4.4: Fiber density effects on dermal and mammary fibroblasts. Representative images of normal human dermal fibroblasts (NHDF) and normal human mammary fibroblasts (NHMF) within nonfibrous control (FD 0.0%) and fibrous hydrogels (FD 5.0%) after 9 days of culture (scale bar: 200 μm), with quantification of α-SMA and cell density (n=4 samples/group with n=10 frames of view quantified and n>25 cells/frame of view. All data presented are means ± standard deviations; asterisk denotes significance with $p < 0.05$ determined by Student's t-test.

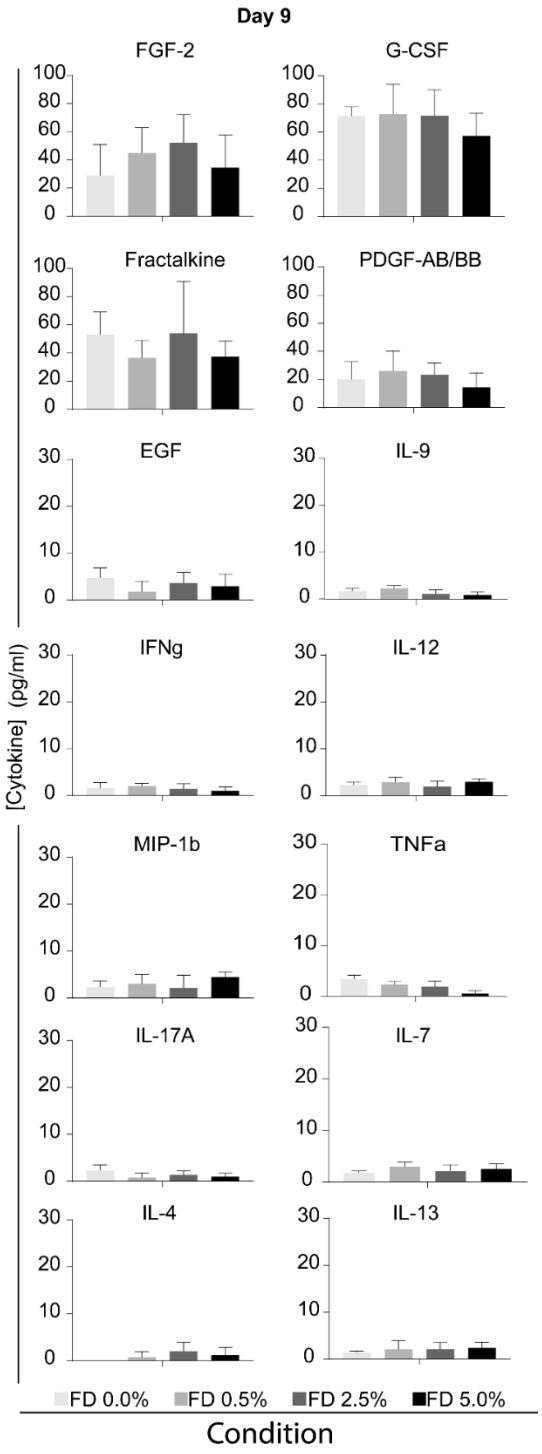

Supplementary Figure 4.5: Full panel of all measurable cytokines secreted by 3D cultured fibroblasts. Luminex quantification of detectable cytokines and growth factors in day 9 NHLF culture media supernatant over a range of fiber density (n=4 samples/group). Factors which significantly changed as a function of fiber density can be seen in **Figure** 4. All data presented are means ± standard deviations; no significant differences were determined with $p < 0.05$ by one-way analysis of variance.

Chapter 5: The Contribution of Rho GTPases During 3D MF Differentiation

5.1 Authors

Daniel L. Matera, Alexander T Lee, Harrison L Hiraki, Brendon M Baker

5.2 Abstract

Connective tissue repair and mechanosensing are tightly entwined *in vivo* and occur within a complex three-dimensional (3D), fibrous extracellular matrix. Typically driven by activated fibroblasts, wound repair involves well-defined steps of cell spreading, migration, proliferation, and fibrous matrix deposition. While the role of Rho GTPases in regulating these processes has been explored extensively in two-dimensional cell culture models, much less in known about their role in more physiologic, 3D environments. Here we utilized a 3D, fibrous synthetic hydrogel platform to model interstitial tissues and examine how Rho GTPases in conjunction with fibrous tissue microstructure modulate wound repair processes of lung fibroblasts. Modulating fiber density within protease sensitive hydrogels confirmed prior findings that increases in fiber density promotes fibroblast spreading and proliferation. This corresponded with increased migration and hydrogel contraction by resident fibroblasts. During fibroblast spreading, Rac1 and RhoA GTPase activity proved crucial for fiber-mediated cell

spreading and contact guidance, while Cdc42 was dispensable. In contrast, interplay between RhoA, Rac1, and Cdc42 contributed to fiber-mediated myofibroblast differentiation and matrix contraction over longer time scales. Our observations may provide insight into tissue repair processes *in vivo* and highlight useful design criteria for material-guided wound repair strategies.

5.3 Introduction

A 3D network of interpenetrating micron-scale fibers embedded within a finer meshwork of gel-like proteoglycans, the extracellular matrix (ECM) provides numerous structural and biochemical cues to drive cell and tissue function (Frantz, Stewart, & Weaver, 2010; Vogel, 2018). ECM homeostasis is maintained by fibroblasts, normally quiescent tissue cells resident to the interstitial matrix of all organs in the body (Bochaton Piallat et al., 2016). In response to external tissue damage, fibroblasts activate during the inflammatory phase of wound repair and migrate to the wound site, ultimately undergoing expansion and differentiation into myofibroblasts (MFs); these contractile cells mediate interstitial ECM deposition and reorganization during the latter phases of wound repair (Bochaton Piallat et al., 2016; I. A. Darby & Hewitson, 2007; Kendall & Feghali-Bostwick, 2014; Wells & Maher, 2017). Insufficient recruitment and differentiation of MFs can hinder wound healing, and conversely, MF hyperactivity and resistance to apoptosis or dedifferentiation contribute to numerous pathologies such as organ fibrosis and cancer (Kendall & Feghali-Bostwick, 2014; Wynn, 2008). Consequently, understanding how interactions with the ECM influences fibroblast behavior is critical for both understanding pathophysiology and the creation of therapies that promote healthy wound repair.

While seminal work studying the wound healing response *in vivo* has been critical for characterizing the distinct phases, cellular players, and associated cytokines that mediate tissue repair (I. Darby, Skalli, & Gabbiani, 1990; G. Gabbiani, Chaponnier, & Huttner, 1978; Ortega, Ittmann, Tsang, Ehrlich, & Basilico, 1998), limitations in intravital imaging and the lethality of genetic knockout of ECM proteins have hindered the study of fibroblast-ECM interactions at the cellular scale *in vivo* (Cox & Erler, 2011b). Consequently, *in vitro* studies of cells plated on 2D culture substrates have been critical for investigating fibroblast biology and in particular, matrix mechanosensing during the fibroblast wound healing response. Multiple culture settings have noted the importance of cell adhesion and actomyosin force generation in the fibroblast-driven wound healing response (Balestrini et al., 2012; Castella et al., 2010; Tomasek, Gabbiani, Hinz, Chaponnier, & Brown, 2002). These key fibroblast functions are controlled by the reorganization and force dynamics of the actomyosin cytoskeleton, dictated primarily by the activity of the Rho GTPases Rac1, Cdc42, and RhoA and their associated regulators (Huang et al., 2012; Ridley, 2001; Tapon & Hall, 1997). Simple 2D models such as scratch wound assays have elucidated a requirement for RhoA and Rac1 in force generation and lamellipodia formation during cell migration, respectively, and the role of Cdc42 in proliferation and generating filopodia for cell-ECM sensing (Liang, Park, & Guan, 2007; S. Liu, Kapoor, & Leask, 2009; Nobes, 2000; Ridley, 2001; Tapon & Hall, 1997; Wirtz, 2004). Given that these simple 2D models fail to recapitulate the 3D and fibrous nature of *in vivo* ECM, the use of reconstituted natural materials such as fibrin and type I collagen gels have also proved informative. Studies of fibroblasts embedded within these hydrogels further implicate Rho GTPases in wound healing processes, namely the requirement of RhoA for cell spreading and force generation required for macroscale gel contraction (Boris Hinz, Mcculloch, & Coelho, 2019; Yee, Melton, & Tran, 2001). Importantly,

while these natural hydrogels possess fibrous architecture, they lack a proteoglycan gel-like component, are prone to rapid degradation and resorption *in vivo* thus limiting their use for wound repair, and have biophysical properties that are difficult to modulate independently (e.g. increasing ECM protein concentration concomitantly increases fiber density, stiffness, and ligand density, but decreases pore size and degradability) (Ghajar et al., 2008; L. Li et al., 2017; Riching et al., 2015). These material limitations have hindered the use of natural materials for mechanistic study of cell-ECM interaction, or for regenerative therapies which require stability across long time scales through tailored degradation rates (Gunatillake, Adhikari, & Gadegaard, 2003; Nakagawa et al., 1989).

In contrast to naturally derived materials, synthetic hydrogels with tunable physical and biochemical properties have emerged as a powerful tool for dissecting the impact of individual matrix properties on cell function. For example, study of fibroblasts seeded on non-degradable 2D hydrogels varying in stiffness has supported a requisite threshold of matrix stiffness and resulting RhoA/MRTF-A activity for MF differentiation (Balestrini et al., 2012; Castella et al., 2010). Unfortunately, these synthetic polymeric networks typically lack micro-scale fibrous architecture and unlike native tissue ECM, possess a homogenous distribution of adhesive ligands and nanoporous topography (Pathak & Kumar, 2011; Russell & Carta, 2005). Such distinctions raise concerns over whether results from these models translate to more complex *in vivo* tissue environments. Separately, electrospinning is an established method for fabricating fibrous scaffolds that have been widely investigated for wound repair applications, potentially indicating a positive influence of fibrous microstructure in wound healing (Leong, Wu, Ng, & Tan, 2016; X. Wang, Ding, & Li, 2013). Given that electrospun scaffolds are typically thin mats which lack a proteoglycan gel-like component and have subcellular pore sizes that limit cell

infiltration (Baker et al., 2008), we recently integrated electrospinning with cell-degradable hydrogel chemistries to generate a multi-component model of the extracellular matrix (Matera et al., 2019). These fiber-hydrogel composites incorporate a tunable gel-like proteoglycan component and adhesive ligand-presenting microfibers, mimicking the two-phase structure of native ECM. Using this system, we recently showed that increased fiber density drives MF differentiation and fibrosis-associated signaling *in vitro* (Matera et al., 2020). Given the parallels between wound healing and fibrosis, and furthermore the deposition of fibrous collagen occurring in both contexts (Barker & Engler, 2017; Fiore et al., 2018), we hypothesized that fiber-reinforced hydrogel composites would promote fibroblast functions associated with key phases of the wound healing process.

Here, we focused on the three primary phases of wound repair following hemostasis (ie. inflammation, proliferation and remodeling) with the goal of understanding how the interplay between Rho GTPase activity and a fibrous ECM cue facilitate the tissue repair functions of fibroblasts. In line with our previous data, the presence of cell-adhesive fibers induces earlier activation (spreading, stress fiber generation, migration and proliferation) of fibroblasts in 3D settings, and promotes MF differentiation (□-smooth muscle actin (α-SMA) expression and heightened contractility) at later timepoints. Via pharmacologic perturbation of RhoA, Rac1, and Cdc42, we then explored the intersection of Rho GTPase activity and cell-matrix fiber interactions that guide fibroblast spreading, migration, and differentiation toward MFs. Initial protrusion formation along fibers was found to be Rac1 dependent in 3D, whereas maturation of these protrusions into stress fiber bearing structures required ROCK/RhoA. In contrast to prior results from 2D studies, we found that pharmacologic inhibition of Rac1 and Cdc42 had minimal effects on inhibiting the 3D migration of fibroblasts, whereas RhoA was essential. We also

showed that inhibition of one GTPase alone was not sufficient to prevent MF differentiation at later timepoints. Our studies suggest a strong interplay between RhoA, Rac, and Cdc42 in 3D fibrous environments, and suggests that strategies to improve wound healing (or conversely prevent aberrant fibrosis) will likely need to simultaneously target multiple Rho GTPases in a cell function dependent manner.

5.4 Results

Given the 3D nature of many native tissues, the ubiquitous presence of ECM fibers *in vivo*, and the importance of fibronectin and collagen secretion during the production of provisional matrix (Barker & Engler, 2017), here we utilized a previously established strategy to generate a 3D fibrous hydrogel model of the wound environment. To generate cell-adhesive, micron-scale diameter ECM-like fibers, we functionalized dextran, a protein-resistant hydrophilic polysaccharide amenable to electrospinning, with pendant vinyl sulfone groups that support photo-crosslinking and peptide functionalization through UV-initiated radical polymerization and Michael-type addition, respectively. We then electrospun dextran vinyl sulfone (DexVS) on a cylindrical collection mandrel **(Figure 5.1A)** to optimize collection efficiency of deposited 1μm diameter DexVS fibers. These fibers were then UV photo-crosslinked, collected in suspension, and functionalized with the adhesive ligand RGD (CGRGDS), an integrin ligand that supports cell spreading, a process critical to wound healing (Bellis, 2011; Smithmyer, Sawicki, & Kloxin, 2014; Walraven & Hinz, 2018). After RGD functionalization, DexVS fibers were encapsulated within a DexVS hydrogel crosslinked with thiolated matrix-metalloproteinase (MMP) cleavable peptides (GCVPMS↓MRGGCG), yielding a two-phase composite of cell-adhesive, non-degradable matrix fibers ensconced within

protease-degradable hydrogel. Given the importance of matrix deposition during wound repair, we also functionalized the hydrogel component with a heparin-binding peptide (HBP, CGFAKLAARLYRKAG) to sequester fibroblast-secreted proteins that interact with heparan sulfate proteoglycans (Olczyk, Mencner, & Komosinska-Vassev, 2015).

This material platform allows for orthogonal modulation of fiber density (0-2.5% volume fibers) without altering the elastic modulus or degradation kinetics of the surrounding bulk hydrogel **(Figure 5.1B)**. Due to the non-degradable nature of DexVS fibers, this system also maintains constant RGD density despite surrounding hydrogel degradation, making this platform advantageous for studying fibroblast-ECM interactions during the wound healing process. Encapsulating primary human fibroblasts in DexVS hydrogels containing a fiber density reminiscent of late provisional matrix stimulated a cell spreading response after 24 hours of culture, whereas fibroblasts within control nonfibrous hydrogels remained largely unspread over the same period. These results are in line with findings from our prior work showing that fibrous microstructure expedites cell spreading and adhesion-mediated signaling required for fibroblast activation (Matera et al., 2020). Given the ubiquity of fibrous interstitial ECM and the well-documented role of matrix fiber remodeling in the later phases of wound repair (Barker & Engler, 2017; Yasui, Tanaka, Hase, Fukushima, & Araki, 2014), we compared cell behavior in nonfibrous DexVS hydrogels vs. fibrous composites, with the goal of understanding how Rho GTPase activity in fibroblasts mediates cell interactions with matrix fibers and resultant fibroblast function.

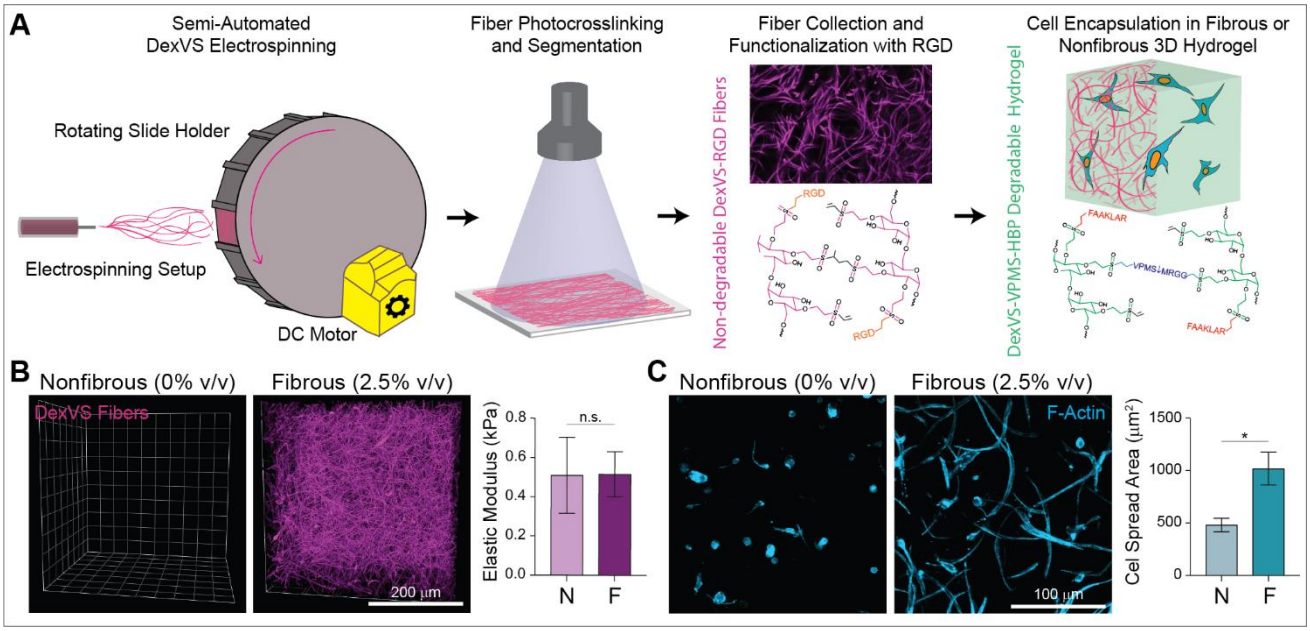

Figure 5.1: Synthetic fibrous hydrogel composites to model the late provisional matrix of wound healing. A) Fabrication schematic for generating fiber-reinforced DexVS hydrogels. B) Representative confocal Z-stack renderings of a nonfibrous (N, 0.0% volume) and high fiber density hydrogel (F, 2.5% volume), with rhodamine-tagged fibers in magenta (scale bar: 200 μm). Young's modulus determined by AFM nanoindentation of control and fibrous DexVS hydrogels (n=4 samples/group, n=5 indentations/sample). C) Representative images of fibroblast F-actin (cyan) within control and fibrous DexVS hydrogels 24 hours after encapsulation, with quantification of projected cell spread area (n=4 samples/group, n=10 fields of view/group, n>25 cells/field of view; scale bars: 100 μm). All data presented are means ± standard deviations; asterisk denotes significance with $p < 0.05$ determined by a Student's t-test.

In response to inflammatory cues arising from tissue damage, one of the earliest stages of fibroblast activation *in vivo* is altered cell morphology and the generation of F-Actin-rich stress fibers (I. Darby et al., 1990; B. Hinz, 2016; Vyalov, Gabbiani, & Kapanci, 1993). Given that fibroblast spreading has been shown to be a prerequisite to fibroblast activation *in vitro* (O'Connor & Gomez, 2013), we first investigated how the presence of matrix fibers modulates normal human lung fibroblast morphology through high-resolution confocal microscopy. In line with our prior results, fibers induced rapid spreading over 24 hours, primarily through contact guidance of nascent cellular protrusions (thin finger-like structures that ultimately develop into F-actin rich extensions) along nearby fibers (**Figure 5.2A**, white arrows). Fiber-mediated

spreading led to increased cellular spread areas as quantified by F-actin staining **(Figure 5.2B)**, and a spindle-like cytoskeletal morphology with high aspect ratios **(Figure 5.2D)** frequently driven by two dominant actin-rich protrusions **(Figure 5.2A)**. In contrast, fibroblasts in control gels possessed high levels of cortical actin and small, randomly oriented protrusions which were fewer in number, resulting in lower spread areas and cellular aspect ratios **(Figure 5.2A-D)**.

To explore which Rho family GTPases are required for cell interactions with matrix fibers and ensuing changes in cell morphology, we treated fibroblasts embedded in nonfibrous and fibrous DexVS hydrogels to a panel of pharmacologic modulators for 24 hours: Y-27632 to reduce the activity of Rho-associated protein kinase (ROCK), the primary downstream effector of RhoA; NSC-23766 to reduce Rac1 activity; ML141 to reduce Cdc42 activity; and lysophosphatidic acid (LPA), a RhoA agonist. Pharmacologic concentrations were validated via screening on 2D tissue culture plastic over ranges known to impact cellular morphology **(Supplemental Figure 5.1A)**. Reduction of ROCK activity reduced fiber-induced increases in total cellular spread area and aspect ratio **(Figure 5.2B,C)** although interestingly, we noted an increase in the number of protrusions **(Figure 5.2A arrows, Figure 5.2D)**, suggesting that ROCK activity is not required for the initiation of protrusions and their extension along matrix fibers. Diminished spreading despite greater number of protrusions, suggests that ROCK activity may be required for maturing nascent protrusions through actin polymerization and eventual actin stress fiber formation. In contrast, reduction of Rac1 activity via NSC-23766 treatment inhibited fiber-mediated cell spreading through a distinct mechanism. NSC-23766 treatment abrogated increases in protrusion formation due to the presence of fibers **(Figure 5.2A, D)**, leading to decreased cell spreading, lower aspect ratios, and cell morphologies akin to cells within nonfibrous hydrogels. ML141 and LPA treatment to reduce Cdc42 activity and activate

RhoA, respectively, did not have detectable effects on cell spread area, aspect ratio, or protrusion formation. These results suggest that contact guidance and protrusion formation are not Cdc42 dependent in 3D for human fibroblasts, in contrast to in 2D culture where we detected fewer protrusions in ML141 treated conditions. Furthermore, the insignificant effects of LPA treatment in fibrous conditions suggests that while RhoA/ROCK activity is required for fiber-induced maturation of protrusions and subsequent spreading in 3D, levels of RhoA activity are not limiting in these settings.

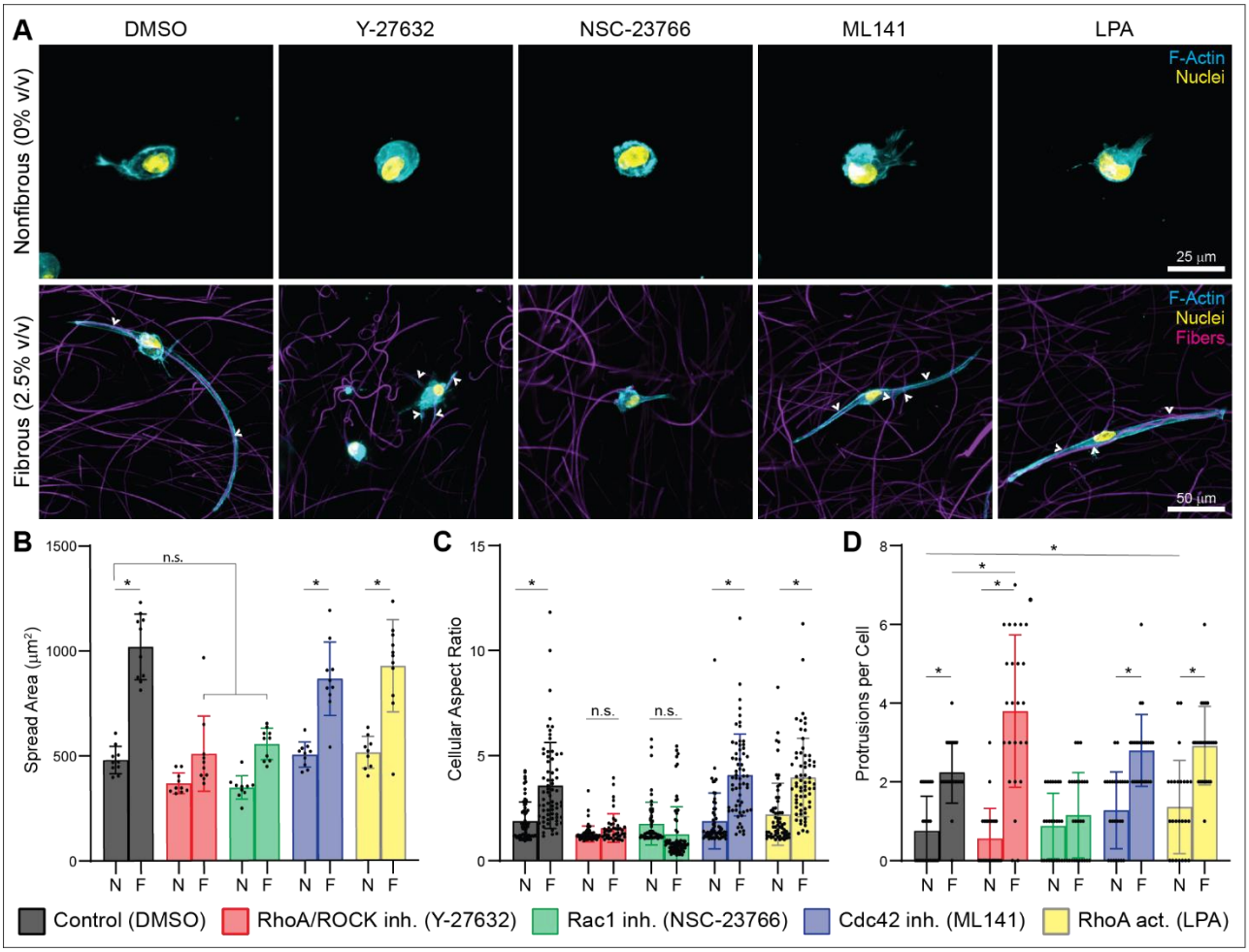

Figure 5.2: Fiber-mediated cell spreading as a function of pharmacologic modulation of Rho GTPases. A) High-resolution images of fibroblasts in nonfibrous (N, 0.0% v/v) and fibrous (F, 2.5% v/v) DexVS hydrogels after 24 hours of culture in the presence of denoted pharmacologic modulators or DMSO (F-actin (cyan), nuclei (yellow), DexVS fibers (magenta); scale bars: 50 µm). White arrows denote arrows of contact guidance along DexVS fibers. Corresponding image quantification of projected A) F-actin cell spread area, B) cell aspect ratio,

and C) total number of protrusions per cell (n=4 samples/group; for aspect ratio and protrusion quantification, n>25 cells/group; for spread area n>10 fields of view/group and n>25 cells/field of view). Protrusions were defined as F-actin rich puncta greater than 5 μm in length. All data presented are means ± standard deviations; asterisk denotes significance with $p < 0.05$ determined by a two-way analysis of variance.

While cell adhesion, spreading, and underlying cytoskeletal dynamics is often thought to be the initial step for fibroblast activation in response to inflammation and tissue damage, subsequent cell migration and infiltration into the wound bed is critical for wound healing and may also contribute to tissue fibrosis in pathologic contexts (Tschumperlin, 2013). To explore how matrix fibers affect fibroblast migration and to determine which Rho GTPases are critical for this process in 3D, we established a migration assay whereby spheroidal fibroblast aggregates (Ø = 300μm) were encapsulated in control and fibrous hydrogels, stimulated with serum for 24 hours, and exposed to pharmacologic modulators for the next 4 days prior to analysis. In control gels without pharmacologic treatment, we observed nearly a three-fold increase in the total number of migratory invasion events (defined as single or multicellular fibroblast strands infiltrating the hydrogel) in fibrous conditions compared to nonfibrous hydrogels **(Figure 5.3A,B)**, supporting numerous observations that fibrous contact guidance cues support cell polarization and subsequent migration in 3D hydrogel environments (Provenzano, Eliceiri, Inman, & Keely, 2010; Sukmana & Vermette, 2010; Yamada & Sixt, 2019). Corresponding to this, we also observed an increase in the total invasion area (determined from total F-actin area outside of the initial cell aggregate, **Figure 5.3C**) and average migration distance (**Figure 5.3D)** in fibrous conditions, suggesting that fibrous matrix cues also supported more extensive migration in actively motile cells.

Treatment with Y-27632 led to increases in invasion events across all hydrogel conditions **(Figure 5.3A,B)**, supporting our earlier observation that protrusion formation does not appear to be ROCK dependent **(Figure 5.2)**. However, it should be noted that while an

increased number of actin-rich protrusions extended into the surrounding hydrogel, cells were unable to migrate away from the aggregate periphery **(Figure 5.3C,D)**, suggesting that ROCK-dependent contractile forces are required for migration in 3D following protrusion formation. Supporting this hypothesis, LPA treatment to activate RhoA/ROCK signaling increased total migration distances in nonfibrous hydrogels and migration areas in fibrous composites, but did not influence the total number of invasion events. While inhibition of Rac1 via NSC-23766 treatment appeared to have limited effects on cell migration in nonfibrous gels, a reduced the number of migratory events, invasion area, and invasion distance were observed in fibrous gels **(Figure 5.3A-D)**. Given that Rac1 inhibition also blocked fiber-guided protrusions during cell spreading **(Figure 5.2)**, these results further suggest that Rac1 is a key player during cell-fiber contact guidance and initial protrusion formation. ML141 treatment conversely led to increased migration areas and distances in all conditions, and also increased the total number of migratory events in nonfibrous conditions. Interestingly, Cdc42 has well-known roles in filipodia generation and sensing processes that impact 2D migration. Discordant findings between 2D models and our 3D system may be due to the interplay between Cdc42 and matrix metalloproteinase (MMP) activity (Deroanne et al., 2005), a link that would be inconsequential in 2D given that matrix degradation is not required for migration in such contexts (Yamada & Sixt, 2019). Taken together, these results suggest both ROCK and Rac1 are required for migration in 3D, where Rac1 aids in initial protrusion formation after which ROCK activity is required for the generation of actomyosin-mediated forces and subsequent translocation of the cell body.

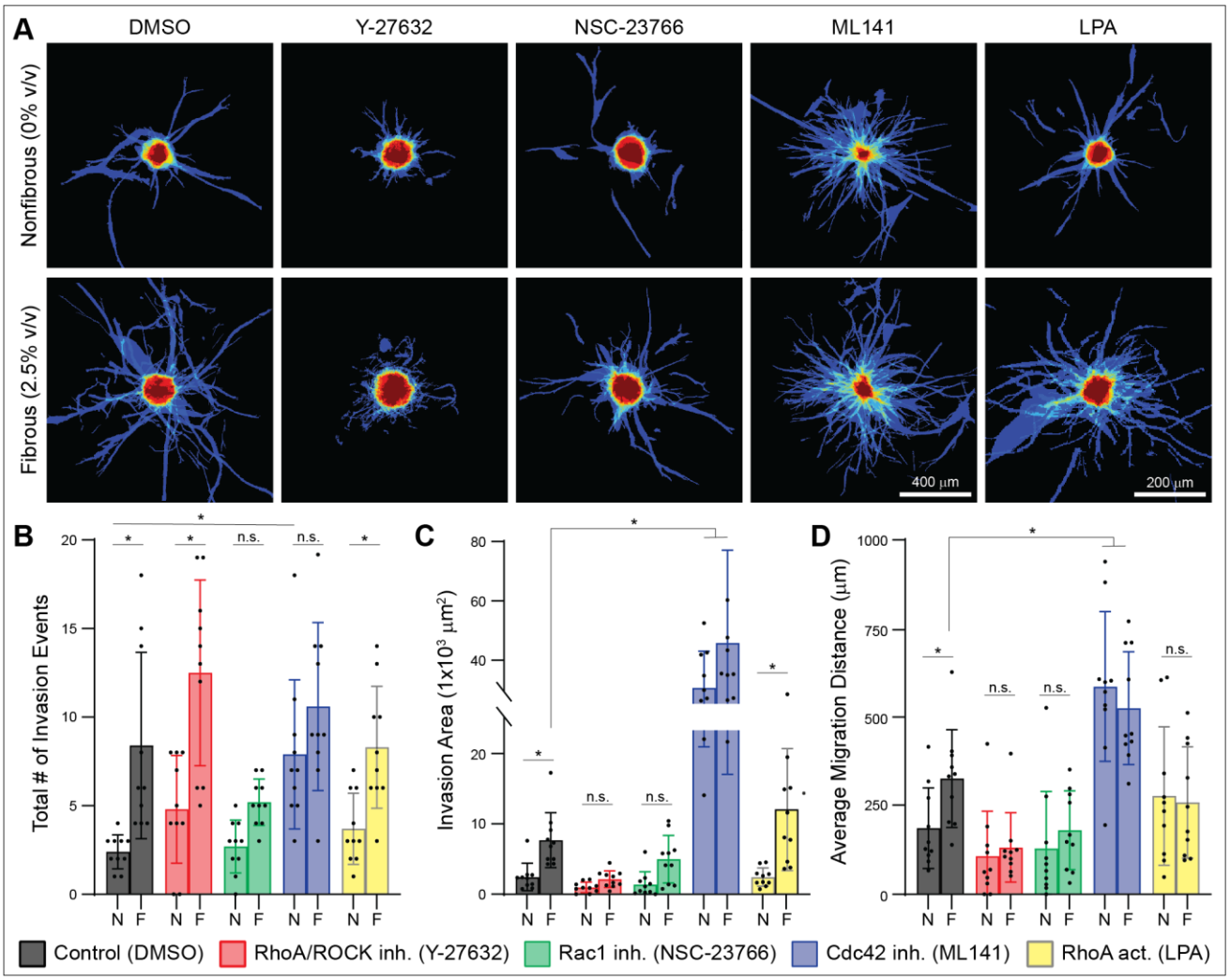

Figure 5.3: Fiber-mediated cell migration as a function of pharmacologic modulation of Rho GTPases. A) Heat map overlays created by an aggregate sum of binarized F-actin images of migrating fibroblast aggregates, after exposure to denoted pharmacologic modulators or DMSO vehicle control for 4 days (n = 10 spheroids/overlay). Red regions indicate regions of greater similarity between replicates, typically denoting the body of the fibroblast aggregate where migration originated from (scale bars: 200 μm for DMSO, Y-27632, NSC-23766, and LPA treated conditions or 400 μm in ML141 treated conditions). Corresponding image quantification of the B) total number of migration events, C) invasion area, and D) migration distance (n>10 aggregates analyzed/group). Migration events were defined as single or collective groups of cells migrating out of the aggregate body. Invasion area was calculated as the total area of F-actin outside of the encapsulated fibroblast aggregate (seen in red in heat map overlays). Migration distance was calculated as the distance from the centroid of each migrating cell or multicellular cluster to the center of the aggregate body. All data presented are means ± standard deviations; asterisk denotes significance with $p < 0.05$ determined by a two-way analysis of variance.

While fibroblasts migrate into provisional matrix soon after injury, the ensuing proliferative phase of wound healing requires proliferation of recruited fibroblasts to create a hypercellular repair tissue reinforced by cell-cell junctions (Singer & Clark, 1999; Tschumperlin, 2013). Through cadherins, these multicellular networks function to drive the coordination of cell-generated tensile forces across long distances in the wound bed to mediate tissue contraction(Follonier, Schaub, Meister, & Hinz, 2008b; Boris Hinz & Gabbiani, 2003; Pittet, Lee, Kulik, Meister, & Hinz, 2008). Previous data from our lab suggests that fibroblast assembly into multicellular networks precedes myofibroblast (MF) differentiation and resulting matrix contraction, all of which were enhanced in the presence of matrix fibers (Matera et al., 2020). Indeed, given that multicellular network formation likely occurs through iterative rounds of protrusive activity, cell spreading, and proliferation, we hypothesized that Rho GTPases underlie the transition from solely cell-ECM adhesion to a mixture of cell-ECM and cell-cell adhesion. Consequently, we sparsely encapsulated single fibroblasts within nonfibrous control and fibrous DexVS hydrogels to explore how RhoA/ROCK, Rac1, and Cdc42 activity affect fibroblast proliferation and multicellular network formation over 5 days of culture. Supporting our prior data (Matera et al., 2020), the incorporation of fibers promoted proliferation **(Figure 5.4A, D)** and network formation, as quantified by a nearly three-fold increase in network area and area:perimeter (A/P) ratio **(Figure 5.54A-C)**, a metric commonly used for vasculogenesis assays where a higher ratio denotes a more interconnected multicellular structure (Califano & Reinhart-King, 2008; Davidson et al., 2019) .

ROCK and Rac1 inhibition markedly reduced fiber-mediated proliferation and network formation **(Figure 5.4)**, although potentially via different mechanisms. Fibroblasts treated with Y-27632 appeared to form more protrusions as observed in early cell spreading studies, leading

to networks with an excess of branch points but less robust junctional assembly between neighboring cells overall **(Supplementary Figure 5.1C)**. In contrast, fibroblasts treated with NSC-27366 appeared to extend unidirectionally along fibers, but the lack of proliferation led to infrequent cell-cell contact and overall limited network formation. Furthermore, in instances where cell-cell contact occurred in NSC-27366 treated fibrous conditions, junctional reinforcement appeared limited as evidenced by thinner F-actin connections between cells **(Supplementary Figure 5.1C)**. However, given the reduced rates of cell proliferation across ROCK and Rac1 inhibited conditions and the importance of proliferation for multicellular network formation, it is difficult to speculate whether diminished cell density and/or fiber-dependent spreading and cell migration are behind the reduction in multicellular assembly.

In nonfibrous conditions, treatment with Y-27632 and NSC-23766 both abrogated cell spreading and reduced total network area **(Figure 5.4)**, suggesting that ROCK and Rac1 activity are also critical for cell spreading in nonfibrous hydrogel environments where guidance cues are lacking. In contrast, treatment with ML141 increased proliferation **(Figure 5.4D)** and network area in nonfibrous control hydrogels, suggesting that Cdc42 activity may actually have an inhibitory role on cell spreading in nonfibrous DexVS hydrogels. Interestingly, Cdc42 activity was dispensable for network formation in fibrous hydrogels, paralleling observations of initial cell spreading at day 1. In sum, these results support prior data **(Figure 5.2)** suggesting that an interplay between Rac1 (required for cell-fiber contact guidance and cell-cell junction formation) and ROCK (required for the development of nascent protrusions into larger spindle structures, contractility, and effective migration) are both critical for fibroblast activation processes in 3D.

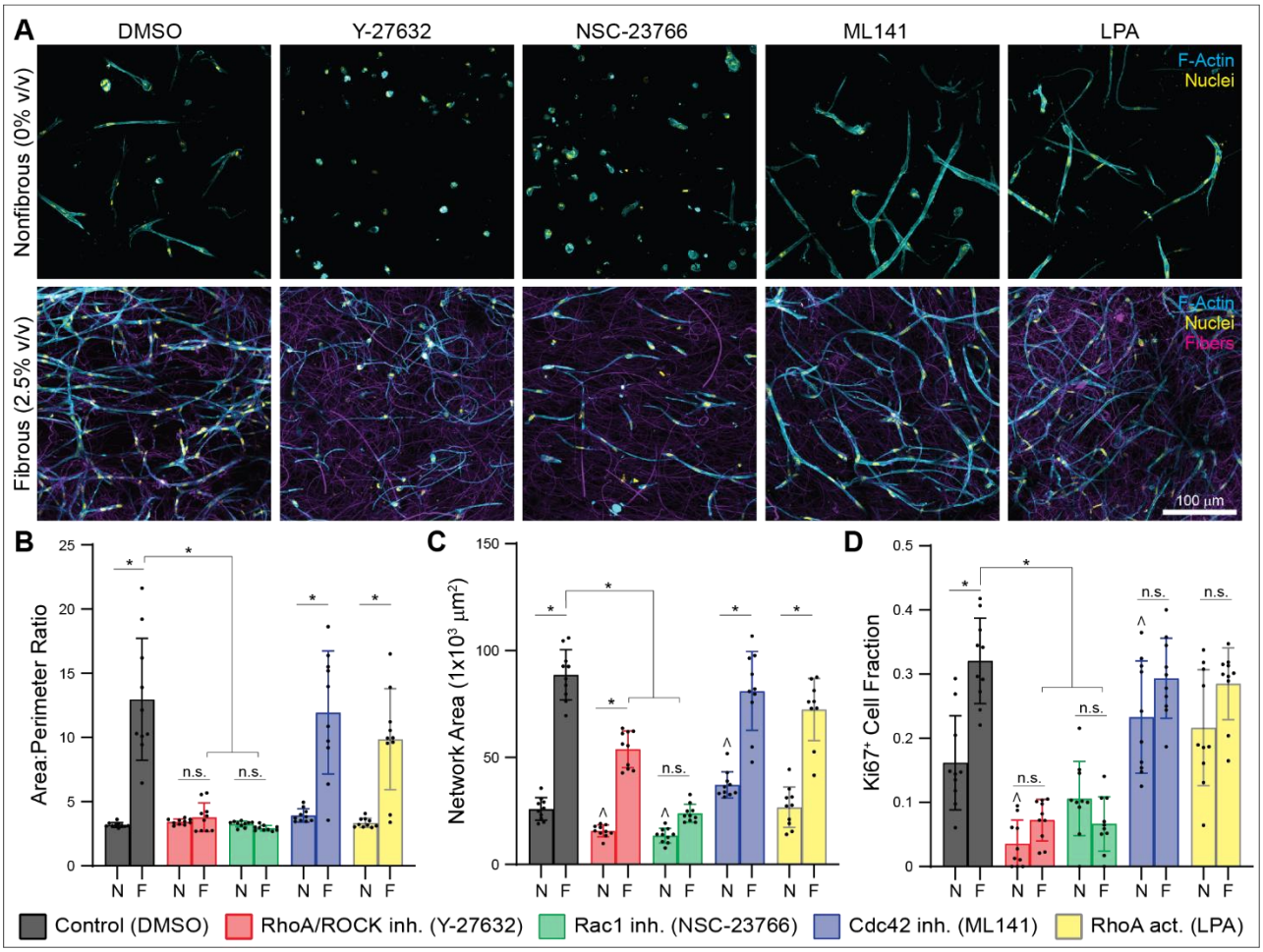

Figure 5.4: Fiber-mediated multicellular network assembly as a function of pharmacologic modulation of Rho GTPases. A) High-magnification images of fibroblast morphology and network formation in nonfibrous and fibrous DexVS hydrogels, after 5 days of culture in the presence of denoted pharmacologic modulators or DMSO (F-actin (cyan), nuclei (yellow), DexVS fibers (magenta); scale bars: 100 μm). Corresponding image quantification of B) F-actin cellular A/P ratio, C) F-actin network area, and D) the fraction of Ki67+ cells within each network (n=4 samples/group; area n>10 fields of view/group and n>25 cells/field of view). Ki67+ cells were defined as cells with co-localization of Ki67 and DAPI. All data presented are means ± standard deviations; asterisk denotes significance with $p < 0.05$ determined by a two-way analysis of variance; ^ denotes significance relative to DMSO containing conditions as determined via a post hoc Dunnett's multiple comparison test.

Activated fibroblasts possess stress fibers and migratory capacity, and more frequently undergo cell division during the inflammatory and proliferative stages of wound healing. However, their differentiation towards highly contractile α-SMA+ myofibroblasts coincides with the initiation of the remodeling phase, marked by ECM synthesis and tissue contraction (Boris

Hinz, 2007). Thus, here we explored whether ROCK, Rac1, or Cdc42 activity were critical for MF differentiation in 3D fibrous environments. Fibroblasts were encapsulated in nonfibrous control and fibrous hydrogels (day 0), allowed 24 hours for spreading, and then culture media was supplemented with the profibrotic cytokine TGF- β1 (days 1-9), given its pleotropic roles during wound healing and MF differentiation *in vivo* (Scharenberg et al., 2014). Indeed, TGF- β1 supplementation was necessary for MF differentiation in DexVS hydrogels regardless of the presence of fibers **(Figure 5.5A,B)**, although matrix fibers synergized with TGF- β1 to increase fibroblast proliferation **(Figure 5.5C)** and the appearance of α-SMA$^+$ MFs **(Figure 5.5B)**, as we have previously reported (Matera et al., 2020).

To account for the significant variation in proliferation rates across pharmacologic treatments observed in previous experiments **(Figure 5.4)**, we allowed fibroblasts to spread, proliferate, and form multicellular networks prior to the introduction of cytoskeletal modulators on day 5. ROCK, Rac1, or Cdc42 inhibition all reduced MF differentiation in fibrous composites, although not to levels of nonfibrous controls **(Figure 5.5A, 5.5B)**. As evidenced by low A/P ratios in nonfibrous conditions **(Figure 5.5C)**, limited multicellular network formation may be another reason why MF differentiation was limited in the absence of fibers. Indeed, A/P ratios were also reduced in treatment conditions with lower α-SMA$^+$ fibroblasts in fibrous gels **(Figure 5.5C)**, further associating multicellular network formation with MF differentiation. In summary, these results suggest that while ROCK and Rac1 inhibition are effective in reducing fiber-mediated contact guidance **(Figure 5.2)**, migration **(Figure 5.3)**, and proliferation/network formation **(Figure 5.4)** in fibroblasts, their targeting alone is not sufficient to completely inhibit MF differentiation once fibroblast networks have formed. Furthermore, these results are consistent with various *in vivo* models showing that Rac1, ROCK, and Cdc42 activity are all critical for

wound closure and organ fibrosis (Edlund, Landström, Heldin, & Aspenström, 2002; S. Liu et al., 2009, 2008; Pothula, Bazan, & Chandrasekher, 2013; Shimizu et al., 2001), yet contrast work showing enhanced MF differentiation with Rac1 ablation *in vitro* (Ge et al., 2018; Igata et al., 2010). However, given that Rac1 inhibition has also been shown to inhibit MF differentiation in other contexts (Choi et al., 2010; Shi-wen et al., 2009) it is likely that Rac1 has differing effects as a function of cell type and culture setting.

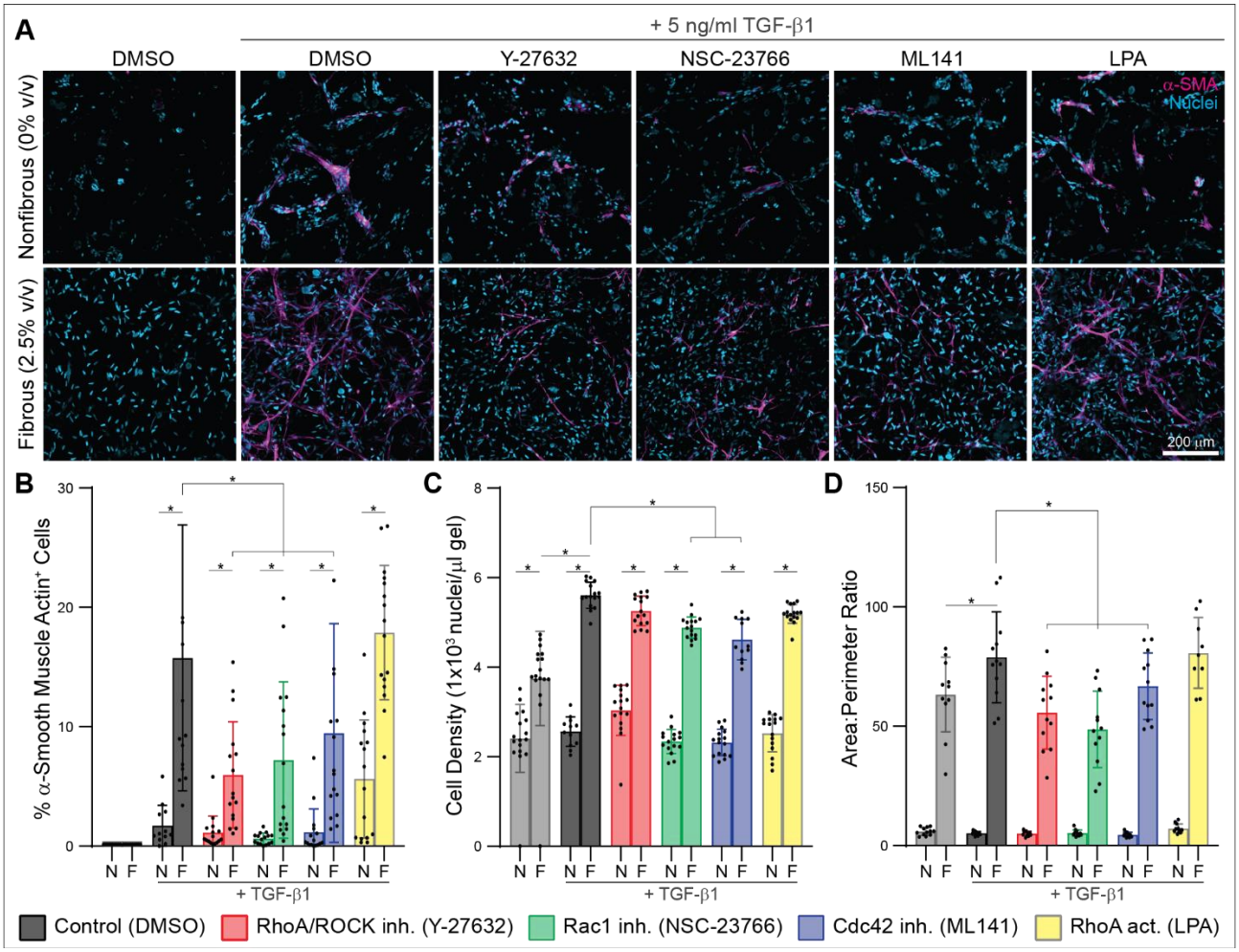

Figure 5.5: Fiber-mediated myofibroblast differentiation as a function of pharmacologic modulation of Rho GTPases. A) Confocal images of the myofibroblast marker α-SMA within nonfibrous and fibrous DexVS hydrogels after 9 days of culture in the presence of stimulatory cytokine TGF- β1 or control media. Starting on day 5 after network formation, cultures were exposed to denoted pharmacologic modulators or DMSO until fixation (α-SMA (magenta), nuclei (cyan); scale bars: 400 μm). Corresponding image quantification of B) α-SMA+ cells, C) total nuclei, and D) F-actin area:perimeter ratio (n=4 samples/group; area n>10 fields of view/group and n>800 cells/field of view). α-SMA+ cells were defined as cells with co-

localization of F-actin and α-SMA. All data presented are means ± standard deviations; asterisk denotes significance with $p < 0.05$ determined by a two-way analysis of variance. Significance relative to TGF- β1 containing conditions was determined via a post hoc Dunnett's multiple comparison test.

While proliferation and α-SMA expression are accepted markers of differentiated MFs, these cells functionally contribute to wound repair in part through macroscale tissue contraction and resultant closure of wound margins. To explore how modulation of ROCK, Rac1, and Cdc42 activity affect the contractile function of MFs over longer time scales, we repeated the prior experiment but detached hydrogels from underlying tissue culture plastic, creating free-floating hydrogels amenable to bulk contraction. Given the limited MF differentiation and proliferation observed in nonfibrous DexVS hydrogels, only fibrous conditions were explored in this study. As expected, hydrogel contraction was enhanced with TGF- β1 supplementation as evidenced by lower final hydrogel areas on day 14 **(Figure 5.6)**. Unexpectedly, however, nearly all treatment conditions (Y-27632, NSC-23766, ML141) reduced hydrogel contraction to levels seen in control conditions lacking exogenously added TGF- β1, despite the fact that MFs were detected in Y-27632, NSC-23766, and ML141 treated samples by day 9 **(Figure 5.5)**. Furthermore, given that hydrogel contraction still occurred in conditions lacking TGF- β1, where differentiated MFs were undetectable, these data suggest that the capacity of fibroblasts to contract tissues is not fully dependent α-SMA expression, and that inhibition of ROCK, Rac1, and Cdc42 is sufficient to diminish the contractility of undifferentiated fibroblasts. This is in contrast to the literature suggesting that RhoA/ROCK activity is the primary driver of fibroblast contraction and force generation in 2D (Huang et al., 2012; Oh, Haak, Smith, & Ligresti, 2018), but perhaps is not surprising given the well-known role of Rac1 and Cdc42 in regulating actin polymerization and cell-cell adhesion in other contexts (Tapon & Hall, 1997).

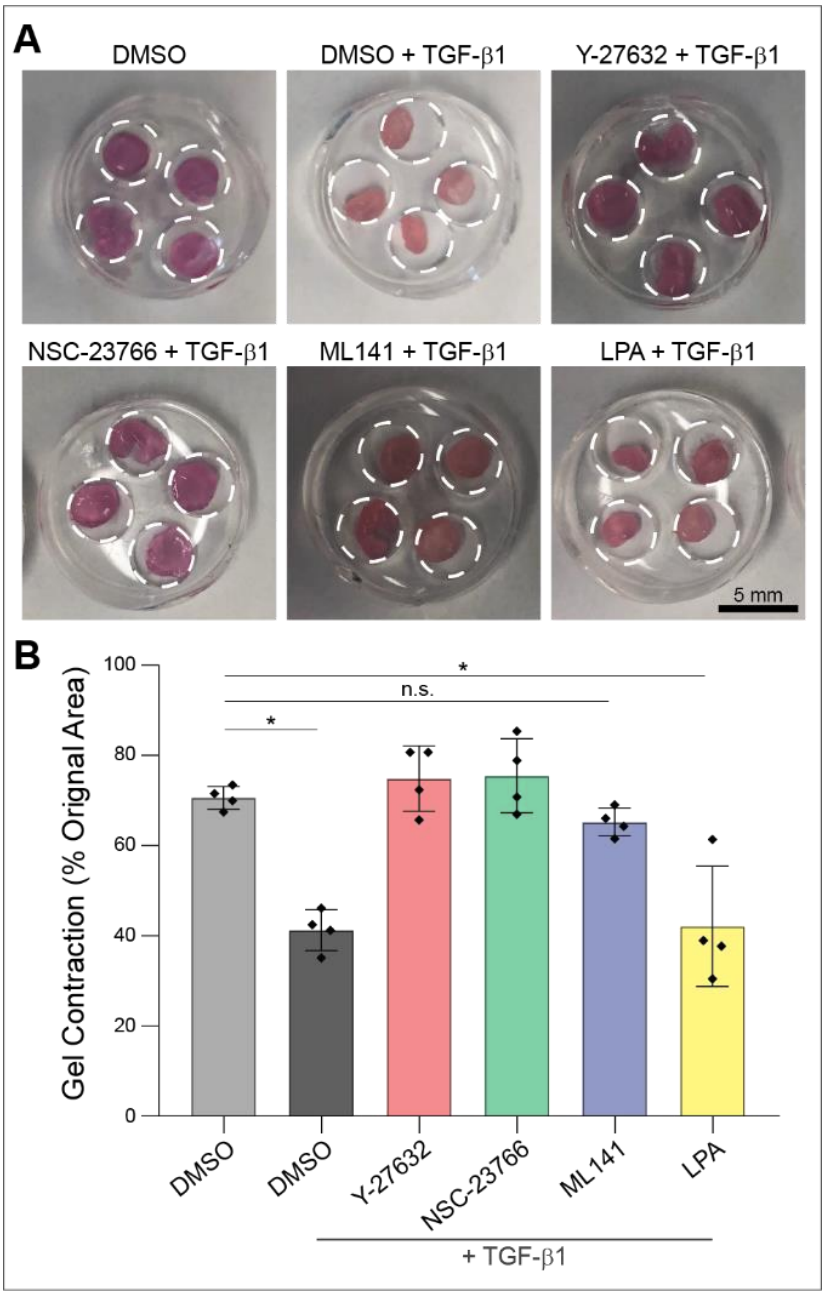

Figure 5.6: Fiber-mediated hydrogel contraction as a function of pharmacologic modulation of Rho GTPases. A) Macroscopic images of a DexVS contraction assay after 14 days of culture in the presence of stimulatory cytokine TGF- β1 or media control. Starting on day 5, cultures were exposed to denoted pharmacologic modulators or DMSO vehicle control until fixation. Dashed line surrounding each hydrogel gasket has a 15mm diameter. B) Corresponding image quantification of DeXS hydrogel contraction on day 14 (n=4 25ul hydrogels per group). All data presented are means ± standard deviations; asterisk denotes significance with $p < 0.05$ determined by a one-way analysis of variance.

5.5 Discussion

Despite the critical role of wound healing processes during tissue homeostasis and fibrotic diseases, few studies have investigated the interplay between the fibrous structure present in provisional matrix and key cytoskeletal regulators in 3D microenvironments(Barker & Engler, 2017; Klingberg, Hinz, & White, 2013). Wound healing models *in vitro* are most frequently protease-independent 2D scratch wound assays lacking fibrous microstructure, or alternatively reconstituted collagen gels that lack a proteoglycan component and have limited tunability (Liang et al., 2007; Pathak & Kumar, 2011). To address this, here we leveraged electrospinning and hydrogel chemistries to generate a biomimetic model of fibronectin-rich provisional matrix; this synthetic approach allowed us to define the density of matrix fibers without affecting initial 3D hydrogel stiffness or degradability, factors that are determined by the gel-like proteoglycan component. Pairing this approach with well-characterized pharmacologics allowed us to dissect the interplay between Rho GTPases and matrix fibers that controls fibroblast behavior during key phases of wound repair. We found that fiber-mediated spreading and migration required both Rac1 and ROCK activity, highlighting a role for these GTPases during the inflammatory phase of wound repair **(Figure 5.2, 5.3)**. During the proliferative phase of wound repair, Rac1 and ROCK were both critical for network formation and proliferation of fibroblasts **(Figure 5.4)**. Finally, despite ample literature highlighting RhoA/ROCK activity as the driver of MF differentiation in 2D, here we show that Rac1 and Cdc42 were additionally important for the 3D differentiation and contractile function of MFs at late timepoints **(Figure 5.5, 5.6)**.

Beyond characterizing various stages of the wound repair program in fibroblasts, these results add to our understanding of fibroblast-ECM interactions in 3D tissues which occurs

throughout developmental processes, ECM homeostasis, and fibrotic disease (Humphrey et al., 2014). First, we propose a developing mechanism for cell spreading in 3D fibrous environments whereby matrix fibers drive the initiation of thin nascent protrusions in a Rac1 dependent manner **(Figure 5.2)**, followed by RhoA/ROCK dependent expansion of these protrusions into thicker, spindle-like structures containing F-actin stress fibers **(Figure 5.3)**. These results suggest that the previously associated morphologies established in 2D studies (whereby Rac1 drives lamellipodium creation, Cdc42 drives filopodia, and RhoA/ROCK drive stress fiber development) does not directly translate to more complex 3D and fibrous environments. More specifically, steric hindrance from surrounding matrix in 3D appears to prevent the formation of flat sheet-like actin structures comprising lammelipodia, instead favoring the formation of protrusions more reminiscent of large filopodia. Importantly, and quite distinct from 2D findings, these protrusions appear to require Rac1 activity and are not Cdc42 dependent. Fibers appear to provide contact guidance cues and direct localized Rac1 activity, perhaps in a similar fashion to our previous studies microcontact printing adhesive lines of fibronectin (W. Y. Wang et al., 2018).

Secondly, while prior work suggests that RhoA/ROCK and Rac1 signaling are in opposition in 2D (Pertz, Hodgson, Klemke, & Hahn, 2006; Sander, Ten Klooster, Van Delft, Van Der Kammen, & Collard, 1999), these results suggest that they work in concert to support cell spreading and downstream actomyosin-dependent processes (eg. migration, proliferation, multicellular network formation, MF differentiation, and contractile force generation). Indeed, the independence of ROCK and Rac1 in 2D is notable; in these contexts Rac1 inhibition prevents the formation of protrusions (Ge et al., 2018) but does not hinder the generation of F-actin rich stress fibers **(Supplemental Figure 5.1)**. This is likely through elevated RhoA/ROCK activity in

situations where Rac1 is absent (Pertz et al., 2006), in addition to the lack of steric hindrance from a surrounding 3D matrix. In contrast, protrusion formation appears to be a prerequisite for stress fiber generation in 3D **(Figure 5.2, 5.5)**. However, as evidenced by the low spread area despite an increased number of nascent protrusions in Y-27632 treated conditions **(Figure 5.2,5.3)**, protrusion formation appears to be necessary but not sufficient for stress fiber generation in 3D. Consequently, we hypothesize that insufficient coordination between Rac1 and ROCK is the primary reason for limited spreading in amorphous nonfibrous 3D hydrogels (Matera et al., 2019) **(Figure 5.1-5.3)**; a lack of ligand presenting guidance cues in 3D hinders Rac1 activation, preventing the formation of nascent protrusions which serve as scaffolds for downstream actin polymerization and ROCK-dependent stress fiber generation. Indeed, we did observe stress fibers in NSC-27632 treated cultures which were allowed to generate protrusions prior to dosing on day 5 **(Figure 5.5, Supplemental Figure 5.1)**, suggesting that Rac1 is needed before but not during stress fiber development in 3D.

Beyond contributing to a developing understanding of 3D mechanosensing, our work also has implications for the treatment of chronic wounds and fibrotic diseases. In the context of wound repair, material-based strategies have emerged as a promising tool to accelerate healing but have yet to be fully realized (Griffin, Weaver, Scumpia, Di Carlo, & Segura, 2015). Our documentation of increased fibroblast migration, proliferation, and matrix remodeling in the presence of matrix fibers supports prior work showing the benefit of fibrous scaffolds in treating dermal, orthopedic, and cardiac wounds (Coburn et al., 2011; Hassiba et al., 2016; Ravichandran et al., 2012) . Importantly, emerging hydrogel technologies have numerous benefits (injectability, viscoelasticity, swelling capacity, non-fouling properties, etc.) but typically lack fibrous microstructure; our fiber-reinforcement technique is compatible across hydrogel platforms

(Matera et al., 2019) and can be paired with developing technologies to enhance cell infiltration, spreading, and proliferation responses if desired. Furthermore, the complex dynamics of wound healing *in vivo* suggests differential adhesive and cytoskeletal states of fibroblasts depending on their required function – optimizing wound healing may require modulating Rho GTPases through cell engineering or dynamic material cues rather than a single material with a statically defined set of properties and resultant cell states(S. Kim, Uroz, Bays, & Chen, 2021).

In contrast, it would be advantageous to prevent fibroblast migration, proliferation, and MF differentiation in the context of fibrotic diseases. Our results suggest that inhibiting any of the key cytoskeletal regulators was insufficient in preventing 3D MF differentiation in the presence of TGF- β1 and matrix fibers **(Figure 5.5)**, particularly after fibroblasts have proliferated and formed cell-cell junctions **(Supplemental Figure 5.1)**, as is the case in clinically detectable fibrosis. Indeed, fibroblasts undergoing MF differentiation at late timepoints appeared to be resistant to drug treatment when compared to immediate dosing of recently encapsulated fibroblasts, where the effect of fibers on cell spreading **(Figure 5.2)**, proliferation **(Figure 5.4D)**, and network formation **(Figure 5.4B)** was reversed under ROCK and Rac1 inhibition. Pharmacologic resistance may be one reason why drugs targeting mechanosensitive pathways have yet to be realized for the treatment of fibrotic disease, despite the well-established requirement of cell-matrix signaling for MF differentiation in 2D over short time scales (Smithmyer et al., 2014). It is also important to note that we used pharmacologic agents to disrupt ROCK, Rac1, and Cdc42 activity in this work, therefore it is possible that more elegant technologies which inhibit protein synthesis (siRNA, CRISPR knockouts) may have more pronounced effects and should be explored in future work.

Importantly, this work is not without limitations. We did not explore how matrix fibers influence 3D Rac1 activity at the subcellular level, or a detailed mechanism by which nascent protrusions develop into larger 3D cytoskeletal structures. Similarly, our observation that Cdc42 inhibition promoted 3D migration is discordant with findings from 2D models, and may be due to the interplay between Cdc42 and matrix metalloproteinase (MMP) activity (Deroanne et al., 2005), a link that would be inconsequential in 2D given that matrix degradation is not required for migration in such contexts (Yamada & Sixt, 2019). Further development of optogenetic tools, live activity reporters, and high-resolution timelapse imaging could enable future exploration and quantification of these complex and dynamic 3D cytoskeletal processes (Matera, Wang, & Baker, n.d.). Furthermore, recent work from our lab and others has demonstrated that cell-derived ECM is rapidly deposited in 3D hydrogels (Loebel et al., 2020; Matera et al., 2020); we cannot exclude the potential for changes in ligand density across conditions over time, or for potential differences in integrin engagement to RGD-presenting fibers compared to cell-derived fibronectin. Indeed, emerging technologies such as metabolic labeling(Loebel et al., 2020) may allow for quantification and investigation of ligand-specific effects. Finally, RGD-presenting fibers and a polymeric gel were utilized to model the biphasic structure (adhesive fibrillar proteins and degradable gel-like proteoglycans) present *in vivo;* we present this material as a reductionist approach to mimicking a complex physiologic stromal ECM. Future material development will be required to capture the heterogeneity of matrix proteins (e.g. collagen, elastin, fibronectin) and mechanical properties present in diverse tissue structures *in vivo.*

In summary, here we utilized a fibrous hydrogel model to explore the stimulatory effects of matrix fibers on fibroblast phenotype and documented the role of Rho GTPases during key cell processes during wound healing. These results emphasize the need to model complex

biological processes, such as wound healing or fibrosis, in distinct cellular phases. Indeed, the timing of pharmacologic treatment is likely to have differing effects depending on the stage of the physiologic process being modeled; further development of bioengineering tools which offer on-demand changes to the matrix- or cell-state will be a critical next step. Future work should also explore the role that other cell types (macrophages, endothelial cells, and mesenchymal stem cells) play during the wound healing process and whether they are influenced by fibers through similar mechanisms. Moreover, given the differences in mechanosensing between 2D, 3D, and 3D fibrous environments, this work motivates the development and implementation of biomimetic models which can elucidate physiologic understanding and support therapeutic translation.

5.6 Materials and Methods

5.6.1 Reagents

All reagents were purchased from Sigma Aldrich and used as received, unless otherwise stated.

5.6.2 Synthesis and Fabrication

Dextran vinyl sulfone (DexVS) was synthesized using a previously established protocol for vinyl sulfonating polysaccharides adapted for use with high MW dextran (MW 86,000 Da, MP Biomedicals, Santa Ana, CA) (Davidson et al., 2020; Matera et al., 2019). Briefly, pure divinyl sulfone (12.5 ml, Fisher Scientific, Hampton, NH) was added to a sodium hydroxide solution (0.1 M, 250 mL) containing dextran (5 g). This reaction was carried out at 1500 RPM for 3.5 minutes, after which the reaction was terminated by adjusting the pH to 5.0 via the addition of hydrochloric acid. A lower functionalization of DexVS was utilized for hydrogels, where the volume of divinyl

sulfone reagent was reduced to 3.875 ml. All reaction products were dialyzed for 5 days against Milli-Q ultrapure water, with two water exchanges daily, and then lyophilized for 3 days to obtain the pure product. Functionalization of DexVS was characterized by ^{1}H –NMR spectroscopy in D_2O and was calculated as the ratio of the proton integral (6.91 ppm) and the anomeric proton of the glucopyranosyl ring (5.166 and 4.923 ppm), here a vinyl sulfone/dextran repeat unit ratio of 0.376 and 0.156 was determined for electrospinning and hydrogel DexVS polymers, respectively.

For fiber fabrication, DexVS was dissolved at 0.6 g ml^{-1} in a 1:1 mixture of Milli-Q ultrapure water and dimethylformamide with 0.015% Irgacure 2959 photoinitiator. Methacrylated rhodamine (0.5 mM; Polysciences, Inc., Warrington, PA) was incorporated into the electrospinning solution to fluorescently visualize fibers. This polymer solution was utilized for electrospinning within an environment-controlled glovebox held at 21 ˚C and 30% relative humidity. Electrospinning was performed at a flow rate of 0.3 ml h^{-1}, gap distance of 5 cm, and voltage of -10.0 kV onto a grounded collecting surface attached to a linear actuator. Fiber layers were collected on glass slabs and primary crosslinked under ultraviolet light (100mW cm^{-2}) and then secondary crosslinked (100 mW cm^{-2}) in a 1mg mL^{-1} Irgacure 2959 solution. After polymerization, fiber segments were resuspended in a known volume of PBS (typically 3 ml). The total volume of fibers was then calculated via a conservation of volume equation: total resulting solution volume = volume of fibers + volume of PBS (3 ml). After calculating total fiber volume, solutions were re-centrifuged, supernatant was removed, and fiber pellets were resuspended to create a 10 vol% fiber solution, which were then aliquoted and stored at 4^{o} C. To support cell adhesion, 2.0 mM RGD (CGRGDS, 2.0 mM, Genscript, George Town, KY), was coupled to vinyl sulfone groups along the DexVS backbone via Michael-type addition chemistry for 30 min, followed by quenching of excess VS groups in a 300 mM cysteine solution for 30 minutes. To

remove free thiols after quenching, fiber solutions were vigorously rinsed via flushing with excess PBS three times before use in cell studies.

For hydrogel formation, DexVS gels were formed via a thiol-ene click reaction at 3.3% w/v (pH 7.4, 37°C, 45 min) with VPMS crosslinker (12.5mM) (GCRDVPMSMRGGDRCG, Genscript, George Town, KY) in the presence of heparin-binding peptide (HBP, GCGAFAKLAARLYRKA, 0.65 mM, Genscript, George Town, KY), and fiber segments (0.0-2.5% v/v). Cysteine was added to precursor solutions to maintain a final vinyl sulfone concentration of 60 mM after gelation. All hydrogel and peptide precursor solutions were made in PBS containing 50 mM HEPES. To create fibrous hydrogels, a defined stock solution (10% v/v) of suspended fibers in PBS/HEPES was mixed into hydrogel precursor solutions prior to gelation. Via controlling the dilution of the fiber suspension, fiber density was readily tuned within the hydrogel at a constant hydrogel weight percentage. For gel contraction experiments, DexVS was polymerized within a gelatin-coated 5 mm diameter PDMS gasket to ensure consistent hydrogel area beginning on day 0.

5.6.3 Cell Culture and Biological Reagents

Normal human lung fibroblasts (University of Michigan Central Biorepository were cultured in DMEM containing 1% penicillin/streptomycin, L-glutamine and 10% fetal bovine serum (Atlanta biologics, Flowery Branch, GA). Cells were passaged upon achieving 90% confluency at a 1:4 ratio and used for studies until passage 7. For all hydrogel studies, cells were detached with 0.05% trypsin-EDTA (Life Technologies), counted and either encapsulated into or seeded onto 12.5 µl hydrogels at a density of 1,000,000 cells ml^{-1} of hydrogel, and subsequently cultured at 37°C and 5% CO2 in serum containing medium. For 2D studies of cell morphology F-

actin organization (Supplementary **Figure** 1), the total number of cells seeded onto each 12 mm glass coverslip was equivalent to 12.5ul hydrogels described above. Media was refreshed the day after encapsulation and every 2 days after. For migration studies, fibroblasts were trypsinized (0.05%), counted, formed into 300 cell aggregates overnight in an AggreWell™ (STEMCELL Technologies, Vancouver, BC, Canada) substrate treated with 0.5% pluronic F-127 to prevent cell adhesion, and encapsulated into DexVS hydrogels after 24 hours. In differentiation experiments, recombinant human TGF- β1 (Peprotech, Rocky Hill, NJ) was supplemented to media at 5 ng ml^{-1}. For pharmacological studies, Y-27632 (30 μM, Fisher Scientific, Hampton, NH), NSC-27366 (50 μM, Fisher Scientific, Hampton, NH), ML141 (20 μM), and LPA (15 μM), were supplemented to media and refreshed every 2 days.

5.6.4 Fluorescent staining, microscopy, and analysis:

Cultures were fixed with 4% paraformaldehyde for 30 min at room temperature. To stain the actin cytoskeleton and nuclei, samples were permeabilized in PBS solution containing Triton X-100 (0.5% v/v), sucrose (10% w/v), and magnesium chloride (0.6% w/v), blocked in 1% BSA, and stained simultaneously with phalloidin and DAPI. For immunostaining, samples were permeabilized, blocked for 8 h in 1% w/v bovine serum albumin, and incubated with mouse monoclonal anti-α-SMA (1:2000, Sigma #A2547) or rabbit monoclonal anti-Ki67 (1:500, Sigma-Aldrich #PIMA514520) followed by secondary antibody for 6 h each at room temperature with 3x PBS washes in between. All samples were imaged on a Zeiss LSM 800 laser scanning confocal microscope. High-resolution images of F-actin were acquired with a 40x water-immersion objective. Unless otherwise specified, images are presented as maximum intensity Z-projections of 25 (**Figure** 2), 50 (**Figure** 4), 100 (**Figure** 1,5) or 300μm (**Figure** 3) Z-stacks, respectively. Single cell morphometric analyses (cell aspect ratio) were performed using custom

Matlab scripts with sample sizes > 25 cells/group, while total F-actin spread area, α-SMA, and Ki67 were quantified on an image basis with a minimum of 10 distinct fields of view. 3D migration characteristics were determined via custom Matlab scripts utilizing n>10 fibroblast aggregates/group, with invasions designated as nucleated F-actin+ structures with aspect ratios >2. Migration heatmaps are presented as an overlay of all biological replicates. Myofibroblasts were denoted as nucleated, F-actin^{+}, α-SMA^{+} cells. For cell density (# of nuclei) calculations, DAPI-stained cell nuclei were thresholded and counted in six separate 600 x 600 x 200 μm image volumes, allowing us to calculate a total number of cells per mm^3 of gel. α-SMA analysis was conducted via a custom Matlab script; briefly, cell outlines were created via α-SMA masking and the total number of nuclei were quantified under each α-SMA mask on a per image basis. A similar analysis method in Matlab was used for area:perimeter ratio as published previously, where higher area:perimeter ratios indicate the formation of a more interconnected network of interconnected cells(Davidson et al., 2019).

To determine the elastic modulus of DexVS hydrogels, indentation tests were performed with a Nanosurf FlexBio atomic force microscope (AFM; Nanosurf, Liestal, Switzerland). Samples were indented with a 5 μm diameter colloidal probe tip (spring constant = 0.03 N/m) to a depth of 10 μm at a rate of 0.333 μm/s. Resulting force-displacement curves were fit to a spherical Hertz model utilizing AtomicJ, assuming a Poisson's ratio of 0.5.

Statistical significance was determined by one-way and two-way analysis of variance (ANOVA) or Student's t-test where appropriate, with significance determined by $p<0.05$. All data are presented as a mean ± standard deviation.

5.7 Supplementary Figures

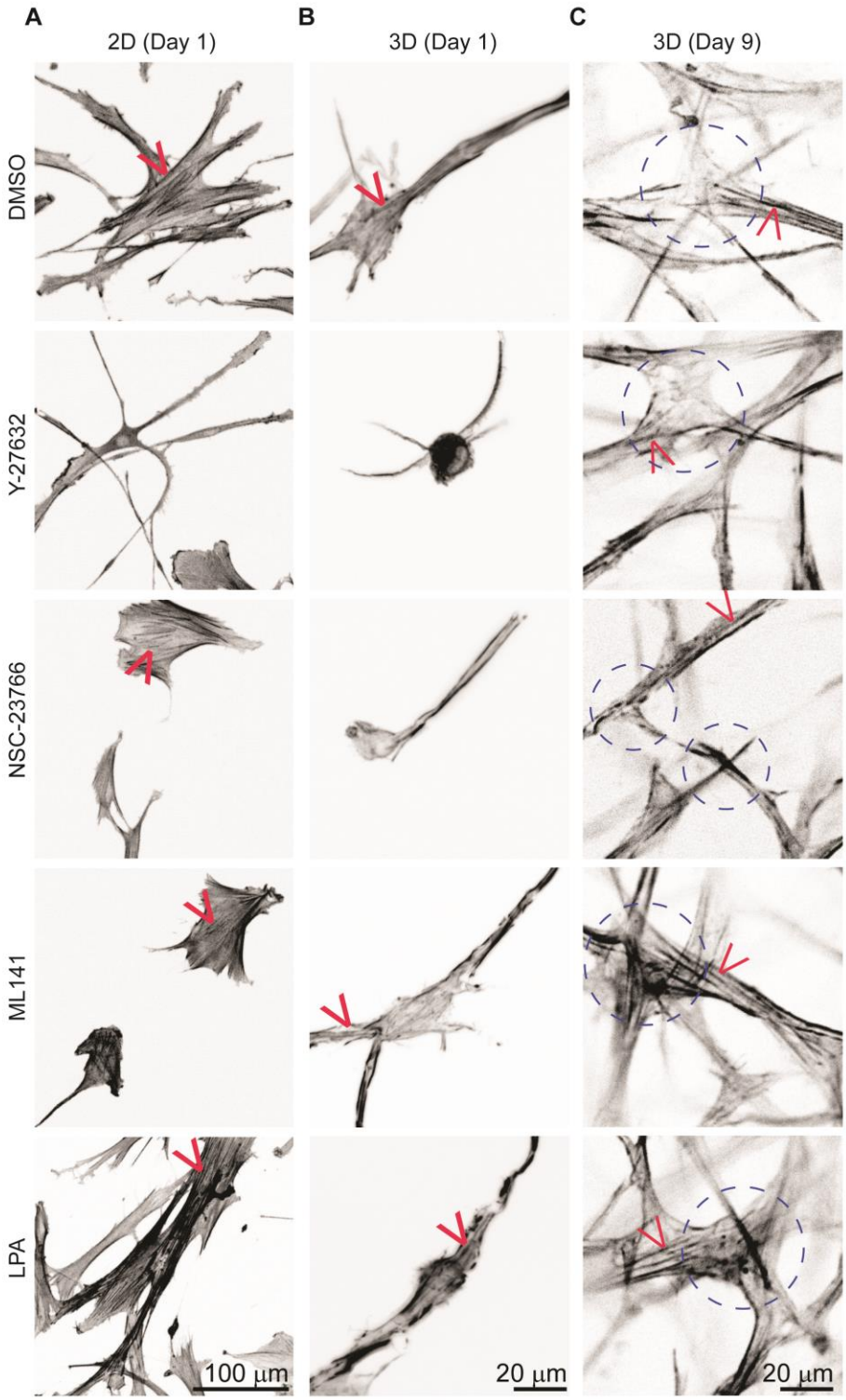

Supplemental Figure 5.1: Cytoskeletal morphology in fibroblasts after treatment with cytoskeletal regulators. A) Representative high-resolution images of F-actin inversions after

seeding fibroblasts on 2D tissue culture plastic. After attachment (2 hours) cultures were stimulated with denoted pharmacologics for 24 hours. Scale bars: 100μm. Red arrows indicate examples of F-actin stress fibers, designated as non-cortical linear F-actin bundles with diameters >1μm. B) Representative high-resolution images of F-actin inversions after fibroblast culture within 3D fibrous DexVS gels (FD 2.5%). Cultures were stimulated with denoted pharmacologics for 24 hours. Red arrows indicate examples of F-actin stress fibers, designated as non-cortical linear F-actin bundles with diameters >1μm. Scale bars: 20μm. C) Representative high-resolution images of F-actin inversions after fibroblast culture within 3D fibrous DexVS gels (FD 2.5%) for 9 days in the presence of TGF-β1. Starting on day 5, cultures were stimulated with denoted pharmacologics every other day until fixation. Red arrows indicate examples of F-actin stress fibers, designated as non-cortical linear F-actin bundles with diameters >1μm. Blue circles highlight regions containing cell-cell junctions, denoted as areas of cytoskeletal intersection between nucleated fibroblasts. Scale bars: 20μm. Images reflect a single 50μm thick Z-plane.

Chapter 6: A Transcriptomics Based Approach to Investigate PF

6.1 Authors

Daniel L. Matera, Jingyi Xia, Brendon M. Baker

6.2 Abstract

While single-cell RNA sequencing has recently provided new insight into the pathobiology of pulmonary fibrosis, it has been challenging to conduct a robust analysis on the mesenchymal and endothelial populations present in fibrotic tissue. This is, in part, due to the low yield of stromal cells when digesting lung tissue. Here, we use standard bioinformatics approaches to integrate three publicly available single-cell pulmonary fibrosis datasets. We conduct a comprehensive analysis of various endothelial and mesenchymal subtypes in the lung, focusing on two populations marked by the POSTN gene that uniquely expand in patients with pulmonary fibrosis. Via exploring the pathway dysregulation shared by POSTN+ cell types, we identify potential pharmacologics that hold promise for the therapeutic treatment of pulmonary fibrosis. Furthermore, via conducting single-cell RNA sequencing on a bioengineered model of pulmonary fibrosis, we identify distinct fibroblast subpopulations that exist *in vitro* and discuss

the relative advantages and limitations of bioengineered disease models. This work provides a foundation for investigating stromal cell heterogeneity in pulmonary fibrosis.

6.3 Introduction

A progressive and fatal lung disease, idiopathic pulmonary fibrosis (PF) is characterized by the extensive deposition of extracellular matrix (ECM) in the distal regions of the lung. During progression, parenchymal structures (alveoli, terminal bronchioles, peripheral veins and capillaries) are disrupted and replaced with non-functional scar tissue, ultimately contributing to lung failure (Kendall & Feghali-Bostwick, 2014). Myofibroblasts (MFs) are thought to be the critical drivers of ECM deposition and aberrant tissue-remodeling in PF. Unfortunately, pharmacologics designed to limit MF differentiation and ECM remodeling *in vitro* have largely been unsuccessful in the clinic, with limited reductions in patient mortality or disease progression (X. Li, Zhu, Wang, Yuan, & Zhu, 2017; Wongkarnjana, Yanagihara, & Kolb, 2019). In fact, the first FDA approved drugs for PF, Pirfenidone (PFD) and Nintedanib (NTB), target fibroblasts in addition to numerous other cell types such as macrophages, alveolar epithelial cells, and endothelial cells (Richter et al., 2018). While PFD and NTB are far from curative, the success of two broad-spectrum pharmacologics suggest that targeting multiple cell types concurrently may be required for the development of an advantageous IPF therapy. As a result, a precise understanding of cellular heterogeneity within IPF may be critical going forward.

While the cellular diversity of the lung has been long appreciated, recent work utilizing single-cell RNA-sequencing (scRNA-seq) has documented the cellular landscape of the lung at an unprecedented fidelity (Jin et al., 2021; Sit et al., 2019). Similarly, scRNA-seq of fibrotic lungs has identified numerous subtypes previously unrecognized, including novel populations of bronchiolar and alveolar epithelial cells that may affect tissue repair processes (Habermann et al.,

2019; Reyfman et al., 2019; Schaum et al., 2020). Indeed, while a critical role of MFs is established, the upstream cellular and paracrine contributors to their accumulation in human disease is less clear. More specifically, while the role of cell types such as macrophages and AT2 cells are acknowledged during fibrosis progression, the contribution of stromal cells beyond the MF (e.g. endothelial cells and other fibroblast lineages) to fibrosis has been understudied (Bagnato & Harari, 2015). In contrast, recent developmental biology studies have highlighted a critical role for alveolar endothelial cells and lipofibroblasts in regulating lung homeostasis (El Agha et al., 2017). An enhanced analysis of stromal cell diversity in PF could identify new cell types and highlight their potential biochemical functions in a fibrotic context.

Given the recent establishment of various cell atlases (Sit et al., 2019; Tsukui et al., 2020; Wilbrey-clark, Roberts, & Teichmann, 2020), here we set out to conduct a comprehensive analysis of stromal cell identity and function in PF. As stromal cell yield is low from pulmonary isolates, we aggregated publicly available scRNA-seq datasets from healthy and diseased donors using an established integration framework on ~400,000 cells. Focusing on stromal cells, we then characterized 6 endothelial and 5 fibroblast subtypes which were recently identified, including three subtypes which appear to be unique to PF lung. Following a detailed transcriptomic analysis of each subtype, we identify key convergent pathways shared by stromal cells within PF lung. Furthermore, we conducted SC-RNA-SEQ on a bioengineered model of PF to inform whether stromal cell heterogeneity can be recapitulated an *in vitro* platform amenable to drug screening. Our results serve to characterize known stromal populations in fibrotic lung, present a transcriptomic roadmap for the further development of tissue-engineered diseases models, and highlight critical implications for the stromal cell heterogeneity observed in PF.

6.4 Results and Discussion

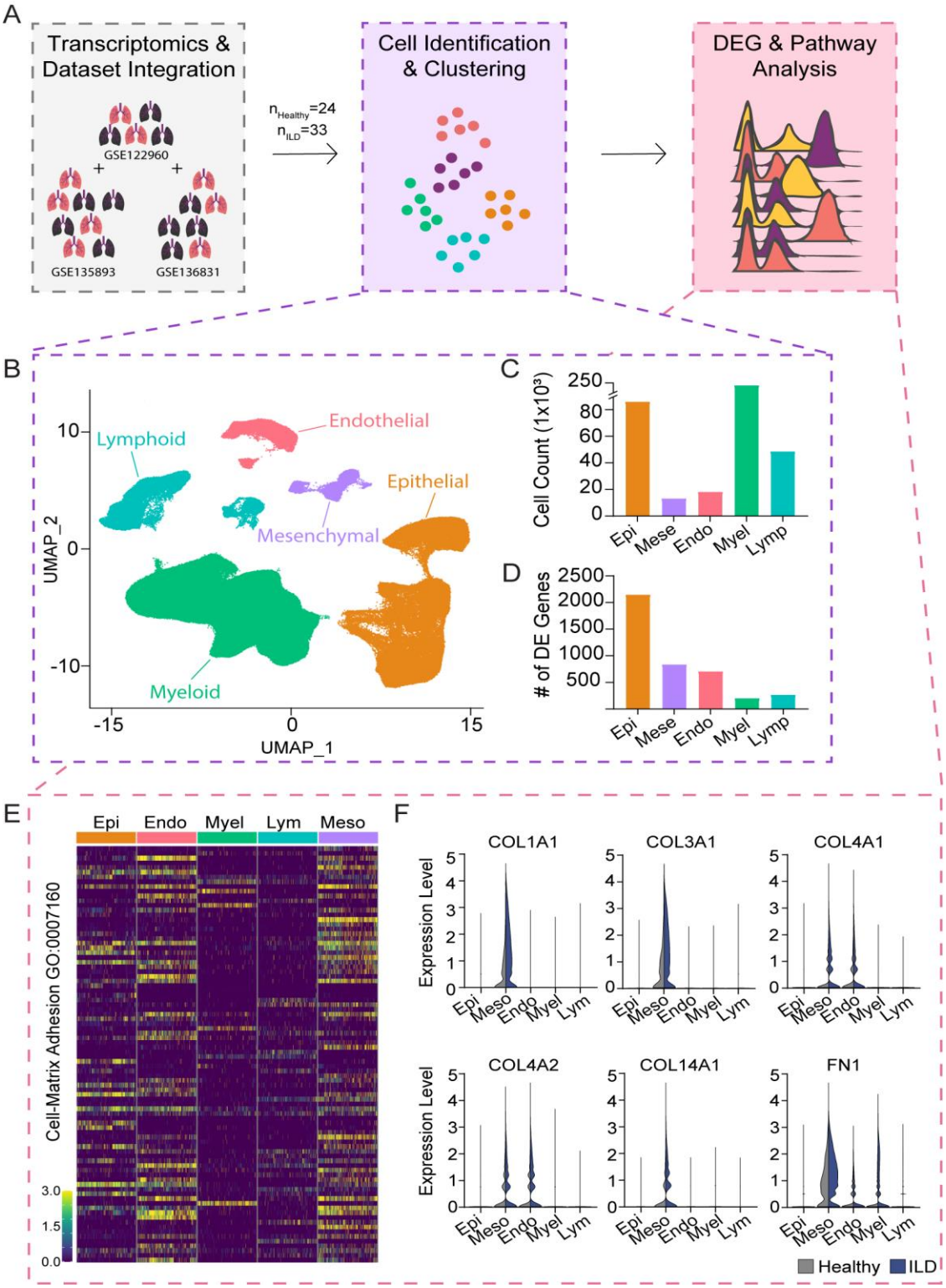

Figure 6.1: Integration and clustering of publicly available single-cell transcriptomics data. A) Schematic of data analysis workflow. B) UMAP plot of 5 major cell populations in the lung, with quantification of relative cell numbers (C) and the number of differentially expressed genes

(D). E) Heatmap of differentially expressed genes associated with cell-matrix adhesion, including violin plots of specific fibrosis-associated matrix proteins (F).

To explore stromal cell diversity in PF, we leveraged three publicly recently published datasets that conducted scRNA-seq on patients with and without pulmonary fibrosis. This included a cohort of 20 patients with various interstitial lung diseases (ILD, GSE135893), a cohort of 9 patients with ILD (GSE122960), and a cohort of 32 patients with IPF (GSE136831). As stromal cell yield from lung tissue isolates is relatively low compared to with immune and epithelial populations, we used an established referenced-based canonical correlation analysis (CCA) from the Seurat package to integrate available datasets **(Figure 6.1A)**. Firstly, low quality cells with either high percentages of mitochondrial RNA or low feature expression were removed, with ~380,000 cells remaining for analysis.

After integration, dimensionality reduction and unsupervised clustering identified 5 major pulmonary cell populations including cells of epithelial, lymphatic, myeloid, endothelial, and mesenchymal lineages **(Figure 6.1B)**. Notably, batch effects present prior to integration in Uniform Manifold Approximation and Projection (UMAP) embeddings were not evident after CCA implementation; GEO metadata from relevant datasets also confirmed accurate population labeling compared to a pre-integrated dataset (data not shown). As clinical datasets can be limited by limited patient numbers and cell yields, this analysis allowed us to explore stromal (i.e. endothelial and mesenchymal) lineages with a higher statistical confidence, with ~40,000 cells available for analysis **(Figure 6.1C)**. We then used a widely employed generalized linear model (MAST) to explore differential gene expression for each major pulmonary lineage via disease contrast (as a function of healthy or fibrotic donor source). While epithelial cells had the highest number of differentially expressed genes, we validated that endothelial and mesenchymal lineages possessed the highest levels of matrix-associated transcripts **(Figure 6.1D, E)**. This

included many key proteins associated with tissue repair including COL1A1, COL3A1, COL4A1, COL4A3, COL14A1 and FN1 **(Figure 6.1F)** and confirmed that endothelial and mesenchymal lineages are the likely cellular drivers of matrix deposition in PF.

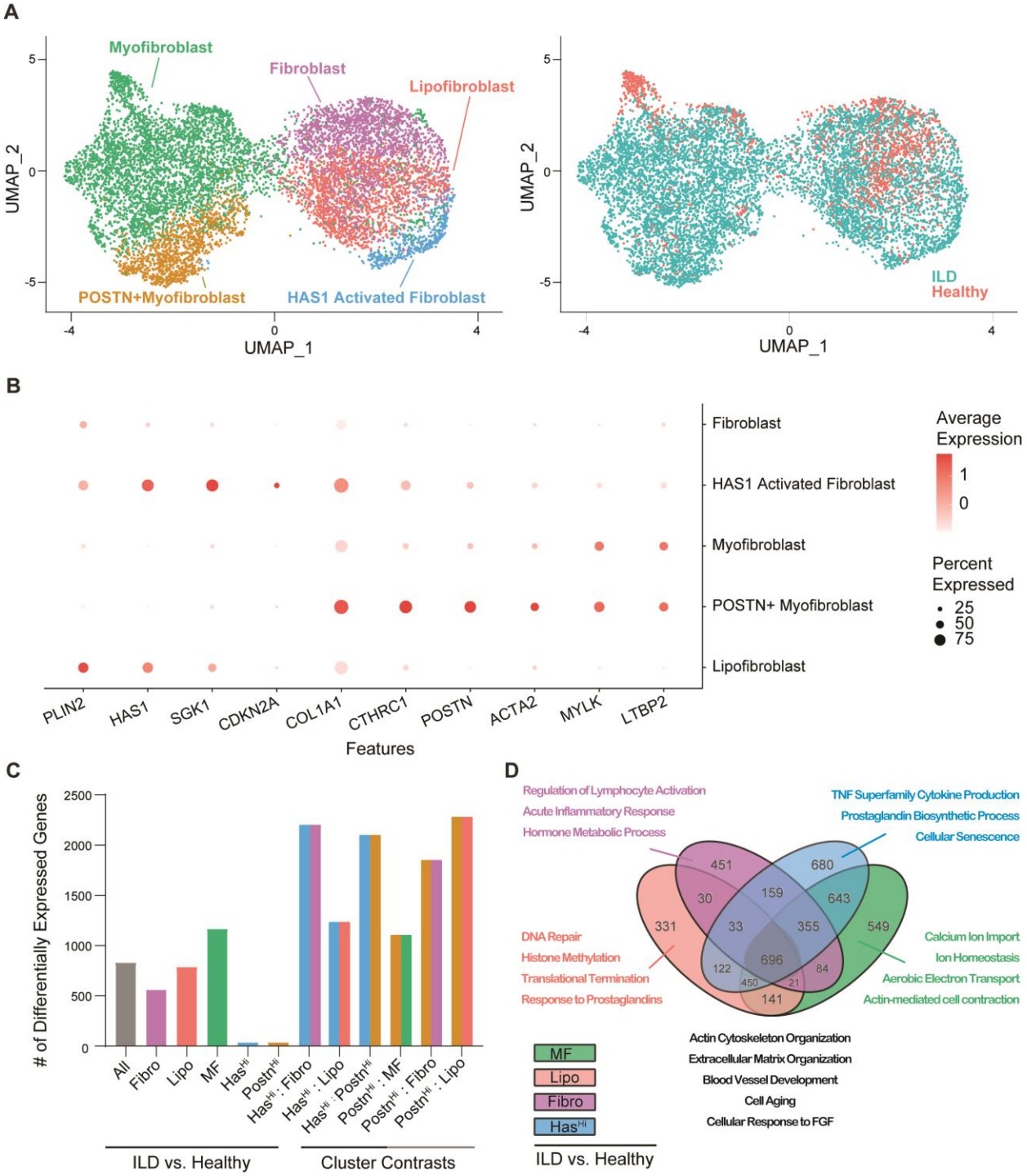

Figure 6.2: A detailed analysis of the fibroblast population within fibrotic lungs. A) UMAP plot of the 5 fibroblast subpopulations present in the lung (left) alongside a UMAP plot of cells

pseudo-colored by donor origin (right). B) Dotplot showing representative marker genes which define each subpopulation. C) Bar graph depicting differentially expressed genes as a function of disease contrast (ILD vs. healthy, left) or cluster-specific contrast (right). D) Venn diagram depicting differentially regulated pathways present in each fibroblast subpopulation, curated pathways with potential disease relevance are depicted via text.

We next conducted further unsupervised clustering on LUM+ lineage cells in an effort to develop a more comprehensive understanding of the matrix producing cells from the pulmonary mesenchyme. Using canonical markers, we identified 5 fibroblast subtypes alongside smooth muscle, pericyte, and mesothelial populations. Interestingly, while numerous murine and *in vitro* studies have focused on ACTA2+ myofibroblasts (MF) as the primary secretors of ECM in PF, we noted that ACTA2 was primarily expressed in smooth muscle cells lacking significant COL1A1 expression. As COL1A1 levels were comparably low in pericyte and mesothelial subtypes, we chose to focus on the fibroblast lineage for subsequent analysis.

We noted of 5 unique fibroblast subtypes including two MYLK+ MF lineages, one of which expressed ACTA2 alongside high levels of ECM-associated transcripts including POSTN and CTHRC1 **(Figure 6.2A)**. As MYLK is an important protein regulating cellular contraction, it is possible that these populations are partly responsible for the tissue stiffening that occurs in PF. Furthermore, CTHRC1+ cells were almost exclusively present in PF lungs **(Figure 6.2A, B)**. Interestingly, a CTHRC1+ population has been recently identified in fibrotic mice and may be analogous to the population explored here (Layton et al., n.d.; Tsukui et al., 2020). In addition, three MYLK- fibroblast populations were identified including interstitial fibroblasts, alveolar fibroblasts, and a recently identified HAS1+ population thought to expand from the lung pleura (Habermann et al., 2019). Interestingly, this HAS1+ population also expressed higher levels of COL1A1 and POSTN and was nearly absent in the lungs of healthy donors **(Figure 6.2B)**.

As the POSTN+ CTHRC1+ MF population has, to our knowledge, not been explored in the human lung, we sought to further characterize the phenotype of this potential subtype.

Conducting a differential expression analysis based on a cluster-specific contrast, we see that the POSTN+ MF population, while sharing some similarity to the POSTN- MF population, has ~1000 differentially expressed genes in comparison. Notably, a disease-based (comparing cells from fibrotic and healthy donors) contrast of the alveolar fibroblast compartment reveals only ~700 differentially regulated genes. Furthermore, while comparing via a disease-based contrast (cells from fibrotic vs. healthy donors) is not possible for this population due to the absence of POSTN+ cells in healthy lung, other cluster-specific contrasts suggest that the POSTN+ MF population is highly distinct from other fibroblast subpopulations **(Figure 6.2C)**. While exceptional recent work has discussed heterogeneity of non-contractile fibroblast subtypes (Habermann et al., 2019; McDonough et al., 2019), these results suggest that heterogeneity may also exist within the contractile MF compartment. Whether MFs exist on a continuum or in distinct lineages will have to be explored in future work.

As it is becoming increasingly appreciated that fibroblasts carry out a diverse set of functions beyond ECM maintenance, we next conducted a thorough characterization of each pulmonary fibroblast subpopulation. With the goal of reducing false positives, we utilized a prior knowledge based network analysis package (Advaita IPathwayGuide, (Draghici et al., 2020; Peyvandipour, Saberian, Shafi, Donato, & Draghici, 2018; Shafi, Nguyen, Peyvandipour, Draghici, & Kelso, 2020) to conduct a thorough analysis of pathways dysregulated within each subtype. For alveolar and interstitial fibroblasts we conducted the analysis via a simple disease-contrast, whereas the limited numbers of HAS1+ and POSTN+ MFs in healthy lungs made this type of comparison challenging. As many of the disease-specific changes present in the MYLK+ MF compartment were due to the appearance of the POSTN+ population, we conducted an aggregated analysis on all MYLK+ MF cells as a function of donor status. For the HAS1+

population we conducted a cluster specific contrast against the neighboring interstitial and alveolar fibroblasts. Interestingly, we noted some shared dysregulation of similar pathways across each fibroblast subtype, including pathways associated with the actin cytoskeleton, matrix deposition, and angiogenesis **(Figure 6.2D)**. Nevertheless, unique changes were observed in the various subtypes: the alveolar fibroblasts signature was indicative of a potential stress response with dysregulation of pathways associated with DNA repair and prostaglandin response, interstitial and HAS1+ fibroblasts may have dysregulated immunomodulation as evidenced by the upregulation of various inflammatory response pathways, with HAS1+ cells also exhibiting a senescent signature when compared to their alveolar and interstitial counterparts **(Figure 6.2D)**. In contrast, most of the pathway dysregulation within the MYLK+ MFs were not associated with inflammation and were instead associated with key mechanosensitive behaviors, namely matrix contraction and ion transport pathways **(Figure 6.2D)**. While the functional role of each fibroblast subtype in lung homeostasis has yet to be fully elucidated, these results suggest that each subpopulation may have a unique role in fibrotic pathology.

Using an analogous pipeline, we next sought to characterize the pulmonary endothelial cell compartment. Unsupervised clustering revealed 6 unique endothelial cell (EC) populations including lymphatic, arterial, capillary type 1, capillary type 2, venous, and POSTN+ venous population **(Figure 6.3A, B)**. Similar to the POSTN+ MF population, POSTN+ ECs appeared to be primarily present in fibrotic lungs. Interestingly, this POSTN+ population was recently identified and marked by the COL14A1 protein and may be present in terminal bronchioles at low levels within the healthy lung (Schupp et al., 2021). Neverthless, these cells appear to undergo a large expansion in PF and have a significantly altered gene expression profile compared to their POSTN- counterparts **(Figure 6.3C)**. Conducting a pathway analysis based on

a disease contrast, we next explored dysregulation of capillary, arterial, and venous (POSTN- and POSTN+) scale vasculature. Broadly, all ECs shared a similar dysregulation of pathways associated with angiogenesis, apoptosis, and aging. Of note, dysregulation of capillary EC

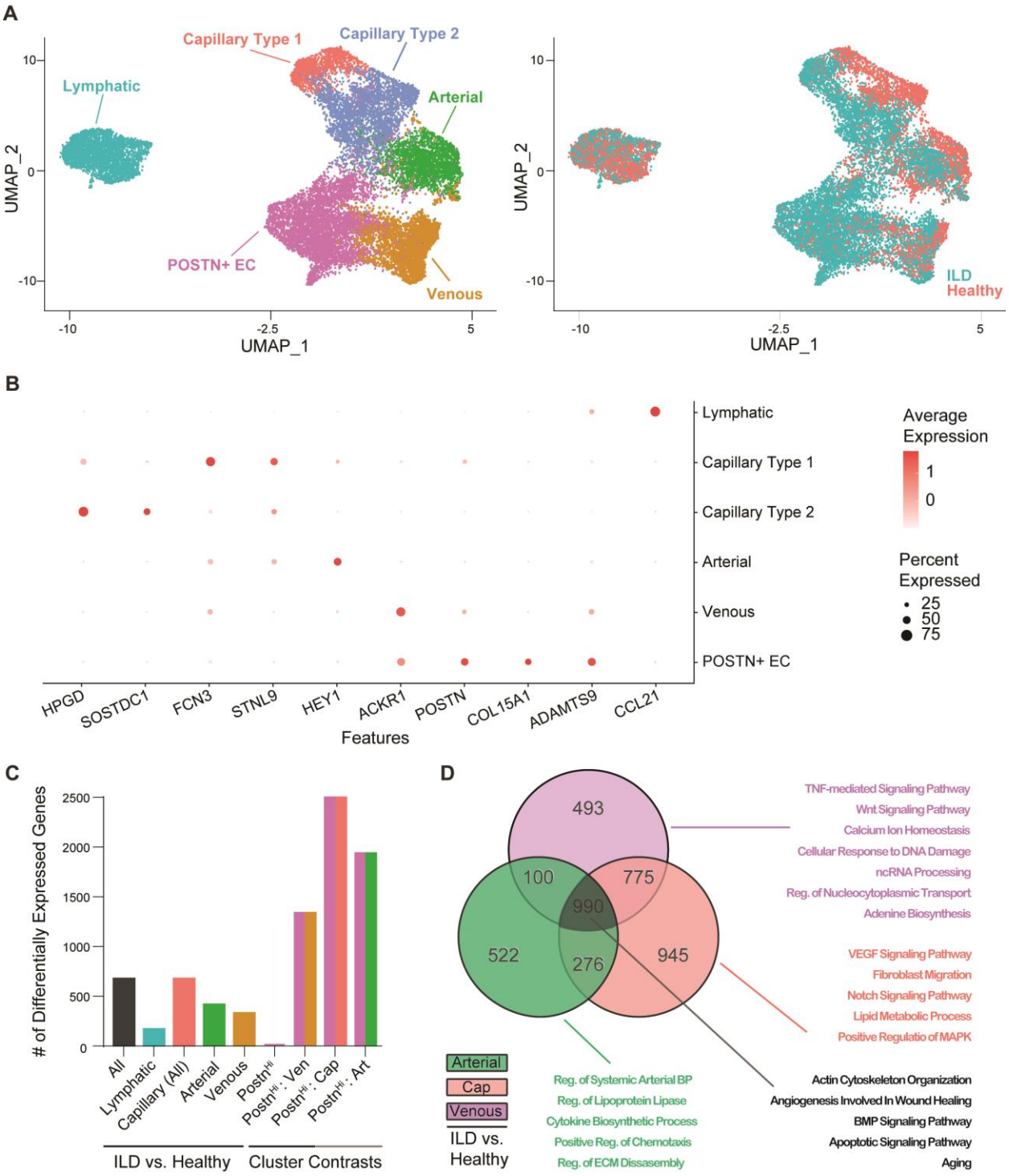

Figure 6.3: A detailed analysis of the endothelial population within fibrotic lungs. A) UMAP plot of the 6 endothelial subpopulations present in the lung (left) alongside a UMAP plot of cells pseudo-colored by donor origin (right). B) Dotplot showing representative marker genes which define each subpopulation. C) Bar graph depicting differentially expressed genes as a function of disease contrast (ILD vs. healthy, left) or cluster-specific contrast (right). D) Venn diagram depicting differentially regulated pathways present in each endothelial subpopulation, curated pathways with potential disease relevance are depicted via text.

phenotype appeared to be related to many common tissue repair pathways, namely VEGF and NOTCH signaling as well as fibroblast migration pathways. In contrast, dysregulation of arterial ECs primarily involved vascular tone and ECM remodeling, potentially in line with the clinical observation of pulmonary hypertension in PF (Colombat et al., 2007; Schraufnagel, Mehta, Harshbarger, Treviranus, & Wang, 1986). Finally, venous ECs appeared to exhibit a stress response signature with DNA damage and TNF signaling pathways dysregulated in fibrosis patients. Indeed, while ECs are infrequently discussed in terms of their contribution to fibrotic disease, these results suggest that each EC subtype likely posseses a unique function in the context of fibrotic lung.

While the above analyses revealed many phenotypic differences within the fibroblast and EC compartments, we noticed that the three abundant celltypes overrepresented in the lungs of pulmonary fibrosis patients (HAS+ fibroblasts, POSTN+ MFs, POSTN+ ECs) all uniquely expressed the POSTN protein and may be converging toward a similar fibrosis-associated phenotype. Logically, we next conducted a cluster-based pathway analysis to explore how these unique cell populations are distinct from there POSTN- counterparts. Results indicated that while each POSTN+ population exhibits a unique transcriptional phenotype, ~65% of dysregulated pathways are shared across each population **(Figure 6.4A)**. Approximitely half of these pathways involve other pathologies that exhibit fibrotic and inflammatory components such as cancer and lung-specific infectious diseases. Remaining shared pathways included well-

established fibrosis-associated pathways (i.e TGF-b1 and matrix-associated signaling), essential second messengers and signal transducers (i.e. cAMP, cGMP, phosphatidic acid, and NF-KB) and emerging pathways that may regulate tissue repair in heath and disease.

More specifically, an overlapping transcriptional signature of dysregulated endocrine (i.e. aldosterone, renin, estrogen, parathyroid hormone, oxytocin) and paracrine (i.e. EGF, IL-17, Wnt, VEGF, BMP, and TNF) factors indicate a convergence of fibrotic signaling in stromal cell populations **(Figure 6.4B)**. As many of these factors have been recently identified to promote fibrosis-associated pathology in murine models, future work should explore how these ligands specifically effect EC and fibroblast populations. Notably, the renin-angiotensin and cAMP pathways are being increasingly explored as targets for therapuetic intervention in PF. Future work should methodologically examine how these pathways impact overall disease course and the presence of POSTN+ stromal cells in the lung. Importantly, whether the accumlation of POSTN+ stromal cells contributes to fibrosis progression or is simply an indicator of aberrant tissue repair remains to be elucidated.

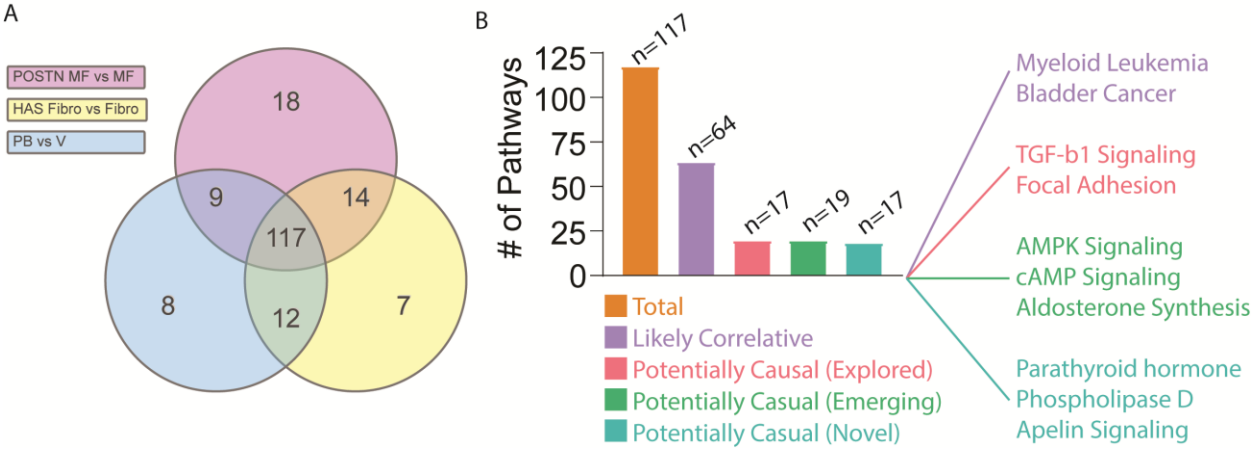

Figure 6.4: Analysis of the stromal-cell signaling axis present in fibrotic lungs. A) Venn diagram depicting overlap of dysregulated pathways present in POSTN+ MFs, POSTN+ ECs, and Has1+ fibroblasts. B) Bar graph characterizing the types of pathways dysregulated in all subpopulations; text depicts examples of each pathway type.

As tracking multiple different POSTN+ celltypes *in vivo* remains particularly challenging, one developing avenue for interrogating human pathology is the use of tissue-specific bioengineered models. Unfortunately, whether common *in vitro* models contain heterogeneity that recapitulates human disease has been almost entirely unexplored. Such unknowns motivated us to conduct scRNA-seq on a recently established 3D model of PF (Matera et al., 2020) that partially recapitulates aspects of disease progression (MF accumulation, tissue stiffening, matrix deposition). This model utilizes a combination of physical (high fiber densities reminscent of fibrotic lung architecture) and soluble (TGF-β1) cues to induce MF differentiation in primary lung fibroblasts. Control conditions included a lower fiber density reminscent of a healthy lung interstitia. In addition, we included a standard 2D TGF-β1-mediated assay widely used for theraputeic screening and basic science applications (Peela et al., 2017).

After 9 days of 2D or 3D culture, primary lung fibroblasts were isolated from control and fibrotic conditions and subject to scRNA-seq using the 10x Genomics platform. After filtering low quality cells, unsupervised clustering on ~50,000 fibroblasts revealed the existence of 13 unique subpopulations *in vitro* as marked by unique marker expression **(Figure 6.5A, B)**. Interestingly, despite analagous donor and media conditions, 2D and 3D culture yielded distinct transcriptional signatures with minimal overlap **(Figure 6.5A)**. These results corroberate signficant evidence from the extant literature emphasizing a key role for the physical microenvrionment in regulating cell fate (Davidson et al., 2019; Engler et al., 2006). Furthermore, a phenotypic shift was noted as both cluster 0 (2D) and cluster 1 (3D) expanded greatly in fibrotic conditions containing TGF-β1 (2D) or TGF-β1 and high fiber density (3D), respectively. Notably, cluster 0 and cluster 1 exhbit increased expression of COL1A1, POSTN, and ACTA2, indicating a MF-associated phenotype (data not shown).

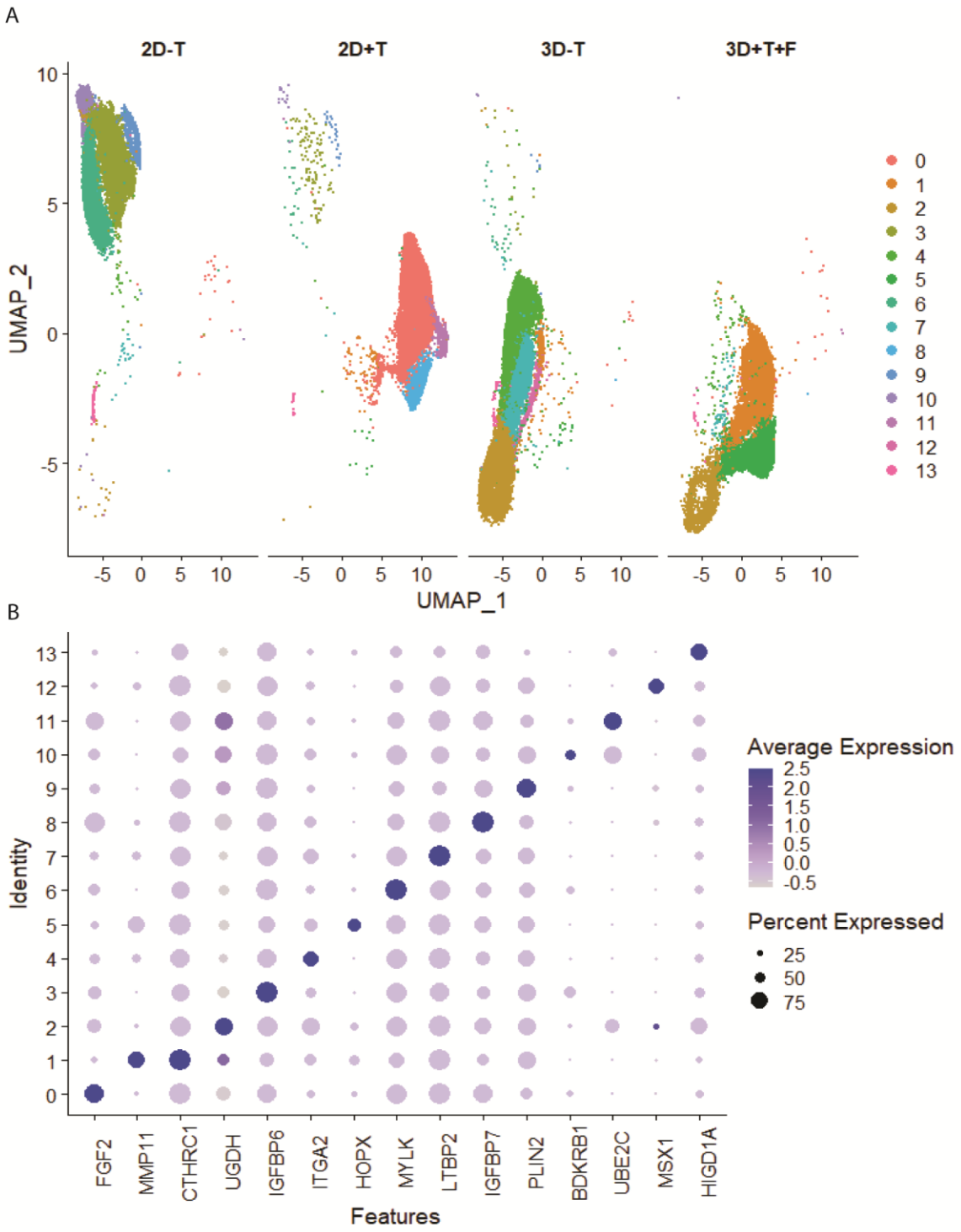

Figure 6.5: scRNA-seq analysis of a bioengineered model of fibrosis. A) UMAP plot depicting various subpopulations present in each condition. B) Dotplot depicting marker genes present in each of the 13 subpopulation clusters.

As cluster 1 exhibited the CTHRC1 and MMP11 markers which were uniquely expressed in the POSTN+ MF population from PF lungs **(Figure 6.6A)**, we next explored the similarity

between these two populations. Conducting a transcriptome-wide analysis of expressed genes within 1) POSTN+ fibroblasts from patient lung and 2) CTHRC1+ cells derived from either 2D or 3D culture revealed that ~45% of genes (1894 unique transcripts) were shared between all three populations, with 3D fibroblast isolates exhibiting a slightly higher similarity

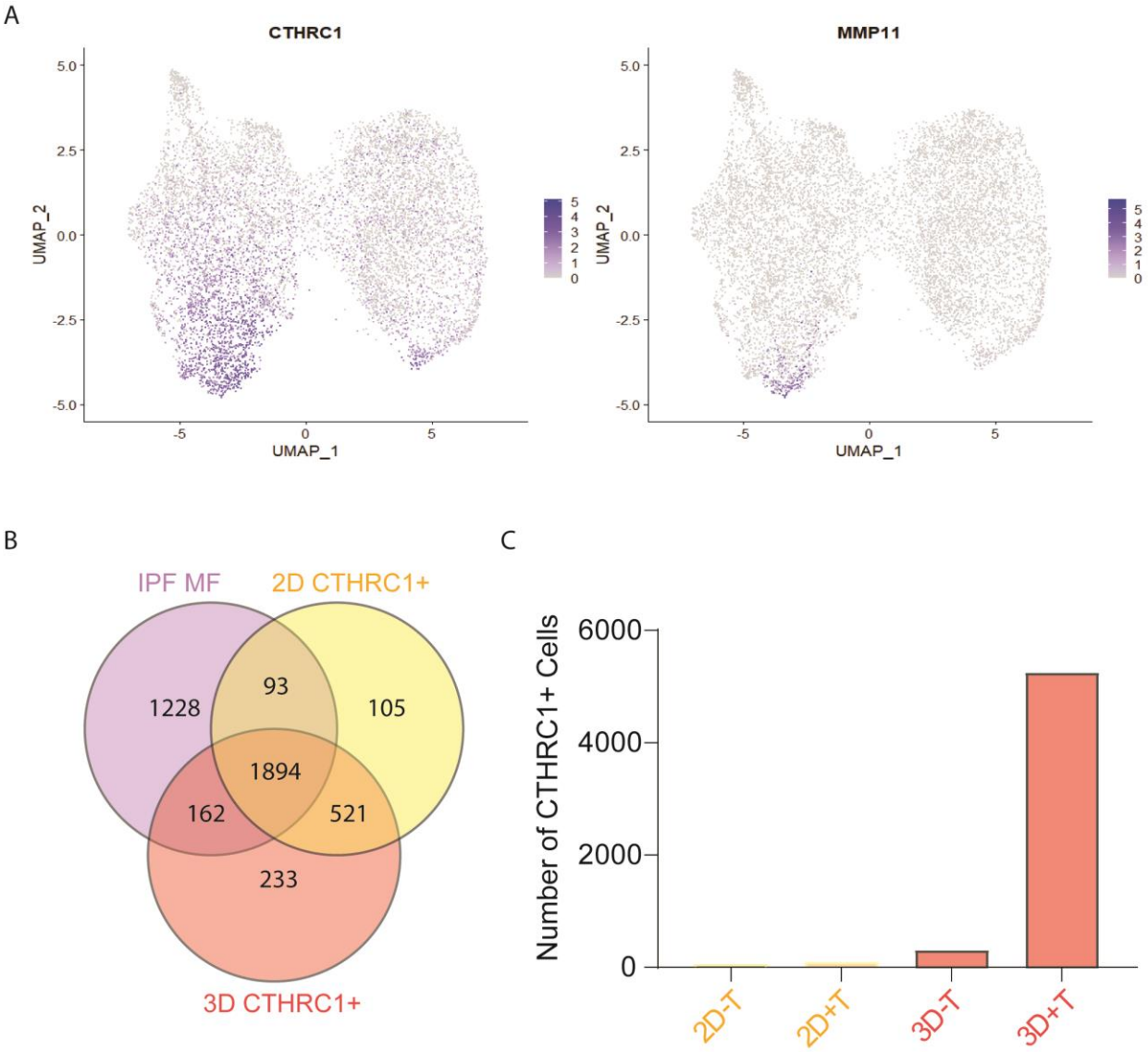

Figure 6.6: Comparison of POSTN+ MFs derived from patient transcriptomics data to a MF-associated cluster present in the bioengineered PF model. A) UMAP plot of patient fibroblasts pseudo-colored by CTHRC1 and MMP11 expression. B) Venn diagram depicting overlap of expressed genes between patient derived POSTN+ MFs and MFs derived from a standard 2D and 3D bioengineered PF model.

(an additional 162 unique transcripts) compared to patient cells **(Figure 6.6A)**. Furthermore, while the CTHRC1+ cells from 2D isolates were relatively similar to their 3D counterparts, only ~2% of the 2D population were CTHRC1+ **(Figure 6.6B)**. In contrast, a majority (~70%) of cells isolated from fibrotic 3D conditions exhibited CTHRC1 positvity **(Figure 6.6B)**. To our knowledge, this work was the first study to explore cell heterogenity within *in vitro* fibrosis models and confirms that primary cells exist as a heterogenous population *in vitro*. Furthermore, we show that exposure to a physical (high fiber density) and soluble (TGF-B1) fibrotic cue can push fibroblast populations toward a phenotype more reminscent of cells found within PF lungs. Future work should methodologically explore each subpopulation and their specific relevance to patient counterparts.

In summary, we utilized a combination of patient transcriptomics data and 2D and 3D models to explore stromal cell heterogenity in the context of pulmonary fibrosis. Results indicated that patient stromal cells exhibit a vast heterogenity and a converging fibrotic phenotype that should be exploited 1) for enhanced pathophysiological understanding and 2) for the evaluation of new therapuetic targets. While invaluable, patient studies posses significant ethical and logistical considerations which hinder their ability to confirm many findings that are, paradoxally, derived from patient data. Such limitations motivate the use of murine models and *in vitro* models of fibrosis, the latter of which will be critical due to their ability to capture human-specific biology. Importantly, a thorough understanding of the relevance of *in vitro* models to the clinic will be required for the translation of these technologies; this work also serves as a seminal characterization of well-established (2D) and emerging (3D) *in vitro* models of PF. We show that while fibroblast heterogenity exists within *in vitro* PF models, a significant transcriptional discordance exists between current modeling technologies and patient biology.

Nevertheless, 3D bioengineered models appear to exhibit a greater degree of transcriptional biomimicry when compared to their 2D counterparts. These data suggest that physical and soluble cues can guide enhanced transcriptional relevance and motivate the continued development of bioengineered platforms. Future work should explore 1) the relevance of the CTHRC1- fibroblast populations present within *in vitro* fibrosis models and 2) explore how the the incorporation of additional plumonary celltypes and soluble factors affect fibroblast phenotype.

6.5 Materials and Methods

6.5.1 Reagents

All reagents were purchased from Sigma Aldrich and used as received, unless otherwise stated.

6.5.2 Synthesis and Fabrication

Dextran vinyl sulfone (DexVS) was synthesized using a previously established protocol for vinyl sulfonating polysaccharides adapted for use with high MW dextran (MW 86,000 Da, MP Biomedicals, Santa Ana, CA) (Davidson et al., 2020; Matera et al., 2019). Briefly, pure divinyl sulfone (12.5 ml, Fisher Scientific, Hampton, NH) was added to a sodium hydroxide solution (0.1 M, 250 mL) containing dextran (5 g). This reaction was carried out at 1500 RPM for 3.5 minutes, after which the reaction was terminated by adjusting the pH to 5.0 via the addition of hydrochloric acid. A lower functionalization of DexVS was utilized for hydrogels, where the volume of divinyl sulfone reagent was reduced to 3.875 ml. All reaction products were dialyzed for 5 days against Milli-Q ultrapure water, with two water exchanges daily, and then lyophilized for 3 days to obtain the pure product. Functionalization of DexVS was characterized by ^{1}H –NMR spectroscopy in

D_2O and was calculated as the ratio of the proton integral (6.91 ppm) and the anomeric proton of the glucopyranosyl ring (5.166 and 4.923 ppm), here a vinyl sulfone/dextran repeat unit ratio of 0.376 and 0.156 was determined for electrospinning and hydrogel DexVS polymers, respectively.

For fiber fabrication, DexVS was dissolved at 0.6 g ml^{-1} in a 1:1 mixture of Milli-Q ultrapure water and dimethylformamide with 0.015% Irgacure 2959 photoinitiator. Methacrylated rhodamine (0.5 mM; Polysciences, Inc., Warrington, PA) was incorporated into the electrospinning solution to fluorescently visualize fibers. This polymer solution was utilized for electrospinning within an environment-controlled glovebox held at 21 ˚C and 30% relative humidity. Electrospinning was performed at a flow rate of 0.3 ml h^{-1}, gap distance of 5 cm, and voltage of -10.0 kV onto a grounded collecting surface attached to a linear actuator. Fiber layers were collected on glass slabs and primary crosslinked under ultraviolet light (100mW cm^{-2}) and then secondary crosslinked (100 mW cm^{-2}) in a 1mg mL^{-1} Irgacure 2959 solution. After polymerization, fiber segments were resuspended in a known volume of PBS (typically 3 ml). The total volume of fibers was then calculated via a conservation of volume equation: total resulting solution volume = volume of fibers + volume of PBS (3 ml). After calculating total fiber volume, solutions were re-centrifuged, supernatant was removed, and fiber pellets were resuspended to create a 10 vol% fiber solution, which were then aliquoted and stored at 4^o C. To support cell adhesion, 2.0 mM RGD (CGRGDS, 2.0 mM, Genscript, George Town, KY), was coupled to vinyl sulfone groups along the DexVS backbone via Michael-type addition chemistry for 30 min, followed by quenching of excess VS groups in a 300 mM cysteine solution for 30 minutes. To remove free thiols after quenching, fiber solutions were vigorously rinsed via flushing with excess PBS three times before use in cell studies.

For hydrogel formation, DexVS gels were formed via a thiol-ene click reaction at 3.3% w/v (pH 7.4, 37°C, 45 min) with VPMS crosslinker (12.5mM) (GCRDVPMSMRGGDRCG, Genscript, George Town, KY) in the presence of heparin-binding peptide (HBP, GCGAFAKLAARLYRKA, 0.65 mM, Genscript, George Town, KY), and fiber segments (0.0-2.5% v/v). Cysteine was added to precursor solutions to maintain a final vinyl sulfone concentration of 60 mM after gelation. All hydrogel and peptide precursor solutions were made in PBS containing 50 mM HEPES. To create fibrous hydrogels, a defined stock solution (10% v/v) of suspended fibers in PBS/HEPES was mixed into hydrogel precursor solutions prior to gelation. Via controlling the dilution of the fiber suspension, fiber density was readily tuned within the hydrogel at a constant hydrogel weight percentage. For gel contraction experiments, DexVS was polymerized within a gelatin-coated 5 mm diameter PDMS gasket to ensure consistent hydrogel area beginning on day 0.

For single-cell isolation during scRNA-seq experiments, hydrogels were washed in ~3 ml of PBS on a rocker plate for 15 minutes. Hydrogels were then incubated in a 1ml solution of ice-cold Accutase containing 50 ul of dextranase (4000IU, Cellendes Technologies, UK) and 30uM EGTA for 20 minutes on a rocker plate at 37C. After 20 minutes, hydrogel solutions were gently pipetted with a 1000ml pipette and 100ul of Liberase (2.5mg/ml, Sigma) was added, mixed, and solutions were returned to the rocker plate. After 10 additional minutes, solutions were gently pipetted for ~30 seconds and transferred to 15 ml conical tubes with ~13ml of DMEM. For 2D cell isolation, cultures were washed and left in accutase/EGTA for 20 minutes, followed by 10 minutes of treatment with .05% T/E solution. Solutions were centrifuged at 500G for 2 minutes and resulting cell pellets were resuspended in 200 ul of DMEM and passed through a 30 micron cell strainer and left on ice until sequencing was conducted.

6.5.3 Cell Culture and Biological Reagents

Normal human lung fibroblasts (University of Michigan Central Biorepository were cultured in DMEM containing 1% penicillin/streptomycin, L-glutamine and 10% fetal bovine serum (Atlanta biologics, Flowery Branch, GA). Cells were passaged upon achieving 90% confluency at a 1:4 ratio and used for studies until passage 7. For all hydrogel studies, cells were detached with 0.05% trypsin-EDTA (Life Technologies), counted and either encapsulated into or seeded onto 12.5 µl hydrogels at a density of 1,000,000 cells ml^{-1} of hydrogel, and subsequently cultured at 37°C and 5% CO2 in serum containing medium. For 2D studies of cell morphology F-actin organization (Supplementary **Figure** 1), the total number of cells seeded onto each 12 mm glass coverslip was equivalent to 12.5ul hydrogels described above. Media was refreshed the day after encapsulation and every 2 days after. In differentiation experiments, recombinant human TGF- β1 (Peprotech, Rocky Hill, NJ) was supplemented to media at 5 ng ml.

6.5.4 RNA-Sequencing and Bioinformatics

For *in vitro* model sequencing, two primary lung donors were used for each culture condition. Per sample, 10,000 cells were pooled from three technical replicates and sequenced at a depth of 30,000 reads/cell via the 3' 10X Genomics platform. Raw sequencing data was processed (transcript mapping, read quantification, alignment) via the CellRanger AGGR pipeline. For unsupervised clustering and downstream analysis, the R package Seurat was used via standard methodologies (Hafemeister & Satija, 2019; Stuart et al., 2019). Following the remove of low quality cells (>10% MT gene expression, <1000 features/cell), data normalization for clustering was conducted via SCTransform to minimize batch effects. CCA-based normalization was conducted for the integration of publicly available datasets (Stuart et al., 2019). Dimensionality reduction, clustering, and visualization were then conducted via standard

approaches. Cluster identification was conducted via unsupervised clustering and validated via a combination of known markers and differential expression between clusters, with <1000 differentially expressed genes/cluster being used as a threshold for overclustering. Differential expression analysis was conducted via the MAST package and dataset origin was used as a latent variable for the patient-based integrated datasets. Differentially expressed genes were defined as genes with a LogFC > .25 and with an adjusted p-value < .05. Pathway analysis were conducted via the IPathwayGuide impact analysis software (Advaita Biotechnologies, MI).

Chapter 7: A Commentary: New Directions and Dimensions for Bioengineered Models of Fibrosis

7.1 Authors

Daniel L. Matera, William Y. Wang, Brendon M. Baker

7.2 Introduction

During fibrotic diseases, functional tissue parenchyma progressively transforms into stiff, disorganized and non-functional tissue causing organ failure. The underlying multitude of interconnected changes in the cellular microenvironment can be investigated using bioengineered fibrosis models.

7.3 Background

Fibrosis is the process of dysregulated wound healing and underlies numerous diseases from cancer to cardiac disease and pulmonary fibrosis. Despite its ubiquity in disease, the diversity and complexity of this process studied *in vivo* has hindered pathophysiological understanding. As a result, the use of *in vitro* culture models has helped elucidate the role of numerous microenvironmental cues and signaling pathways contributing to the differentiation of myofibroblasts (MF). However, recent single-cell transcriptomic studies have raised new

questions about the identities and signaling of cells contributing to fibrosis. Here, we comment on recent developments in bioengineered disease models that may address outstanding challenges in fibrosis research.

7.4 Biomaterials: From 2D to 4D

Early insights into MF biology surprisingly originate from cell culture studies in 3D settings; observations that embedded fibroblasts contract type I collagen matrices confirmed their role as force-generating cellular drivers of wound closure. The use of this simplified tissue model to screen soluble factors established the pro-contractile effects of TGF- β, a family of cytokines and associated signaling pathways now accepted as major effectors of organ fibrosis. While foundational, inherent limitations of natural biopolymers (i.e. limited range and orthogonality of tunable properties and rapid degradability) motivated the use of synthetic polymeric materials as tunable culture substrates. Due to their elegance and ease of use, engineered 2D elastomer and hydrogel-based substrates have subsequently guided our understanding of how fibroblast-extracellular matrix (ECM) interaction drives fibrogenesis. Studies using these models illuminated the effect of cell spreading and morphology on proliferative signaling, the importance of Rho GTPases in cytoskeletal and focal adhesion assembly and signaling during matrix mechanosensing, and the link between matrix stiffness and MF differentiation, among many other important findings. This progress cemented the utility of materials-based approaches for studying cell biology, with the caveat that reductionist models capture singular key inputs or steps in a disease process, but likely fail to recapitulate the complexity and dynamics of actual disease.

Matrix stiffness modeled by plating cells on 2D substrates with tunable elasticity has emerged as an important physical cue that regulates fibrogenic signaling. The signaling induced

by stiff 2D substrates likely captures some key aspects of MF biology and suggests a feed-forward mechanism in fibrosis. However, questions remain regarding the initial appearance of MFs and the existence of mechanical thresholds that differentiate between reversion to healthy states versus continued fibrosis. Importantly, we should avoid distilling the complexity of tissue mechanics (further accentuated at the scale of the cell) into a single mechanical property such as a Young's modulus despite the appeal of simplicity. Recent work indicates significant heterogeneity and non-linear mechanical behavior that spatiotemporally evolves with lung fibrosis. New materials with more complex yet dynamically controllable mechanical behavior, including tunable viscoelasticity, nonlinearity, and plasticity, will help provide new insights into how mechanical behaviors of tissues beyond elasticity influence fibrogenesis as well as reversion to healthy states (Box 1). Beyond new materials, characterization methods that can map the mechanical properties of biomaterials and tissues at the cell-scale in combination with improved measurements for traction forces in non-continuum and non-elastic settings are both desperately needed **(Figure 7.1)**.

Beyond possessing simpler mechanical behavior than native tissues, elastic 2D culture surfaces lack tissue-relevant structure, topography, and the potential to be remodeled and reorganized by constituent cells. In contrast, fibrogenic ECM presents complex and dynamic microenvironmental cues reciprocally to constituent cells: the evolving composite of gel-like proteoglycans and intermingled fibrous proteins modulates cell-adhesive ligand accessibility, viscoelastic and non-linear mechanical properties, and myriad diffusive or matrix-bound signaling molecules secreted by diverse cell types. These signals converge on fibroblasts as well as numerous other cell types, whether resident or recruited to the tissue. Interactions between cells and the ECM and between different cell types (heterocellular) drive matrix remodeling and

fibrotic changes at the tissue level, including destruction of parenchyma, altered tissue-scale mechanics, and disrupted organ homeostasis and function **(Figure 7.1)**. Although understudied, heterocellular interactions are likely mediated by mechanical properties of the ECM. Material systems that enable on-demand control of cell-driven remodeling and/or intercellular communication in combination with metabolic and molecular reporters **(Figure 7.1)** will help to decipher these complex dynamic interactions.

Given the inherent 3D architecture of connective tissue spaces where fibrosis originates and the notion that 3D culture elicits a more physiologically representative cell state, it is hard to imagine a route forward without returning to 3D settings. Our recent efforts to translate the relationship between matrix stiffness and MF differentiation to 3D settings (where matrix degradability and proteolytic remodeling are operative) suggests additional complexity must be considered. We found an enhanced capacity for MF differentiation when fibroblasts were embedded within soft (E = ~500 Pa) hydrogels that proved non-permissive to MF differentiation when cells were plated on top in 2D. Conversely, MF differentiation did not occur when fibroblasts were embedded within stiffer hydrogels possessing a Young's modulus of fibrosed lung tissue. Acknowledging the co-dependence of elasticity and degradable crosslink density of 3D polymeric hydrogels, we adopted a composite materials approach to decouple cell-scale mechanics from that of the bulk hydrogel cells are embedded within. By recapitulating the two-phase (gel-like proteoglycan and matrix fiber) composition of interstitial ECM, we established a model of fibrotic lung interstitium and found that matrix fiber density, not bulk hydrogel elastic modulus, promoted 3D MF differentiation via a mechanism heavily dependent upon dynamic MMP-mediated remodeling. These studies motivate continued development of 1) 3D ECM-mimetic models with tissue-relevant architecture and degradative/remodeling properties and 2)

new strategies to dissect the entwined relationship between cell-driven remodeling, matrix structure, and resultant cell and tissue mechanics.

Cell-driven remodeling in patients and animal models manifests as fibrosis after months to years, thus an additional key design feature for relevant biomaterial models is stability across long-term culture. Cell-degradable yet hydrolytically stable materials allowed us to investigate the role of matrix structure on fibrotic events downstream of MF differentiation (e.g. tissue contraction, matrix deposition, and stiffening) weeks after cell encapsulation. Although to present there has been an overemphasis on MF differentiation, 4D models will allow for investigating subsequent pathways that underlie matrix remodeling after differentiation. Understanding the actual MF functions that drive tissue/organ failure will be critical to both pathophysiological understanding and the development of next-generation therapies.

7.5 Cell Biology: From Monoculture to Microphysiology

Advances in biomaterial design have helped elucidate cell-matrix interactions that regulate MF differentiation in monoculture, but the involvement of other structural cells (e.g. endothelium, pericytes) and immune cells in fibrosis remains less understood. Partly due to the challenge of dissecting intercellular communication *in vivo*, much of our current understanding has been garnered from 2D co-culture, transwell assays, or mixed cell populations dispersed within 3D hydrogels. These assays fail to faithfully recapitulate the compartmentalization of most tissues, which contain parenchyma, vasculature, and the interstitia where fibroblasts reside. As such, these models fail to capture critical soluble, insoluble, and mechanical crosstalk between immune, structural, and parenchymal cells, all of which can be mediated by the ECM. The recent advent of microphysiologic or tissue-chip models provides an exciting opportunity to

recapitulate critical tissue-relevant organization of different cellular components, especially when integrated with biomaterial approaches described above. As many synthetic hydrogels tend to swell with equilibrium hydration, strategies to control swelling are critical to fluidically interfacing with tissue chip platforms and needed for high fidelity molding of channels or compartments within hydrogels. The repertoire of tissue-chips now covers most major organs that undergo fibrosis; integrative models capturing fibrotic changes surrounding tissue-specific structures can enable assessment of tissue function decline due to fibrotic changes, or conversely, improvement upon resolution. Furthermore, tissue chip models sufficiently scaled to meet standards for high throughput drug screening would also provide much needed functional assays superior to current 2D monoculture assays used in industry.

Given their consistent presence in all fibrosis-susceptible tissues, a fundamental question that remains to be answered is whether endothelial cells (ECs) and the angiogenic response promotes or mitigates fibrosis. The importance of the microvasculature in maintaining tissue homeostasis and the established requirement for angiogenesis in wound healing would suggest a beneficial contribution from ECs, yet the recent FDA approval of an angiogenesis inhibitor (nintedanib) for the treatment of lung fibrosis suggests otherwise. In mouse models of lung and liver fibrosis, signaling of ECs has been identified to play a critical role in both fibrotic progression and tissue regeneration and the process of endothelial-to-mesenchymal transition has been associated with angiogenesis, but also can provide a source of MF-like cells in mouse models of cancer, cardiac, liver, and kidney fibrosis. More recently, crosstalk between aberrant mesenchymal ECs and tubular epithelial cells has been shown to promote kidney fibrosis.

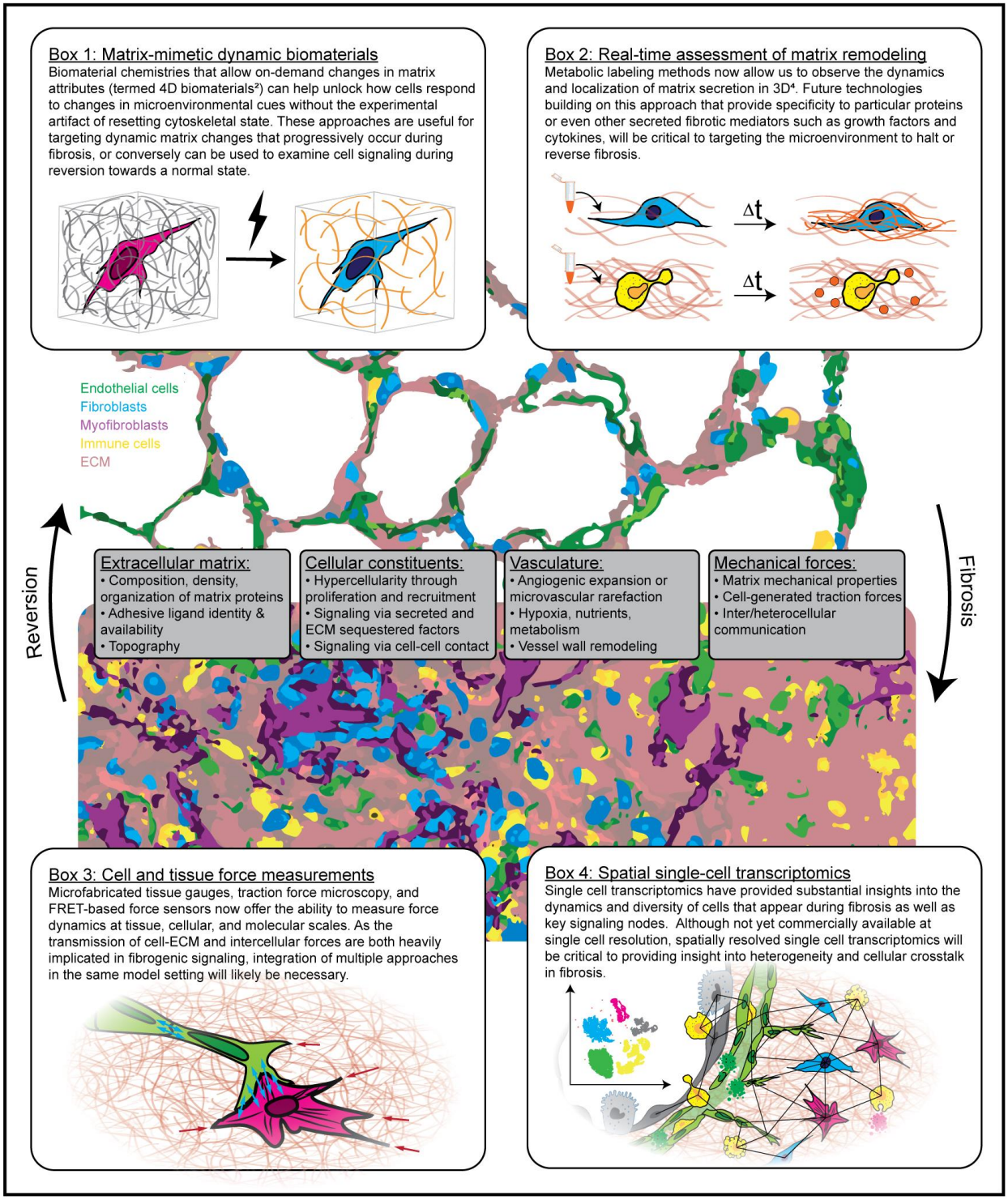

Figure 7.1: In fibrosis, organized and functional parenchyma is progressively transformed into stiffer, disorganized and non-functional tissue. Multiple, interrelated changes in the extracellular matrix (ECM), cells, vasculature and tissue mechanics are associated with fibrosis. Understanding the dynamic and reciprocal relationships between cells and their microenvironment requires advanced technologies and materials.

Consistent mechanisms of EC involvement in fibrosis across organ systems may be unlikely given that the microvascular response to injury is also heterogeneous by organ and insult; for example, the liver undergoes excessive angiogenesis during fibrosis, but regression or rarefaction are observed in the case of the lung or kidney. The implications of these observations are two-fold: 1) they highlight the intrinsic difference across tissues and emphasize the need for tissue-specific modeling; and 2) they suggest that the role of the microvasculature in fibrosis requires further study. Indeed, how MFs modulate tissue microvasculature (or vice versa) remains an open question. The integration of recently developed vessel-on-a-chip platforms and synthetic hydrogel chemistries offer a path to investigate heterotypic cell interactions at long time-scales and with high resolution. Such efforts will not only shed light on the nuanced and divergent roles ECs play in fibrosis, but will also serve as a roadmap for the development of more advanced fibrosis-on-a-chip platforms; similar investigations integrating tissue-specific parenchymal cells will be an essential next step.

7.6 Outlook: Complexity with Purpose

Spanning materials science and cell biology, bioengineers are developing new biomimetic models to bring increasingly complex questions within reach. In these endeavors, the biology of interest should take center-stage – materials that test biologically motivated hypotheses, rather than materials developed for the sake of novelty, will be essential if bioengineers want to make a meaningful impact for patients. Bearing in mind that “all models are wrong, but some are useful” (George E.P. Box), we should ensure our work contributes to a clear objective, whether that be the pursuit of fundamental biological understanding or the development of efficacious therapies.

Chapter 8: Summary and Future Directions

8.1 Summary

Overall, this thesis aimed to explore PF via the engineering of synthetic fibrous matrices that mimic the extracellular environment present in healthy and diseased lung. Chapter 2 served to provide a background into the clinical pathology of PF and the various cellular and extracellular factors at play within the fibrotic microenvironment. Additionally, Chapter 2 served to present the current modeling paradigms employed during fibrosis research. The information presented in Chapter 2 serves as a brief background to concepts discussed in detail within the introduction sections of subsequent chapters.

Chapter 3 examined the architecture of interstitial extracellular matrix and discussed the relative advantages and disadvantages of current models. This chapter also explored the engineering of a novel bioengineered model of interstitial ECM. With the goal of studying fibroblast biology in PF, Chapters 4-5 worked to adapt this bioengineered model toward use as lung biomimetic. In addition to advancing model complexity, these chapters established one of the first 3D mechanisms for MF differentiation; briefly, matrix fibers induce local RhoA and Rac1 activity in fibroblasts and work together to drive their activation toward MFs in an MMP-dependent manner. Finally, these chapters established a new platform for 1) the investigation of MF biology and 2) the screening of anti-fibrotic compounds.

Using scRNA-seq, Chapters 6 served as a detailed characterization of fibroblasts and other stromal cells within clinical PF as well as within a bioengineered model of fibrotic ECM. This work documented a convergent signaling axis among stromal cells in PF and discussed the relevance of a major MF population present in the bioengineered model. Chapter 7 served as a broad discussion of the field of fibrosis bioengineering, with specific focus on the role those emerging technologies may play in the future of fibrosis research.

8.2 Future Directions: Four Goals for Fibrosis Bioengineering

As previously discussed in Chapters 6-7, the continued development of bioengineered disease models will be critical for the future of fibrosis research. Via recapitulating aspects of pulmonary ECM structure, the modalities presented here serve as a logical first step in enhancing 3D biomimicry. While an advancement, future models will need to accomplish four major milestones going forward.

Firstly, ECM models will need to traverse numerous length scales in an effort to incorporate lung-specific features. To mimic tissue-scale respiration, this includes the generation of alveolar geometries as well as the ability to externally actuate 3D hydrogels at relevant timescales. Given that cells within the lung experience a unique mechanical environment, such efforts would aid in understanding the mechanobiology unique to PF. At the cellular level, fibrotic progression into tissue parenchyma is highly understudied; how fibroblasts traverse the barriers between interstitial and parenchymal ECM remains unknown. While 2D patterning is well-established, 3D patterning technologies would be a major advance, allowing researchers to investigate how parenchymal ECM and mechanics affect cells expanding from an interstitia. Indeed, alveoli possess unique ligands and topographies compared to collagenous ECM; the

impact of these features on MFs is underexplored. Recent advances in bioprinting technologies may aid in the technological barrier to high-fidelity patterning in 3D.

Secondly, fibrosis researchers will eventually have to move away from studying models of fibrogenesis. After all, patients presenting with PF in the clinic may be years removed from the early stages of tissue repair that promote fibroblast proliferation; whether MF differentiation continues at terminal stages of the disease is unknown. While bioengineers possess the ability to study these events at much faster time scales, the ability to conduct long term cultures should not be overlooked. Indeed, understanding the factors that promote the apoptosis or de-differentiation of an existing MF population may be more clinical relevant. Furthermore, the scRNA-seq results presented in Chapter 6 suggest that a loss of normal fibroblast phenotype (for example, accumulation of non-functional lipofibroblasts) occurs alongside MF expansion. Such evidence encourages the development of new platforms beyond the traditional TGF-β1 mediated MF differentiation assays.

Thirdly, future models should incorporate the use of various celltypes, preferably with primary cell isolates as opposed to cell lines. While the contributions of numerous cell lineages remains understudied, evidence presented in Chapters 6-7 suggests that exploring endothelial-fibroblast crosstalk may be an advantageous pursuit. Furthermore, the synthetic materials established here are compatible with recently developed organ-on-chip platforms; microfluidic systems that support the creation of functional, perfusable capillary beds at the scale of lung vasculature are a logical next step. The combination of these materials will allow for co-culture between vasculature, lung fibroblasts, and other celltypes such as macrophages. Mutlicompartment designs may allow for temporal control over when secondary celltypes are incorporated, helping researchers dissect multivariate processes that are difficult to parse *in vivo*.

Nevertheless, the difficulty in recapitulating complex human biology with synthetic technologies cannot be understated; patient data and *in vivo* models will need to be used in concert if translation is the goal.

Finally, computational biologists have developed an array of powerful and accessible bioinformatics modalities that should not be neglected. Looking forward, the rise of multi-omics data and deep learning in histopathology will soon provide a wealth of spatiotemporal information across biological scales. These resources will not only accelerate biological discovery but will serve as a guidepost for basic research. Notably, as all models possess artefactual elements, quantitative systems-based approaches may finally allow for precise measurement of biological models and their accuracy relative to human disease. In fact, the bioengineering field lacks standardization or defined evaluation criteria to compare technologies; quantitative bioinformatics technologies will likely be required for such efforts.

Bibliography

Aref, A. R., Ruby Yun-Ju Huang, ab, Weimiao Yu, cd, Chua, K.-N., Sun, W., Tu, T.-Y., … Kamm, R. D. (2013). Screening therapeutic EMT blocking agents in a three-dimensional microenvironment. *Integr. Biol. Integr. Biol*, *5*(5), 381–389. https://doi.org/10.1039/c2ib20209c

Arora, P. D., Narani, N., & McCulloch, C. A. G. (1999). The Compliance of Collagen Gels Regulates Transforming Growth Factor-β Induction of α-Smooth Muscle Actin in Fibroblasts. *The American Journal of Pathology*, *154*(3), 871–882. https://doi.org/10.1016/S0002-9440(10)65334-5

Asmani, M., Velumani, S., Li, Y., Wawrzyniak, N., Hsia, I., Chen, Z., … Zhao, R. (2018). Fibrotic microtissue array to predict anti-fibrosis drug efficacy. *Nature Communications*, *9*(1), 1–12. https://doi.org/10.1038/s41467-018-04336-z

Bagnato, G., & Harari, S. (2015). Cellular interactions in the pathogenesis of interstitial lung diseases. *European Respiratory Review*, *24*(135), 102–114. https://doi.org/10.1183/09059180.00003214

Baker, B. M., Gee, A. O., Metter, R. B., Nathan, A. S., Marklein, R. A., Burdick, J. A., & Mauck, R. L. (2008). The potential to improve cell infiltration in composite fiber-aligned electrospun scaffolds by the selective removal of sacrificial fibers. *Biomaterials*, *29*(15), 2348–2358. https://doi.org/10.1016/j.biomaterials.2008.01.032

Baker, B. M., Trappmann, B., Wang, W. Y., Sakar, M. S., Kim, I. L., Shenoy, V. B., … Chen, C. S. (2015). Cell-mediated fibre recruitment drives extracellular matrix mechanosensing in engineered fibrillar microenvironments. *Nature Materials*, *14*(12), 1262–1268. https://doi.org/10.1038/nmat4444

Balestrini, J. L., Chaudhry, S., Sarrazy, V., Koehler, A., & Hinz, B. (2012). The mechanical memory of lung myofibroblasts. *Integrative Biology*, *4*(4), 410–421. https://doi.org/10.1039/c2ib00149g

Barker, T. H., & Engler, A. J. (2017). The provisional matrix: setting the stage for tissue repair outcomes. *Matrix Biology*, *60–61*, 1–4. https://doi.org/10.1016/j.matbio.2017.04.003

Barrett, T., Wilhite, S. E., Ledoux, P., Evangelista, C., Kim, I. F., Tomashevsky, M., … Soboleva, A. (2013). NCBI GEO: Archive for functional genomics data sets - Update. *Nucleic Acids Research*, *41*(D1), 991–995. https://doi.org/10.1093/nar/gks1193

Bellis, S. L. (2011). Advantages of RGD peptides for directing cell association with biomaterials. *Biomaterials*, *32*(18), 4205–4210. https://doi.org/10.1016/j.biomaterials.2011.02.029

Berger, A. J., Linsmeier, K. M., Kreeger, P. K., & Masters, K. S. (2017). Decoupling the effects of stiffness and fiber density on cellular behaviors via an interpenetrating network of gelatin-methacrylate and collagen. *Biomaterials*, *141*, 125–135. https://doi.org/10.1016/j.biomaterials.2017.06.039

Bochaton Piallat, M.-L., Gabbiani, G., & Hinz, B. (2016). The Myofibroblast in wound healing

and fibrosis: Answered and unanswered questions. *F1000 Research*, *5*(5). https://doi.org/10.12688/f1000research.8190.1

Caliari, S. R., Vega, S. L., Kwon, M., Soulas, E. M., & Burdick, J. A. (2016). Dimensionality and spreading influence MSC YAP/TAZ signaling in hydrogel environments. *Biomaterials*, *103*, 314–323. https://doi.org/10.1016/j.biomaterials.2016.06.061

Califano, J. P., & Reinhart-King, C. A. (2008). A Balance of Substrate Mechanics and Matrix Chemistry Regulates Endothelial Cell Network Assembly. *Cellular and Molecular Bioengineering*, *1*(2–3), 122–132. https://doi.org/10.1007/s12195-008-0022-x

Calvo, F., Ege, N., Grande-Garcia, A., Hooper, S., Jenkins, R. P., Chaudhry, S. I., … Sahai, E. (2013). Mechanotransduction and YAP-dependent matrix remodelling is required for the generation and maintenance of cancer-associated fibroblasts. *Nature Cell Biology*, *15*(6), 637–646. https://doi.org/10.1038/ncb2756

Carone, M., Salerno, F. G., & Esquinas, A. M. (2016). Obstructive lung function decline and IPF. *Chronic Respiratory Disease*, *13*(2), 204–205. https://doi.org/10.1177/1479972316628534

Castella, L. F., Buscemi, L., Godbout, C., Meister, J. J., & Hinz, B. (2010). A new lock-step mechanism of matrix remodelling based on subcellular contractile events. *Journal of Cell Science*, *123*(10), 1751–1760. https://doi.org/10.1242/jcs.066795

Choi, S. S., Witek, R. P., Yang, L., Omenetti, A., Syn, W. K., Moylan, C. A., … Diehl, A. M. (2010). Activation of Rac1 promotes hedgehog-mediated acquisition of the myofibroblastic phenotype in rat and human hepatic stellate cells. *Hepatology*, *52*(1), 278–290. https://doi.org/10.1002/hep.23649

Chong, S. G., Sato, S., Kolb, M., & Gauldie, J. (2019). Fibrocytes and fibroblasts—Where are we now. *International Journal of Biochemistry and Cell Biology*, *116*(July), 105595. https://doi.org/10.1016/j.biocel.2019.105595

Coburn, J., Gibson, M., Bandalini, P. A., Laird, C., Mao, H. Q., Moroni, L., … Elisseeff, J. (2011). Biomimetics of the extracellular matrix: An integrated three-dimensional fiber-hydrogel composite for cartilage tissue engineering. *Smart Structures and Systems*, *7*(3), 213–222. https://doi.org/10.12989/sss.2011.7.3.213

Colombat, M., Mal, H., Groussard, O., Capron, F., Thabut, G., Jebrak, G., … Fournier, M. (2007). Pulmonary vascular lesions in end-stage idiopathic pulmonary fibrosis: histopathologic study on lung explant specimens and correlations with pulmonary hemodynamics. *Human Pathology*, *38*(1), 60–65. https://doi.org/10.1016/j.humpath.2006.06.007

Comley, K., & Fleck, N. A. (2010). A micromechanical model for the Young's modulus of adipose tissue. *International Journal of Solids and Structures*, *47*(21), 2982–2990. https://doi.org/10.1016/j.ijsolstr.2010.07.001

Corbel, M., Lanchou, J., Germain, N., Malledant, Y., Boichot, E., & Lagente, V. (2001). Modulation of airway remodeling-associated mediators by the antifibrotic compound, pirfenidone, and the matrix metalloproteinase inhibitor, batimastat, during acute lung injury in mice. *European Journal of Pharmacology*, *426*(1–2), 113–121. https://doi.org/10.1016/S0014-2999(01)01209-2

Cox, T. R., & Erler, J. T. (2011a). Remodeling and homeostasis of the extracellular matrix: implications for fibrotic diseases and cancer. *Disease Models & Mechanisms*, *4*(2), 165–178. https://doi.org/10.1242/dmm.004077

Cox, T. R., & Erler, J. T. (2011b). Remodeling and homeostasis of the extracellular matrix:

implications for fibrotic diseases and cancer. *Disease Models & Mechanisms*, *4*(2), 165–178. https://doi.org/10.1242/dmm.004077

Czirók, A., Rongish, B. J., & Little, C. D. (2004). Extracellular matrix dynamics during vertebrate axis formation. *Developmental Biology*, *268*(1), 111–122. https://doi.org/10.1016/j.ydbio.2003.09.040

Darby, I. A., & Hewitson, T. D. (2007). Fibroblast Differentiation in Wound Healing and Fibrosis. *International Review of Cytology*, *257*(07), 143–179. https://doi.org/10.1016/S0074-7696(07)57004-X

Darby, I., Skalli, O., & Gabbiani, G. (1990). Alpha-smooth muscle actin is transiently expressed by myofibroblasts during experimental wound healing. *Laboratory Investigation; a Journal of Technical Methods and Pathology*, *63*(1), 21–29. https://doi.org/10.1017/CBO9781107415324.004

Davidson, C. D., Jayco, D. K. P., Matera, D. L., DePalma, S. J., Hiraki, H. L., Wang, W. Y., & Baker, B. M. (2020). Myofibroblast activation in synthetic fibrous matrices composed of dextran vinyl sulfone. *Acta Biomaterialia*, *105*, 78–86. https://doi.org/10.1016/j.actbio.2020.01.009

Davidson, C. D., Wang, W. Y., Zaimi, I., Jayco, D. K. P., & Baker, B. M. (2019). Cell force-mediated matrix reorganization underlies multicellular network assembly. *Scientific Reports*, *9*(1), 1–13. https://doi.org/10.1038/s41598-018-37044-1

de Meijer, V. E., Sverdlov, D. Y., Popov, Y., Le, H. D., Meisel, J. A., Nosé, V., … Puder, M. (2010). Broad-spectrum matrix metalloproteinase inhibition curbs inflammation and liver injury but aggravates experimental liver fibrosis in mice. *PLoS ONE*, *5*(6). https://doi.org/10.1371/journal.pone.0011256

Deroanne, C. F., Hamelryckx, D., Ho, T. T. G., Lambert, C. A., Catroux, P., Lapière, C. M., & Nusgens, B. V. (2005). Cdc42 downregulates MMP-1 expression by inhibiting the ERK1/2 pathway. *Journal of Cell Science*, *118*(6), 1173–1183. https://doi.org/10.1242/jcs.01707

Discher, D. E. (2005). Tissue Cells Feel and Respon to the Stiffness of Their Substrate. *Science*, *310*(5751), 1139–1143. https://doi.org/10.1126/science.1116995

Doyle, A. D., Carvajal, N., Jin, A., Matsumoto, K., & Yamada, K. M. (2015). Local 3D matrix microenvironment regulates cell migration through spatiotemporal dynamics of contractility-dependent adhesions. *Nature Communications*. https://doi.org/10.1038/ncomms9720

Draghici, S., Nguyen, T.-M., Sonna, L. A., Ziraldo, C., Vanciu, R. L., Fadel, R., … Mor, G. (2020). COVID-19: disease pathways and gene expression changes predict methylprednisolone can improve out- come in severe cases. *MedRxiv*, 2020.05.06.20076687. https://doi.org/10.1101/2020.05.06.20076687

Ebrahimkhani, M. R., Young, C. L., Lauffenburger, D. A., Griffith, L. G., & Borenstein, J. T. (2014). Approaches to *in vitro* tissue regeneration with application for human disease modeling and drug development. *Drug Discovery Today*, *19*(6), 754–762. https://doi.org/10.1016/j.drudis.2014.04.017

Edlund, S., Landström, M., Heldin, C. H., & Aspenström, P. (2002). Transforming growth factor-β-induced mobilization of actin cytoskeleton requires signaling by small GTPases Cdc42 and RhoA. *Molecular Biology of the Cell*, *13*(3), 902–914. https://doi.org/10.1091/mbc.01-08-0398

Ehling, J., Bartneck, M., Wei, X., Gremse, F., Fech, V., Möckel, D., … Tacke, F. (2014). CCL2-dependent infiltrating macrophages promote angiogenesis in progressive liver fibrosis. *Gut*,

63(12), 1960–1971. https://doi.org/10.1136/gutjnl-2013-306294
Ekaputra, A. K., Prestwich, G. D., Cool, S. M., & Hutmacher, D. W. (2008). Combining electrospun scaffolds with electrosprayed hydrogels leads to three-dimensional cellularization of hybrid constructs. *Biomacromolecules*, *9*(8), 2097–2103. https://doi.org/10.1021/bm800565u
El Agha, E., Moiseenko, A., Kheirollahi, V., De Langhe, S., Crnkovic, S., Kwapiszewska, G., … Bellusci, S. (2017). Two-Way Conversion between Lipogenic and Myogenic Fibroblastic Phenotypes Marks the Progression and Resolution of Lung Fibrosis. *Cell Stem Cell*, *20*(2), 261-273.e3. https://doi.org/10.1016/j.stem.2016.10.004
Engler, A. J., Sen, S., Sweeney, H. L., & Discher, D. E. (2006). Matrix Elasticity Directs Stem Cell Lineage Specification. *Cell*, *126*(4), 677–689. https://doi.org/10.1016/j.cell.2006.06.044
Fallica, B., Maffei, J. S., Villa, S., Makin, G., & Zaman, M. (2012). Alteration of Cellular Behavior and Response to PI3K Pathway Inhibition by Culture in 3D Collagen Gels. *PLoS ONE*, *7*(10), 1–11. https://doi.org/10.1371/journal.pone.0048024
Fang, M., Yuan, J., Peng, C., & Li, Y. (2014). Collagen as a double-edged sword in tumor progression. *Tumour Biology : The Journal of the International Society for Oncodevelopmental Biology and Medicine*, *35*(4), 2871–2882. https://doi.org/10.1007/s13277-013-1511-7
Farber, D. L., & Sims, P. A. (2019). Dissecting lung development and fibrosis at single-cell resolution. *Genome Medicine*, *11*(1), 10–12. https://doi.org/10.1186/s13073-019-0645-7
Fiore, V. F., Wong, S., Tran, C., Tan, C., Xu, W., White, E. S., … Barker, T. H. (2018). Integrin a v b 3 drives fibroblast contraction and strain stiffening of soft provisional extracellular matrix during progressive fibrosis, *3*(20), 1–35. https://doi.org/10.1172/jci.insight.97597
Follonier, L., Schaub, S., Meister, J.-J., & Hinz, B. (2008a). Myofibroblast communication is controlled by intercellular mechanical coupling. *Journal of Cell Science*, *121*(20), 3305–3316. https://doi.org/10.1242/jcs.024521
Follonier, L., Schaub, S., Meister, J.-J., & Hinz, B. (2008b). Myofibroblast communication is controlled by intercellular mechanical coupling. *Journal of Cell Science*, *121*(20), 3305–3316. https://doi.org/10.1242/jcs.024521
Fong, E. L. S., Harrington, D. A., Farach-Carson, M. C., & Yu, H. (2016). Heralding a new paradigm in 3D tumor modeling. *Biomaterials*, *108*, 197–213. https://doi.org/10.1016/j.biomaterials.2016.08.052
Frantz, C., Stewart, K. M., & Weaver, V. M. (2010). The extracellular matrix at a glance. *Journal of Cell Science*, *123*(24), 4195–4200. https://doi.org/10.1242/jcs.023820
Furtado, K. S., Prado, M. G., Aguiar e Silva, M. A., Dias, M. C., Rivelli, D. P., Rodrigues, M. A. M., & Barbisan, L. F. (2012). Coffee and Caffeine Protect against Liver Injury Induced by Thioacetamide in Male Wistar Rats. *Basic and Clinical Pharmacology and Toxicology*, *111*(5), 339–347. https://doi.org/10.1111/j.1742-7843.2012.00903.x
Gabbiani, G., Chaponnier, C., & Huttner, I. (1978). Cytoplasmic filaments and gap junctions in epithelial cells and myofibroblasts during wound healing. *Journal of Cell Biology*, *76*(3), 561–568. https://doi.org/10.1083/jcb.76.3.561
Gabbiani, Giulio. (2003). The myofibroblast in wound healing and fibrocontractive diseases. *Journal of Pathology*, *200*(4), 500–503. https://doi.org/10.1002/path.1427
Ge, J., Burnier, L., Adamopoulou, M., Kwa, M. Q., Schaks, M., Rottner, K., & Brakebusch, C. (2018). RhoA, Rac1 and Cdc42 differentially regulate aSMA and collagen I expression in

mesenchymal stem cells. *The Journal of Biological Chemistry*, *293*, jbc.RA117.001113. https://doi.org/10.1074/jbc.RA117.001113

Ghajar, C. M., Chen, X., Harris, J. W., Suresh, V., Hughes, C. C. W., Jeon, N. L., … George, S. C. (2008). The effect of matrix density on the regulation of 3-D capillary morphogenesis. *Biophysical Journal*, *94*(5), 1930–1941. https://doi.org/10.1529/biophysj.107.120774

Gharaee-kermani, M., Mccullumsmith, R. E., Charo, I. F., Kunkel, S. L., & Phan, S. H. (2003). CC-chemokine receptor 2 required for bleomycin-induced pulmonary fibrosis, *24*, 266–276. https://doi.org/10.1016/j.cyto.2003.08.003

Giménez, A., Duch, P., Puig, M., Gabasa, M., Xaubet, A., & Alcaraz, J. (2017). Dysregulated collagen homeostasis by matrix stiffening and TGF-β1 in fibroblasts from idiopathic pulmonary fibrosis patients: Role of FAK/Akt. *International Journal of Molecular Sciences*, *18*(11). https://doi.org/10.3390/ijms18112431

Griffin, D. R., Weaver, W. M., Scumpia, P. O., Di Carlo, D., & Segura, T. (2015). Accelerated wound healing by injectable microporous gel scaffolds assembled from annealed building blocks. *Nature Materials*, *14*(7), 737–744. https://doi.org/10.1038/nmat4294

Grzegorzewska, A. P., Seta, F., Han, R., Czajka, C. A., Makino, K., Stawski, L., … Trojanowska, M. (2017). Dimethyl Fumarate ameliorates pulmonary arterial hypertension and lung fibrosis by targeting multiple pathways. *Scientific Reports*, *7*(July 2016), 1–14. https://doi.org/10.1038/srep41605

Gunatillake, P. A., Adhikari, R., & Gadegaard, N. (2003). Biodegradable synthetic polymers for tissue engineering. *European Cells and Materials*, *5*, 1–16. https://doi.org/10.22203/eCM.v005a01

Guo, C. L., Ouyang, M., & Yu, J. Y. (2013). Long-range mechanical force enables self-assembly of epithelial tubules. *Conference Proceedings of the Society for Experimental Mechanics Series*, *5*, 15–21. https://doi.org/10.1007/978-1-4614-4427-5_3

H. Bart van der Worp, D. W. Howells, E.S. Sena, M.J. Porritt, S. Rewell, V. O'Collins, M. R. M. (2016). Can Animal Models of Disease Reliably Inform Human Studies? *PLoS ONE*, *11*(5). https://doi.org/10.1371/journal

Habermann, A. C., Gutierrez, A. J., Bui, L. T., Yahn, S. L., Winters, N. I., Carla, L., … Ware, L. B. (2019). Single-cell RNA-sequencing reveals profibrotic roles of distinct epithelial and mesenchymal lineages in pulmonary fibrosis. *BioRxiv*, 753806. https://doi.org/https://doi.org/10.1101/753806

Hafemeister, C., & Satija, R. (2019). Normalization and variance stabilization of single-cell RNA-seq data using regularized negative binomial regression. *Genome Biology*, *20*(1), 1–15. https://doi.org/10.1186/s13059-019-1874-1

Hall, M. S., Alisafaei, F., Ban, E., Feng, X., Hui, C.-Y., Shenoy, V. B., & Wu, M. (2016). Fibrous nonlinear elasticity enables positive mechanical feedback between cells and ECMs. *Proceedings of the National Academy of Sciences of the United States of America*, *113*(49), 14043–14048. https://doi.org/10.1073/pnas.1613058113

Handorf, A. M., Zhou, Y., Halanski, M. A., & Li, W. J. (2015). Tissue stiffness dictates development, homeostasis, and disease progression. *Organogenesis*, *11*(1), 1–15. https://doi.org/10.1080/15476278.2015.1019687

Hassiba, A. J., El Zowalaty, M. E., Nasrallah, G. K., Webster, T. J., Luyt, A. S., Abdullah, A. M., & Elzatahry, A. A. (2016). Review of recent research on biomedical applications of electrospun polymer nanofibers for improved wound healing. *Nanomedicine*, *11*(6), 715–737. https://doi.org/10.2217/nnm.15.211

Hinz, B. (2016). The role of myofibroblasts in wound healing. *Current Research in Translational Medicine*, *64*(4), 171–177. https://doi.org/10.1016/j.retram.2016.09.003
Hinz, Boris. (2007). Formation and Function of the Myofibroblast during Tissue Repair. *Journal of Investigative Dermatology*, *127*(3), 526–537. https://doi.org/10.1038/sj.jid.5700613
Hinz, Boris, & Gabbiani, G. (2003). Cell-matrix and cell-cell contacts of myofibroblasts: Role in connective tissue remodeling. *Thrombosis and Haemostasis*, *90*(6), 993–1002. https://doi.org/10.1160/th03-05-0328
Hinz, Boris, Mcculloch, C. A., & Coelho, N. M. (2019). Mechanical regulation of myofibroblast phenoconversion and collagen contraction. *Experimental Cell Research*, *379*(1), 119–128. https://doi.org/10.1016/j.yexcr.2019.03.027
Hinz, Boris, Phan, S. H., Thannickal, V. J., Prunotto, M., Desmoulire, A., Varga, J., … Gabbiani, G. (2012). Recent developments in myofibroblast biology: Paradigms for connective tissue remodeling. *American Journal of Pathology*, *180*(4), 1340–1355. https://doi.org/10.1016/j.ajpath.2012.02.004
Hoch, E., Hirth, T., Tovar, G. E. M., & Borchers, K. (2013). Chemical tailoring of gelatin to adjust its chemical and physical properties for functional bioprinting. *Journal of Materials Chemistry B*, *1*(41), 5675. https://doi.org/10.1039/c3tb20745e
Hotary, K., Li, X. Y., Allen, E., Stevens, S. L., & Weiss, S. J. (2006). A cancer cell metalloprotease triad regulates the basement membrane transmigration program. *Genes and Development*, *20*(19), 2673–2686. https://doi.org/10.1101/gad.1451806
Howard, E. W., Crider, B. J., Updike, D. L., Bullen, E. C., Parks, E. E., Haaksma, C. J., … Tomasek, J. J. (2012). MMP-2 expression by fibroblasts is suppressed by the myofibroblast phenotype. *Experimental Cell Research*, *318*(13), 1542–1553. https://doi.org/10.1016/j.yexcr.2012.03.007
Huang, X., Yang, N., Fiore, V. F., Barker, T. H., Sun, Y., Morris, S. W., … Zhou, Y. (2012). Matrix stiffness-induced myofibroblast differentiation is mediated by intrinsic mechanotransduction. *American Journal of Respiratory Cell and Molecular Biology*, *47*(3), 340–348. https://doi.org/10.1165/rcmb.2012-0050OC
Humphrey, J. D., Dufresne, E. R., & Schwartz, M. A. (2014). Mechanotransduction and extracellular matrix homeostasis. *Nature Reviews Molecular Cell Biology*, *15*(12), 802–812. https://doi.org/10.1038/nrm3896
Huveneers, S., & Danen, E. H. J. (2009). Adhesion signaling - crosstalk between integrins, Src and Rho. *Journal of Cell Science*, *122*(8), 1059–1069. https://doi.org/10.1242/jcs.039446
Igata, T., Jinnin, M., Makino, T., Moriya, C., Muchemwa, F. C., Ishihara, T., & Ihn, H. (2010). Up-regulated type I collagen expression by the inhibition of Rac1 signaling pathway in human dermal fibroblasts. *Biochemical and Biophysical Research Communications*, *393*(1), 101–105. https://doi.org/10.1016/j.bbrc.2010.01.090
Jassal, B., Matthews, L., Viteri, G., Gong, C., Lorente, P., Fabregat, A., … D'Eustachio, P. (2019). The reactome pathway knowledgebase. *Nucleic Acids Research*, 2–7. https://doi.org/10.1093/nar/gkz1031
Jiang, D., Dey, T., & Liu, G. (2020). Recent developments in the pathobiology of lung myofibroblasts. *Expert Review of Respiratory Medicine*, *00*(00), 1–9. https://doi.org/10.1080/17476348.2021.1829972
Jiang, J., Parker, C. E., Fuller, J. R., Kawula, T. H., & H, C. (2008). Age-Related Intimal Stiffening Enhances Endothelial Permeability and Leukocyte Transmigration. *Anal Chim Acta*, *605*(1), 70–79. https://doi.org/10.1016/j.immuni.2010.12.017.Two-stage

Jin, S., Guerrero-Juarez, C. F., Zhang, L., Chang, I., Ramos, R., Kuan, C. H., … Nie, Q. (2021). Inference and analysis of cell-cell communication using CellChat. *Nature Communications*, *12*(1), 1–20. https://doi.org/10.1038/s41467-021-21246-9

Kendall, R. T., & Feghali-Bostwick, C. A. (2014). Fibroblasts in fibrosis: Novel roles and mediators. *Frontiers in Pharmacology*, *5 MAY*(May), 1–13. https://doi.org/10.3389/fphar.2014.00123

Kim, S. H., Turnbull, J., & Guimond, S. (2011). Extracellular matrix and cell signalling: The dynamic cooperation of integrin, proteoglycan and growth factor receptor. *Journal of Endocrinology*, *209*(2), 139–151. https://doi.org/10.1530/JOE-10-0377

Kim, S., Uroz, M., Bays, J. L., & Chen, C. S. (2021). Harnessing Mechanobiology for Tissue Engineering. *Developmental Cell*, *56*(2), 180–191. https://doi.org/10.1016/j.devcel.2020.12.017

Klingberg, F., Hinz, B., & White, E. S. (2013). The myofibroblast matrix: Implications for tissue repair andfibrosis. *Journal of Pathology*. https://doi.org/10.1002/path.4104

Knight, E., & Przyborski, S. (2015). Advances in 3D cell culture technologies enabling tissue-like structures to be created *in vitro*. *Journal of Anatomy*, *227*(6), 746–756. https://doi.org/10.1111/joa.12257

Kolb, P., Upagupta, C., Vierhout, M., Ayaub, E., Bellaye, P. S., Gauldie, J., … Kolb, M. R. J. (2020). The importance of interventional timing in the bleomycin model of pulmonary fibrosis. *European Respiratory Journal*, *55*(6). https://doi.org/10.1183/13993003.01105-2019

Kottmann, R. M., Sharp, J., Owens, K., Salzman, P., Xiao, G. Q., Phipps, R. P., … Perry, S. W. (2015). Second harmonic generation microscopy reveals altered collagen microstructure in usual interstitial pneumonia versus healthy lung. *Respiratory Research*, *16*(1), 1–13. https://doi.org/10.1186/s12931-015-0220-8

Kurita, Y., Araya, J., Minagawa, S., Hara, H., Ichikawa, A., Saito, N., … Morikawa, T. (2017). Pirfenidone inhibits myofibroblast differentiation and lung fibrosis development during insufficient mitophagy, 1–14. https://doi.org/10.1186/s12931-017-0600-3

Layton, T. B., Williams, L., Mccann, F., Zhang, M., Fritszche, M., Colin-york, H., … Nanchahal, J. (n.d.). Cellular census of human fibrosis defines functionally distinct stromal cell types and states. *Nature Communications*, (2020), 1–11. https://doi.org/10.1038/s41467-020-16264-y

Leong, W. S., Wu, S. C., Ng, K., & Tan, L. P. (2016). Electrospun 3D multi-scale fibrous scaffold for enhanced human dermal fibroblast infiltration. *International Journal of Bioprinting*, *2*(1).

Li, L., Eyckmans, J., & Chen, C. S. (2017). Designer biomaterials for mechanobiology. *Nature Materials*, *16*(12), 1164–1168. https://doi.org/10.1038/nmat5049

Li, X., Zhu, L., Wang, B., Yuan, M., & Zhu, R. (2017). Drugs and targets in fibrosis. *Frontiers in Pharmacology*, *8*(NOV). https://doi.org/10.3389/fphar.2017.00855

Liang, C. C., Park, A. Y., & Guan, J. L. (2007). *In vitro* scratch assay: A convenient and inexpensive method for analysis of cell migration *in vitro*. *Nature Protocols*, *2*(2), 329–333. https://doi.org/10.1038/nprot.2007.30

Liberati, T. A., Randle, M. R., & Toth, L. A. (2010). *In vitro* lung slices: A powerful approach for assessment of lung pathophysiology. *Expert Review of Molecular Diagnostics*, *10*(4), 501–508. https://doi.org/10.1586/erm.10.21

Liu, F., Lagares, D., Choi, K. M., Stopfer, L., Marinković, A., Vrbanac, V., … Tschumperlin, D.

J. (2015a). Mechanosignaling through YAP and TAZ drives fibroblast activation and fibrosis. *American Journal of Physiology - Lung Cellular and Molecular Physiology*, *308*(4), L344–L357. https://doi.org/10.1152/ajplung.00300.2014

Liu, F., Lagares, D., Choi, K. M., Stopfer, L., Marinković, A., Vrbanac, V., … Tschumperlin, D. J. (2015b). Mechanosignaling through YAP and TAZ drives fibroblast activation and fibrosis. *American Journal of Physiology - Lung Cellular and Molecular Physiology*, *308*(4).

Liu, F., & Tschumperlin, D. J. (2011). Micro-mechanical characterization of lung tissue using atomic force microscopy. *Journal of Visualized Experiments : JoVE*, (54), 1–7. https://doi.org/10.3791/2911

Liu, S., Kapoor, M., & Leask, A. (2009). Rac1 expression by fibroblasts is required for tissue repair *in vivo*. *American Journal of Pathology*, *174*(5), 1847–1856. https://doi.org/10.2353/ajpath.2009.080779

Liu, S., Kapoor, M., Xu, S. W., Kennedy, L., Denton, C. P., Glogauer, M., … Leask, A. (2008). Role of Rac1 in a bleomycin-induced scleroderma model using fibroblast-specific Rac1-knockout mice. *Arthritis and Rheumatism*, *58*(7), 2189–2195. https://doi.org/10.1002/art.23595

Loebel, C., Kwon, M. Y., Wang, C., Han, L., Mauck, R. L., & Burdick, J. A. (2020). Metabolic Labeling to Probe the Spatiotemporal Accumulation of Matrix at the Chondrocyte–Hydrogel Interface. *Advanced Functional Materials*, *1909802*, 1–10. https://doi.org/10.1002/adfm.201909802

Luzina, I. G., Todd, N. W., Sundararajan, S., & Atamas, S. P. (2015). The cytokines of pulmonary fibrosis: Much learned, much more to learn. *Cytokine*, *74*(1), 88–100. https://doi.org/10.1016/j.cyto.2014.11.008

Madl, C. M., Lesavage, B. L., Dewi, R. E., Dinh, C. B., Stowers, R. S., Khariton, M., … Heilshorn, S. C. (2017). Maintenance of neural progenitor cell stemness in 3D hydrogels requires matrix remodelling. *Nature Materials*, *16*(12), 1233–1242. https://doi.org/10.1038/nmat5020

Mason, B. N., Starchenko, A., Williams, R. M., Bonassar, L. J., & Reinhart-King, C. A. (2013). Tuning three-dimensional collagen matrix stiffness independently of collagen concentration modulates endothelial cell behavior. *Acta Biomaterialia*, *9*(1), 4635–4644. https://doi.org/10.1016/j.actbio.2012.08.007

Matera, D. L., DiLillo, K. M., Smith, M. R., Davidson, C. D., Parikh, R., Said, M., … Baker, B. M. (2020). Microengineered 3D pulmonary interstitial mimetics highlight a critical role for matrix degradation in myofibroblast differentiation. *Science Advances*, *6*(37), 1–15. https://doi.org/10.1126/sciadv.abb5069

Matera, D. L., Wang, W. Y., & Baker, B. M. (n.d.). New directions and dimensions for bioengineered models of fibrosis. *Nature Reviews Materials*, *0123456789*, 2–5. https://doi.org/10.1038/s41578-021-00288-x

Matera, D. L., Wang, W. Y., Smith, M. R., Shikanov, A., & Baker, B. M. (2019). Fiber Density Modulates Cell Spreading in 3D Interstitial Matrix Mimetics. https://doi.org/10.1021/acsbiomaterials.9b00141

Mayorca-Guiliani, A. E., Madsen, C. D., Cox, T. R., Horton, E. R., Venning, F. A., & Erler, J. T. (2017). ISDoT: In situ decellularization of tissues for high-resolution imaging and proteomic analysis of native extracellular matrix. *Nature Medicine*, *23*(7), 890–898. https://doi.org/10.1038/nm.4352

McDonough, J. E., Ahangari, F., Li, Q., Jain, S., Verleden, S. E., Herazo-Maya, J., … Kaminski, N. (2019). Transcriptional regulatory model of fibrosis progression in the human lung. *JCI Insight*, *4*(22). https://doi.org/10.1172/jci.insight.131597

Meng, X. M., Nikolic-Paterson, D. J., & Lan, H. Y. (2016). TGF-β: The master regulator of fibrosis. *Nature Reviews Nephrology*, *12*(6), 325–338. https://doi.org/10.1038/nrneph.2016.48

Mercer, R., Crap, D., Carolina, N., Robert, R., Ii, J., & Spatial, C. (1990). Spatial distribution in the lungs.

Mia, M. M., Boersema, M., & Bank, R. A. (2014). Interleukin-1β attenuates myofibroblast formation and extracellular matrix production in dermal and lung fibroblasts exposed to transforming growth factor-β1. *PLoS ONE*, *9*(3). https://doi.org/10.1371/journal.pone.0091559

Miller, C., Jeftinija, S., & Mallapragada, S. (2002). Synergistic effects of physical and chemical guidance cues on neurite alignment and outgrowth on biodegradable polymer substrates. *Tissue Engineering*, *8*(3), 367–378. https://doi.org/10.1089/107632702760184646

Miron-Mendoza, M., Seemann, J., & Grinnell, F. (2010). The differential regulation of cell motile activity through matrix stiffness and porosity in three dimensional collagen matrices. *Biomaterials*, *31*(25), 6425–6435. https://doi.org/10.1016/j.biomaterials.2010.04.064

Morse, C., Tabib, T., Sembrat, J., Buschur, K. L., Bittar, H. T., Valenzi, E., … Lafyatis, R. (2019). Proliferating SPP1/MERTK-expressing macrophages in idiopathic pulmonary fibrosis. *European Respiratory Journal*, *54*(2). https://doi.org/10.1183/13993003.02441-2018

Mouw, J. K., Ou, G., & Weaver, V. M. (2014). Extracellular matrix assembly: a multiscale deconstruction. *Nature Reviews Molecular Cell Biology*, *15*(12), 771–785. https://doi.org/10.1038/nrm3902

Nakagawa, S., Pawelek, P., & Grinnell, F. (1989). Long-Term Culture of Fibroblasts in Contracted Collagen Gels: Effects on Cell Growth and Biosynthetic Activity. *Journal of Investigative Dermatology*, *93*(6), 792–798. https://doi.org/10.1111/1523-1747.ep12284425

Nakatsuji, N., & Johnson, K. E. (1984). Experimental manipulation of a contact guidance system in amphibian gastrulation by mechanical tension. *Nature*. https://doi.org/10.1038/307453a0

Nam, S., Lee, J., Brownfield, D. G., & Chaudhuri, O. (2016). Viscoplasticity Enables Mechanical Remodeling of Matrix by Cells. *Biophysical Journal*, *111*(10), 2296–2308. https://doi.org/10.1016/j.bpj.2016.10.002

Nichol, J. W., Koshy, S. T., Bae, H., Hwang, C. M., Yamanlar, S., & Khademhosseini, A. (2010). Cell-laden microengineered gelatin methacrylate hydrogels. *Biomaterials*, *31*(21), 5536–5544. https://doi.org/10.1016/j.biomaterials.2010.03.064

Nobes, C. D. (2000). Rho GTPases and Cell Migration-Fibroblast Wound. *Cell*, *325*(1996), 441–449.

O'Connor, J. W., & Gomez, E. W. (2013). Cell adhesion and shape regulate TGF-beta1-induced epithelial-myofibroblast transition via MRTF-A signaling. *PLoS ONE*, *8*(12), 1–11. https://doi.org/10.1371/journal.pone.0083188

Ogura, T., Taniguchi, H., Azuma, A., Inoue, Y., Kondoh, Y., Hasegawa, Y., … Fujimoto, T. (n.d.). Safety and pharmacokinetics of nintedanib and pirfenidone in idiopathic pulmonary fibrosis, 1382–1392. https://doi.org/10.1183/09031936.00198013

Oh, R. S., Haak, A. J., Smith, K. M. J., & Ligresti, G. (2018). RNAi screening identifies a mechanosensitive ROCK-JAK2-STAT3 network central to myofibroblast activation.

Journal of Cell Science. https://doi.org/10.1242/jcs.209932
Ohshima, M., Yamaguchi, Y., Ambe, K., Horie, M., Saito, A., Nagase, T., … Kappert, K. (2016). Fibroblast VEGF-receptor 1 expression as molecular target in periodontitis. *Journal of Clinical Periodontology*, *43*(2), 128–137. https://doi.org/10.1111/jcpe.12495
Olczyk, P., Mencner, Ł., & Komosinska-Vassev, K. (2015). Diverse Roles of Heparan Sulfate and Heparin in Wound Repair. *BioMed Research International*, *2015*. https://doi.org/10.1155/2015/549417
Ortega, S., Ittmann, M., Tsang, S. H., Ehrlich, M., & Basilico, C. (1998). Neuronal defects and delayed wound healing in mice lacking fibroblast growth factor 2. *Proceedings of the National Academy of Sciences of the United States of America*, *95*(10), 5672–5677. https://doi.org/10.1073/pnas.95.10.5672
Parker, M. W., Rossi, D., Peterson, M., Smith, K., Sikstroḿ, K., White, E. S., … Bitterman, P. B. (2014). Fibrotic extracellular matrix activates a profibrotic positive feedback loop. *Journal of Clinical Investigation*, *124*(4), 1622–1635. https://doi.org/10.1172/JCI71386
Paszek, M. J., Zahir, N., Johnson, K. R., Lakins, J. N., Rozenberg, G. I., Gefen, A., … Weaver, V. M. (2005). Tensional homeostasis and the malignant phenotype. *Cancer Cell*, *8*(3), 241–254. https://doi.org/10.1016/j.ccr.2005.08.010
Pathak, A., & Kumar, S. (2011). Biophysical regulation of tumor cell invasion: moving beyond matrix stiffness. *Integr Biol (Camb)*, *3*(4), 267–278. https://doi.org/10.1039/c0ib00095g
Pearce, O. M. T., Delaine-Smith, R., Maniati, E., Nichols, S., Wang, J., Böhm, S., … Balkwill, F. R. (2017). Deconstruction of a metastatic tumor microenvironment reveals a common matrix response in human cancers. *Cancer Discovery*, CD-17-0284. https://doi.org/10.1158/2159-8290.CD-17-0284
Peela, N., Truong, D., Saini, H., Chu, H., Mashaghi, S., Ham, S. L., … Nikkhah, M. (2017). Advanced biomaterials and microengineering technologies to recapitulate the stepwise process of cancer metastasis. *Biomaterials*, *133*, 176–207. https://doi.org/10.1016/j.biomaterials.2017.04.017
Peng, R., Sridhar, S., Tyagi, G., Phillips, J. E., Garrido, R., Harris, P., … Stevenson, C. S. (2013). Bleomycin Induces Molecular Changes Directly Relevant to Idiopathic Pulmonary Fibrosis: A Model for "Active" Disease. *PLoS ONE*, *8*(4). https://doi.org/10.1371/journal.pone.0059348
Pertz, O., Hodgson, L., Klemke, R. L., & Hahn, K. M. (2006). Spatiotemporal dynamics of RhoA activity in migrating cells. *Nature*, *440*(7087), 1069–1072. https://doi.org/10.1038/nature04665
Peyvandipour, A., Saberian, N., Shafi, A., Donato, M., & Draghici, S. (2018). Systems biology: A novel computational approach for drug repurposing using systems biology. *Bioinformatics*, *34*(16), 2817–2825. https://doi.org/10.1093/bioinformatics/bty133
Piera-Velazquez, S., Li, Z., & Jimenez, S. A. (2011). Role of Endothelial-Mesenchymal Transition (EndoMT) in the Pathogenesis of Fibrotic Disorders. *The American Journal of Pathology*, *179*(3), 1074–1080. https://doi.org/10.1016/j.ajpath.2011.06.001
Piersma, B., Bank, R. A., & Boersema, M. (2015). Signaling in Fibrosis: TGF-β, WNT, and YAP/TAZ Converge. *Frontiers in Medicine*, *2*(September), 1–14. https://doi.org/10.3389/fmed.2015.00059
Pittet, P., Lee, K., Kulik, A. J., Meister, J.-J., & Hinz, B. (2008). Fibrogenic fibroblasts increase intercellular adhesion strength by reinforcing individual OB-cadherin bonds. *Journal of Cell Science*, *121*(6), 877–886. https://doi.org/10.1242/jcs.024877

Plotnikov, S. V., Pasapera, A. M., Sabass, B., & Waterman, C. M. (2012). Force fluctuations within focal adhesions mediate ECM-rigidity sensing to guide directed cell migration. *Cell*, *151*(7), 1513–1527. https://doi.org/10.1016/j.cell.2012.11.034

Plouffe, S. W., Hong, A. W., & Guan, K. L. (2015). Disease implications of the Hippo/YAP pathway. *Trends in Molecular Medicine*, *21*(4), 212–222. https://doi.org/10.1016/j.molmed.2015.01.003

Pothula, S., Bazan, H. E. P., & Chandrasekher, G. (2013). Regulation of cdc42 expression and signaling is critical for promoting corneal epithelial wound healing. *Investigative Ophthalmology and Visual Science*, *54*(8), 5343–5352. https://doi.org/10.1167/iovs.13-11955

Provenzano, P. P., Eliceiri, K. W., Inman, D. R., & Keely, P. J. (2010). Engineering three-dimensional collagen matrices to provide contact guidance during 3D cell migration. *Current Protocols in Cell Biology*, (SUPPL. 47). https://doi.org/10.1002/0471143030.cb1017s47

Provenzano, P. P., Inman, D. R., Eliceiri, K. W., Knittel, J. G., Yan, L., Rueden, C. T., … Keely, P. J. (2008). Collagen density promotes mammary tumor initiation and progression. *BMC Medicine*, *6*(1), 11. https://doi.org/10.1186/1741-7015-6-11

Raghu, G., Brown, K. K., Collard, H. R., Cottin, V., Gibson, K. F., Kaner, R. J., … O'Riordan, T. G. (2017). Efficacy of simtuzumab versus placebo in patients with idiopathic pulmonary fibrosis: a randomised, double-blind, controlled, phase 2 trial. *The Lancet Respiratory Medicine*, *5*(1), 22–32. https://doi.org/10.1016/S2213-2600(16)30421-0

Ramirez-San Juan, G. R., Oakes, P. W., & Gardel, M. L. (2017). Contact guidance requires spatial control of leading-edge protrusion. *Molecular Biology of the Cell*, *28*(8), 1043–1053. https://doi.org/10.1091/mbc.E16-11-0769

Ravichandran, R., Venugopal, J. R., Sundarrajan, S., Mukherjee, S., Sridhar, R., & Ramakrishna, S. (2012). Minimally invasive injectable short nanofibers of poly(glycerol sebacate) for cardiac tissue engineering. *Nanotechnology*, *23*(38). https://doi.org/10.1088/0957-4484/23/38/385102

Reyfman, P. A., Walter, J. M., Joshi, N., Anekalla, K. R., McQuattie-Pimentel, A. C., Chiu, S., … Misharin, A. V. (2019). Single-cell transcriptomic analysis of human lung provides insights into the pathobiology of pulmonary fibrosis. *American Journal of Respiratory and Critical Care Medicine*, *199*(12), 1517–1536. https://doi.org/10.1164/rccm.201712-2410OC

Riching, K. M., Cox, B. L., Salick, M. R., Pehlke, C., Riching, A. S., Ponik, S. M., … Keely, P. J. (2015). 3D collagen alignment limits protrusions to enhance breast cancer cell persistence. *Biophysical Journal*, *107*(11), 2546–2558. https://doi.org/10.1016/j.bpj.2014.10.035

Richter, M. J., Grimminger, J. E. F., Ghofrani, H. A., Kojonazarov, B., Petrovic, A., Seeger, W., … Gall, H. (2018). Nintedanib in severe pulmonary arterial hypertension. *American Journal of Respiratory and Critical Care Medicine*, *198*(6), 808–810. https://doi.org/10.1164/rccm.201801-0195LE

Ridley, A. J. (2001). Rho GTPases and cell migration. *Journal of Cell Science*, *114*(15), 2713–2722.

Rockey, D. C., Bell, P. D., & Hill, J. A. (2015). Fibrosis — A Common Pathway to Organ Injury and Failure. *New England Journal of Medicine*, *372*(12), 1138–1149. https://doi.org/10.1056/NEJMra1300575

Russell, S. M., & Carta, G. (2005). Mesh size of charged polyacrylamide hydrogels from

partitioning measurements. *Industrial and Engineering Chemistry Research*, *44*(22), 8213–8217. https://doi.org/10.1021/ie050079m
Rys, J. P., Monteiro, D. A., & Alliston, T. (2016). Mechanobiology of TGFβ signaling in the skeleton. *Matrix Biology*, *52*, 413–425. https://doi.org/10.1016/j.matbio.2016.02.002
Sahin, H., & Wasmuth, H. E. (2013). Chemokines in tissue fibrosis. *Biochimica et Biophysica Acta - Molecular Basis of Disease*, *1832*(7), 1041–1048. https://doi.org/10.1016/j.bbadis.2012.11.004
Sakiyama-elbert, S. E., & Hubbell, J. A. (2000). Development of fibrin derivatives for controlled release of heparin-binding growth factors, *65*, 389–402.
Sander, E. E., Ten Klooster, J. P., Van Delft, S., Van Der Kammen, R. A., & Collard, J. G. (1999). Rac downregulates Rho activity: Reciprocal balance between both GTPases determines cellular morphology and migratory behavior. *Journal of Cell Biology*, *147*(5), 1009–1021. https://doi.org/10.1083/jcb.147.5.1009
Santos, A., & Lagares, D. (2018). Matrix Stiffness : the Conductor of Organ Fibrosis.
Sapudom, J., Rubner, S., Martin, S., Kurth, T., Riedel, S., Mierke, C. T., & Pompe, T. (2015). The phenotype of cancer cell invasion controlled by fibril diameter and pore size of 3D collagen networks. *Biomaterials*, *52*(1), 367–375. https://doi.org/10.1016/j.biomaterials.2015.02.022
Sato, Y., Fujiwara, H., & Takatsu, Y. (2012). Biochemical markers in heart failure. *Journal of Cardiology*, *59*(1), 1–7. https://doi.org/10.1016/j.jjcc.2011.11.001
Scharenberg, M. A., Pippenger, B. E., Sack, R., Zingg, D., Ferralli, J., Schenk, S., … Chiquet-Ehrismann, R. (2014). TGF-β-induced differentiation into myofibroblasts involves specific regulation of two MKL1 isoforms. *Journal of Cell Science*, *127*(5), 1079–1091. https://doi.org/10.1242/jcs.142075
Schaum, M., Pinzuti, E., Sebastian, A., Lieb, K., Fries, P., Mobascher, A., … Society, P. (2020). Single Cell RNA-seq reveals ectopic and aberrant lung resident cell populations in Idiopathic Pulmonary Fibrosis 5, 1–28.
Schraufnagel, D. E., Mehta, D., Harshbarger, R., Treviranus, K., & Wang, N. S. (1986). Capillary remodeling in bleomycin-induced pulmonary fibrosis. *American Journal of Pathology*, *125*(1), 97–106.
Schuett, J., Ostermann, A., & Wollin, L. (2015). The Effect Of Nintedanib Compared To Pirfenidone On Serum-Stimulated Proliferation Of Human Primary Lung Fibroblasts At Clinically Relevant Concentrations. *Am J Respir Rit Care Med*, *191*, A4940. Retrieved from www.atsjournals.org
Schupp, J. C., Adams, T. S., Cosme, C., Raredon, M. S. B., Yuan, Y., Omote, N., … Kaminski, N. (2021). Integrated Single-Cell Atlas of Endothelial Cells of the Human Lung. *Circulation*, 286–302. https://doi.org/10.1161/CIRCULATIONAHA.120.052318
Seager, R. J., Hajal, C., Spill, F., Kamm, R. D., & Zaman, M. H. (n.d.). Dynamic interplay between tumour, stroma and immune system can drive or prevent tumour progression. https://doi.org/https://doi.org/10.1088/2057-1739/aa7e86
Sen, S., Engler, A. J., & Discher, D. E. (2009). Matrix strains induced by cells: Computing how far cells can feel. *Cellular and Molecular Bioengineering*, *2*(1), 39–48. https://doi.org/10.1007/s12195-009-0052-z
Shafi, A., Nguyen, T., Peyvandipour, A., Draghici, S., & Kelso, J. (2020). GSMA: An approach to identify robust global and test Gene Signatures using Meta-Analysis. *Bioinformatics*, *36*(2), 487–495. https://doi.org/10.1093/bioinformatics/btz561

Shapiro, J. M., & Oyen, M. L. (2013). Hydrogel Composite Materials for Tissue Engineering Scaffolds. *JOM*, *65*(4), 505–516. https://doi.org/10.1007/s11837-013-0575-6

Shastri, M. D., Chong, W. C., Dua, K., Peterson, G. M., Patel, R. P., Mahmood, M. Q., … Hansbro, P. M. (2020). Emerging concepts and directed therapeutics for the management of asthma: regulating the regulators. *Inflammopharmacology*, (0123456789). https://doi.org/10.1007/s10787-020-00770-y

Shi-wen, X., Liu, S., Eastwood, M., Sonnylal, S., Denton, C. P., Abraham, D. J., & Leask, A. (2009). Rac Inhibition Reverses the Phenotype of Fibrotic Fibroblasts, *4*(10), 1–9. https://doi.org/10.1371/journal.pone.0007438

Shimizu, Y., Dobashi, K., Iizuka, K., Horie, T., Suzuki, K., Tukagoshi, H., … Mori, M. (2001). Contribution of small GTPase Rho and its target protein ROCK in a murine model of lung fibrosis. *American Journal of Respiratory and Critical Care Medicine*, *163*(1), 210–217. https://doi.org/10.1164/ajrccm.163.1.2001089

Shinsato, Y., Doyle, A. D., Li, W., & Yamada, K. M. (2020). Direct comparison of five different 3D extracellular matrix model systems for characterization of cancer cell migration. *Cancer Reports*, (May), 1–11. https://doi.org/10.1002/cnr2.1257

Shoulders, M. D., & Raines, R. T. (2009). Collagen Structure and Stability. *Annual Review of Biochemistry*, *78*(1), 929–958. https://doi.org/10.1146/annurev.biochem.77.032207.120833

Singer, A. J., & Clark, R. A. F. (1999). Cutaneous Wound Healing. *New England Journal of Medicine*, *341*(10), 738–746. https://doi.org/10.1056/NEJM199909023411006

Sit, R. V, Chang, S., Conley, S. D., Mori, Y., & Seita, J. (2019). A molecular cell atlas of the human lung from single cell RNA sequencing, *7191*.

Smithmyer, M. E., Sawicki, L. A., & Kloxin, A. M. (2014). Hydrogel scaffolds as *in vitro* models to study fibroblast activation in wound healing and disease. *Biomaterials Science*, *2*(5), 634–650. https://doi.org/10.1039/C3BM60319A

Stracuzzi, A., Wahlsten, A., Giampietro, C., Hopf, R., Restivo, G., Martyts, A., … Ehret, A. E. (n.d.). The key role of fibre-matrix coupling for connective tissue mechanobiology and chemomechanics at cell length scale.

Stuart, T., Butler, A., Hoffman, P., Hafemeister, C., Papalexi, E., Mauck, W. M., … Satija, R. (2019). Comprehensive Integration of Single-Cell Data. *Cell*, *177*(7), 1888-1902.e21. https://doi.org/10.1016/j.cell.2019.05.031

Sukmana, I., & Vermette, P. (2010). Polymer fibers as contact guidance to orient microvascularization in a 3D environment. *Journal of Biomedical Materials Research - Part A*, *92*(4), 1587–1597. https://doi.org/10.1002/jbm.a.32479

Sun, G., & Mao, J. J. (2012). Engineering dextran-based scaffolds for drug delivery and tissue repair. *Nanomedicine*, *7*(11), 1771–1784. https://doi.org/10.2217/nnm.12.149

Sundarakrishnan, A., Chen, Y., Black, L. D., Aldridge, B. B., & Kaplan, D. L. (2018). Engineered cell and tissue models of pulmonary fibrosis. *Advanced Drug Delivery Reviews*, *129*, 78–94. https://doi.org/10.1016/j.addr.2017.12.013

Sundarakrishnan, A., Zukas, H., Coburn, J., Bertini, B. T., Liu, Z., Georgakoudi, I., … Kaplan, D. L. (2019). Bioengineered *in vitro* Tissue Model of Fibroblast Activation for Modeling Pulmonary Fibrosis. *ACS Biomaterials Science & Engineering*, *5*, 2417–2429. research-article. https://doi.org/10.1021/acsbiomaterials.8b01262

Sundararaj, K. P., Samuvel, D. J., Li, Y., Sanders, J. J., Lopes-Virella, M. F., & Huang, Y. (2009). Interleukin-6 released from fibroblasts is essential for up-regulation of matrix metalloproteinase-1 expression by U937 macrophages in coculture: Cross-talking between

fibroblasts and U937 macrophages exposed to high glucose. *Journal of Biological Chemistry*, *284*(20), 13714–13724. https://doi.org/10.1074/jbc.M806573200
Szklarczyk, D., Gable, A. L., Lyon, D., Junge, A., Wyder, S., Huerta-Cepas, J., … Von Mering, C. (2019). STRING v11: Protein-protein association networks with increased coverage, supporting functional discovery in genome-wide experimental datasets. *Nucleic Acids Research*, *47*(D1), D607–D613. https://doi.org/10.1093/nar/gky1131
Tapon, N., & Hall, A. (1997). Rho, Rac and Cdc42 GTPases regulate the organization of the actin cytoskeleton. *Current Opinion in Cell Biology*, *9*(1), 86–92. https://doi.org/10.1016/S0955-0674(97)80156-1
Tibbitt, M. W., & Anseth, K. S. (2009). Hydrogels as extracellular matrix mimics for 3D cell culture. *Biotechnology and Bioengineering*, *103*(4), 655–663. https://doi.org/10.1002/bit.22361
Tomasek, J. J., Gabbiani, G., Hinz, B., Chaponnier, C., & Brown, R. A. (2002). Myofibroblasts and mechano: Regulation of connective tissue remodelling. *Nature Reviews Molecular Cell Biology*, *3*(5), 349–363. https://doi.org/10.1038/nrm809
Tschumperlin, D. J. (2013). Fibroblasts and the ground they walk on. *Physiology*, *28*(6), 380–390. https://doi.org/10.1152/physiol.00024.2013
Tschumperlin, D. J., & Lagares, D. (2020). Mechano-therapeutics: Targeting Mechanical Signaling in Fibrosis and Tumor Stroma. *Pharmacology and Therapeutics*, *212*, 107575. https://doi.org/10.1016/j.pharmthera.2020.107575
Tsukui, T., Sun, K.-H., Wetter, J. B., Wilson-Kanamori, J. R., Hazelwood, L. A., Henderson, N. C., … Sheppard, D. (2020). Collagen-producing lung cell atlas identifies multiple subsets with distinct localization and relevance to fibrosis. *Nature Communications*, *11*(1), 1920. https://doi.org/10.1038/s41467-020-15647-5
Ushiki, T. (n.d.). Collagen Fibers, Reticular Fibers and Elastic Fibers. A Comprehensive Understanding from a Morphological Viewpoint. https://doi.org/10.1679/aohc.65.109
van Dijk-Wotthuis, W. N. E., Franssen, O., Talsma, H., van Steenbergen, M. J., Kettenes-van den Bosch, J. J., & Hennink, W. E. (1995). Synthesis, Characterization, and Polymerization of Glycidyl Methacrylate Derivatized Dextran. *Macromolecules*, *28*(18), 6317–6322. https://doi.org/10.1021/ma00122a044
van Grunsven, L. A. (2017). 3D *in vitro* models of liver fibrosis. *Advanced Drug Delivery Reviews*, *121*, 133–146. https://doi.org/10.1016/j.addr.2017.07.004
van Helvert, S., Storm, C., & Friedl, P. (2018). Mechanoreciprocity in cell migration. *Nature Cell Biology*, *20*(1), 8–20. https://doi.org/10.1038/s41556-017-0012-0
Vogel, V. (2018). Unraveling the Mechanobiology of Extracellular Matrix.
Vyalov, S. L., Gabbiani, G., & Kapanci, Y. (1993). Rat alveolar myofibroblasts acquire ??-smooth muscle actin expression during bleomycin-induced pulmonary fibrosis. *American Journal of Pathology*, *143*(6), 1754–1765.
Walraven, M., & Hinz, B. (2018). Therapeutic approaches to control tissue repair and fibrosis: Extracellular matrix as a game changer. *Matrix Biology*, *71–72*, 205–224. https://doi.org/10.1016/j.matbio.2018.02.020
Wang, H., Abhilash, A. S., Chen, C. S., Wells, R. G., & Shenoy, V. B. (2015). Long-range force transmission in fibrous matrices enabled by tension-driven alignment of fibers. *Biophysical Journal*, *107*(11), 2592–2603. https://doi.org/10.1016/j.bpj.2014.09.044
Wang, W., Wyckoff, J. B., Frohlich, V. C., Wang, W., Wyckoff, J. B., Frohlich, V. C., … Condeelis, J. S. (2002). Single Cell Behavior in Metastatic Primary Mammary Tumors

Correlated with Gene Expression Patterns Revealed by Molecular Profiling Single Cell Behavior in Metastatic Primary Mammary Tumors Correlated with Gene Expression Patterns Revealed by Molecular Pro. *Cancer Research*, *62*(21), 6278–6288. Retrieved from http://eutils.ncbi.nlm.nih.gov/entrez/eutils/elink.fcgi?dbfrom=pubmed&id=12414658&retmode=ref&cmd=prlinks%5Cnpapers3://publication/uuid/C1163A1A-24F2-45E5-BD68-595D11577D97

Wang, W. Y., Pearson, A. T., Kutys, M. L., Choi, C. K., Wozniak, M. A., Baker, B. M., & Chen, C. S. (2018). Extracellular matrix alignment dictates the organization of focal adhesions and directs uniaxial cell migration. *APL Bioengineering*, *2*(4). https://doi.org/10.1063/1.5052239

Wang, X., Ding, B., & Li, B. (2013). Biomimetic electrospun nanofibrous structures for tissue engineering. *Materials Today*, *16*(6), 229–241. https://doi.org/10.1016/j.mattod.2013.06.005

Weigelin, B., Bakker, G.-J., & Friedl, P. (2012). Intravital third harmonic generation microscopy of collective melanoma cell invasion. *IntraVital*, *1*(1), 32–43. https://doi.org/10.4161/intv.21223

Wells, A. U., & Maher, T. M. (2017). Update in interstitial lung disease 2016. *American Journal of Respiratory and Critical Care Medicine*, *196*(2), 132–138. https://doi.org/10.1164/rccm.201702-0351UP

Wilbrey-clark, A., Roberts, K., & Teichmann, S. A. (2020). Cell Atlas technologies and insights into tissue architecture, *0*(April), 1427–1442.

Wirtz, D. (2004). Intracellular Mechanics of Migrating Fibroblasts. *Mol Biol Cell*, *15*(December), 5318–5328. https://doi.org/10.1091/mbc.E04

Wolf, K., Alexander, S., Schacht, V., Coussens, L. M., von Andrian, U. H., van Rheenen, J., … Friedl, P. (2009). Collagen-based cell migration models *in vitro* and *in vivo*. *Seminars in Cell and Developmental Biology*, *20*(8), 931–941. https://doi.org/10.1016/j.semcdb.2009.08.005

Wongkarnjana, A., Yanagihara, T., & Kolb, M. R. J. (2019). Treatment of idiopathic pulmonary fibrosis with Nintedanib: an update. *Expert Review of Respiratory Medicine*, *13*(12), 1139–1146. https://doi.org/10.1080/17476348.2019.1673733

Wozniak, M. A., & Chen, C. S. (2009). Mechanotransduction in development: A growing role for contractility. *Nature Reviews Molecular Cell Biology*, *10*(1), 34–43. https://doi.org/10.1038/nrm2592

Wu, S. Z., Roden, D. L., Wang, C., Holliday, H., Harvey, K., Cazet, A. S., … Swarbrick, A. (2020). Stromal cell diversity associated with immune evasion in human triple-negative breast cancer. *The EMBO Journal*, *39*(19), 1–20. https://doi.org/10.15252/embj.2019104063

Wynn, T. A. (2008). Cellular and molecular mechanisms of fibrosis. *The Journal of Pathology*, *214*(2), 199–210. https://doi.org/10.1002/path.2277

Xiang, M., Grosso, R. A., Takeda, A., Pan, J., Bekkhus, T., Brulois, K., … Butcher, E. C. (2020). A Single-Cell Transcriptional Roadmap of the Mouse and Human Lymph Node Lymphatic Vasculature. *Frontiers in Cardiovascular Medicine*, *7*(April). https://doi.org/10.3389/fcvm.2020.00052

Xu, Y., Mizuno, T., Sridharan, A., Du, Y., Guo, M., Tang, J., … Whitsett, J. A. (2016). Single-cell RNA sequencing identifies diverse roles of epithelial cells in idiopathic pulmonary fibrosis. *JCI Insight*, *1*(20). https://doi.org/10.1172/jci.insight.90558

Yamada, K. M., & Sixt, M. (2019). Mechanisms of 3D cell migration. *Nature Reviews*

Molecular Cell Biology, (Box 1). https://doi.org/10.1038/s41580-019-0172-9
Yasui, T., Tanaka, R., Hase, E., Fukushima, S., & Araki, T. (2014). *In vivo* time-lapse imaging of skin burn wound healing using second-harmonic generation microscopy . *Multiphoton Microscopy in the Biomedical Sciences XIV*, *8948*(February 2014), 89480B. https://doi.org/10.1117/12.2038022
Yee, H. F., Melton, A. C., & Tran, B. N. (2001). RhoA/Rho-associated kinase mediates fibroblast contractile force generation. *Biochemical and Biophysical Research Communications*, *280*(5), 1340–1345. https://doi.org/10.1006/bbrc.2001.4291
Yeung, T., Georges, P. C., Flanagan, L. A., Marg, B., Ortiz, M., Funaki, M., … Janmey, P. A. (2005). Effects of substrate stiffness on cell morphology, cytoskeletal structure, and adhesion. *Cell Motility and the Cytoskeleton*, *60*(1), 24–34. https://doi.org/10.1002/cm.20041
Yu, Y., & Chau, Y. (2012). One-Step "Click" Method for Generating Vinyl Sulfone Groups on Hydroxyl-Containing Water-Soluble Polymers. *Biomacromolecules*, *13*(3), 937–942. https://doi.org/10.1021/bm2014476
Yue, K., Trujillo-de Santiago, G., Alvarez, M. M., Tamayol, A., Annabi, N., & Khademhosseini, A. (2015). Synthesis, properties, and biomedical applications of gelatin methacryloyl (GelMA) hydrogels. *Biomaterials*, *73*, 254–271. https://doi.org/10.1016/j.biomaterials.2015.08.045
Zhang, Y., Lin, Z., Foolen, J., Schoen, I., Santoro, A., Zenobi-Wong, M., & Vogel, V. (2014). Disentangling the multifactorial contributions of fibronectin, collagen and cyclic strain on MMP expression and extracellular matrix remodeling by fibroblasts. *Matrix Biology*, *40*, 62–72. https://doi.org/10.1016/j.matbio.2014.09.001
Zigrino, P., Brinckmann, J., Niehoff, A., Lu, Y., Giebeler, N., Eckes, B., … Mauch, C. (2016). Fibroblast-Derived MMP-14 Regulates Collagen Homeostasis in Adult Skin. *Journal of Investigative Dermatology*, *136*(8), 1575–1583. https://doi.org/10.1016/j.jid.2016.03.036